

6-28-2010

Longwave and bi-color type-II InAs/(In)GaSb superlattice infrared detectors

Arezou Khoshakhlagh

Follow this and additional works at: https://digitalrepository.unm.edu/ose_etds

Recommended Citation

Khoshakhlagh, Arezou. "Longwave and bi-color type-II InAs/(In)GaSb superlattice infrared detectors." (2010).
https://digitalrepository.unm.edu/ose_etds/12

This Dissertation is brought to you for free and open access by the Engineering ETDs at UNM Digital Repository. It has been accepted for inclusion in Optical Science and Engineering ETDs by an authorized administrator of UNM Digital Repository. For more information, please contact disc@unm.edu.

Arezou KhoshaKhlagh

Candidate

Optical sciences and Engineering - Electrical Engineering

Department

This dissertation is approved, and it is acceptable in quality and form for publication:

Approved by the Dissertation Committee:

Prisha

, Chairperson

Juba F. Juba

L. Ralph Dawson

Abhyas Kalyan

Longwave and Bi-color Type-II InAs/(In)GaSb Superlattice Infrared Detectors

by

Arezou Khoshakhlagh

B.S., University of New Mexico, 2004
M.S., University of New Mexico, 2008

DISSERTATION

Submitted in Partial Fulfillment of the
Requirements for the Degree of

**Doctor of Philosophy
Optical Sciences and Engineering**

The University of New Mexico
Albuquerque, New Mexico

May, 2010

©2010, Arezou Khoshakhlagh

Dedication

*To my Parents,
Shahnaz and Rahman*

Acknowledgments

First and foremost I offer my sincerest gratitude to my advisor, Dr. Sanjay Krishna, who has supported me throughout my thesis with his patience and knowledge whilst allowing me the room to work in my own way. I attribute this thesis to his encouragement and effort and without his support this thesis, too, would not have been completed or written. One simply could not wish for a better or friendlier advisor. I greatly acknowledge the assistance provided to me by the members of my dissertation committee, Dr. Ralph Dawson, Dr. Luke Lester and Dr. Abhaya Datye. I sincerely appreciate the crystal growth knowledge bestowed upon me by Dr. Ralph Dawson. I would also like to acknowledge the group members for their support and great teamwork: Dr. J.B. Rodriguez, Dr. Elena Plis, Hasul Kim, Stephen Myers, Nutan Gautam, and Brianna Klein.

I would like to thank my family and friends for their support. My special thanks goes to my parents, Rahman and Shahnaz and my husband, Mahmood. Without their love, support and understanding I would not have been able to finish this thesis.

**Longwave and Bi-color Type-II
InAs/(In)GaSb Supperlattice Infrared
Detectors**

BY

Arezou Khoshakhlagh

ABSTRACT OF DISSERTATION

Submitted in Partial Fulfillment of the
Requirements for the Degree of

**Doctor of Philosophy
Optical Sciences and Engineering**

The University of New Mexico
Albuquerque, New Mexico

May, 2010

Longwave and Bi-color Type-II InAs/(In)GaSb Superlattice Infrared Detectors

by

Arezou Khoshakhlagh

B.S., University of New Mexico, 2004

M.S., University of New Mexico, 2008

Ph.D., Optical Sciences and Engineering, University of New Mexico,
2010

Abstract

Infrared (IR) photodetectors are useful for a variety of military and civil applications such as target acquisition, medical diagnostics, pollution monitoring, to name just a few. Presently photonic IR detectors are based on interband transitions in low bandgap semiconductors such as mercury cadmium telluride (MCT) or InSb or in intersubband transitions in hetero-engineered structures such as quantum well or quantum dot infrared photodetectors (QWIPs or QDIPs). These detectors operate at low temperatures (77 K - 200 K) in order to obtain high signal to noise ratio. The cooling requirement limits the lifetime, increases the weight and the total cost, as well as the power budget, of the whole infrared system. There is a concerted effort to develop photonic detectors operating at higher temperatures. In the past few years, interband transitions in type II InAs/GaSb strain layer superlattices (SL)

have emerged as a competing technology among other IR systems. Although MCT and QWIP technologies are relatively more mature than the SL technology, the SL technology has potential to enhance performance in several key areas. One of the main advantages of this system lies in the fact that the effective band gap of the SL can be tailored over a wide range ($3 \mu\text{m} < \lambda_c < 30 \mu\text{m}$) by varying the thickness of two “mid bandgap” constituent materials, namely GaSb and InAs. Tunneling currents in SL are reduced due to a larger electron effective mass. Large splitting between heavy-hole and light-hole valence subbands due to strain in the SLs contributes to the suppression of Auger recombination. Moreover, the band structure of the SL can be engineered to enhance carrier lifetimes and reduce noise at higher temperatures. SL based IR detectors have demonstrated high quantum efficiency, high temperature operation, and are suitable for incorporation in focal plane arrays (FPA) by tapping into the mature III-V based growth and fabrication processes.

The recently proposed nBn heterostructure design has demonstrated a 100 *K* increase in background-limited infrared photodetection (BLIP) for InAs-based device, by decreasing Shockley-Read-Hall generation currents and by suppressing surface currents using specific processing.

Third generation IR detectors have three main emphasis, High operating temperature (HOT), multicolor capability, and large format arrays. This work concentrates on multicolor and HOT IR detectors based on nBn design. Contributions of this thesis include

1. **Development of design and growth procedure for the long-wave (LW) SL detectors leading to an improved detector performance**

13 MLs of InAs and 7 MLs of GaSb with InSb strain compensating layer were designed and optimized for LW SL detectors. LWIR pin and nBn detectors were introduced and their optical and electrical properties were compared. LW

nBn detectors show higher device performance in terms of lower dark current density and higher responsivity as compared to the LW pin detectors. The reduction in dark current in LW nBn detector is due to reduction of SRH centers as well as surface leakage currents. The increase in responsivity for LW nBn detectors is due to reduction non-radiative SRH recombination.

2. Design, growth and characterization of bi-color nBn detectors

Present day two color SL detectors require two contacts per pixel leading to a complicated processing scheme and expensive read out integrated circuits (ROICs). The nBn architecture was modified to realize a dual-band response by changing the polarity of applied bias using single contact processing. The spectral response shows a significant change in the LWIR to MWIR ratio within a very small bias range (~ 100 mV) making it compatible with commercially available ROICs.

3. Investigation of background carrier concentration in SLs

The electrical transport in SLs was investigated in order to improve the collection efficiency and understand SL devices performance operating at ambient temperature. For this purpose background carrier concentration of type-II InAs/GaSb SLs on GaAs substrates are studied. The hall measurements on mid-wave SLs revealed that the conduction in the MWIR SLs is dominated by holes at low temperatures (< 200 K) and by electrons at high temperatures (> 200 K) and is dominated by electrons at all temperatures for LWIR SLs possibly due to the thicker InAs (residually n-type) and thinner GaSb (residually p-type) layers. By studying the in-plane transport characteristics of LW SLs grown at different temperatures, it was shown that interface roughness scattering is the dominant scattering mechanism at higher temperatures (200 K- 300 K).

Contents

List of Figures	xv
List of Tables	xxii
1 Introduction	1
1.1 Basics of infrared detection	1
1.1.1 Thermal Radiation Laws	3
1.2 Infrared detectors	5
1.2.1 Thermal Detectors	5
1.2.2 Photon detectors	6
1.3 Figures of merit for infrared detectors	8
1.3.1 Responsivity	9
1.3.2 Noise Equivalent Power	10
1.3.3 Detectivity	10
1.4 Focal Plane Arrays (FPAs)	11

Contents

1.4.1	Thermal detector FPAs	11
1.4.2	Photon detector FPAs	12
1.5	Conclusion	18
2	Materials and Methods	21
2.1	Introduction	21
2.2	Design tools	22
2.3	Molecular Beam Expitaxy (MBE)	24
2.3.1	Growth of InAs/GaSb superlattice	25
2.4	X-ray diffraction	26
2.5	Atomic Force Microscopy (AFM)	30
2.6	Absorption measurements	30
2.7	Processing	32
2.8	Characterization	34
2.9	Conclusion	38
3	Mid-wave and Long-wave pin and nBn SL detectors	39
3.1	Introduction	39
3.2	Midwave superlattices (MW SLs)	40
3.2.1	Design and growth of MW SLs	40
3.2.2	Calibration of the group III elements for SL growth	40

Contents

3.2.3	MW SL growth optimization	42
3.3	Midwave pin InAs/GaSb SL detector	42
3.3.1	Growth	42
3.3.2	Processing	43
3.3.3	Characterization	44
3.4	Longwave SLs	45
3.4.1	Design of the LW SLs	45
3.4.2	Growth optimization of InAs/GaSb SLs for LWIR region	49
3.5	Longwave pin detectors	57
3.5.1	LWIR InAs/GaSb pin diodes growth and processing	58
3.5.2	Characterization of LWIR InAs/GaSb pin diodes	59
3.6	Longwave nBn detectors	64
3.6.1	nBn detectors	64
3.6.2	Growth and processing of LWIR SL detector based on nBn design	66
3.6.3	Characterization of the LWIR SL detector based on nBn design	69
3.7	Comparison of the LWIR pin and nBn detectors	70
3.8	Conclusion	76
4	Dual Band nBn InAs/Ga(In)Sb SL detectors	78
4.1	Introduction	78

Contents

4.2	Background and applications of Bi-color infrared detectors	79
4.3	Present bicolor detectors	81
4.4	Epitaxial growth and fabrication of dual-color nBn SL detectors	83
4.5	Device characterization: results and discussions	86
4.6	Conclusion	93
5	Transport properties of type-II InAs/GaSb SLs	95
5.1	Introduction	95
5.2	Background and motivation	96
5.3	Interfacial misfit dislocation arrays (IMF)	97
5.3.1	Growth of the GaSb/GaAs using IMF method	97
5.4	Background carrier concentration of mid-wave and long-wave superlattices grown on GaAs	98
5.5	Transport properties of longwave SLs on GaSb substrate	105
5.5.1	Growth, processing, characterization of the long-wave superlattices on GaSb substrate	105
5.6	Conclusion	110
6	Conclusions and Future Work	114
6.1	Conclusion	114
6.2	Future work	119
6.2.1	SL transport studies	119

Contents

6.2.2 Minority carrier lifetime 121

6.2.3 Device performance optimization for pin and nBn detectors . . 121

6.2.4 Alternative designs 121

6.2.5 Design of very longwave infrared (VLWIR) detector and theoretical modeling 122

References **125**

List of Figures

1.1	The Electromagnetic Spectrum	2
1.2	Transmission of IR in atmosphere	2
1.3	Planck's laws: spectral radiant emittance of a black body vs wavelength at various temperatures . The dashed line is the Wien's law.	4
1.4	Ideal quantum efficiency vs. wavelength.	6
1.5	Schematic of a photoconductor detector and its band diagram.	7
1.6	Schematic of a pin detector and its corresponding band diagram.	8
1.7	Schematic diagram of GaAs/AlGaAs QWIP	14
1.8	Heterojunction formed by InAs and GaSb	16
1.9	Band edge diagram illustrating the confined electron and hole minibands which form the energy band gap.	17
2.1	(a) wavefunctions (b) dispersion diagram at 0 K for 2.4nm GaSb/ 2.4nm InAs.	23
2.2	(a) doping profile (b) band alignment of a pin MWIR SL detector	24
2.3	Schematic of a Molecular Beam Epitaxy growth chamber	26

List of Figures

2.4	Schematic diffraction of X-rays in the crystal	27
2.5	Typical XRD spectrum from InAs/GaSb SL	28
2.6	Essential components of atomic force microscopy (AFM)	31
2.7	(a) Optical absorption measurement set-up, sample holder is loaded in the main compartment of the FTIR (b) Brewster angle sample holder (c) Normal incidence sample holder	32
2.8	Schematics of the masks used in fabrication process of the superlat- tice detectors	34
2.9	Conventionally processed pin diode	34
2.10	Spectral response measurement setup	36
2.11	Responsivity measurement setup	37
3.1	(a) electron and hole wavefunctions (b) dispersion diagram at 0 K for 2.4 nm GaSb/2.4 nm InAs.	41
3.2	Estimation of the growth rates by X-ray scan of SLs width different period	42
3.3	shutter sequence for the growth of MW SLs	43
3.4	A schematic of pin InAs/GaSb SL MWIR detector	44
3.5	A schematic of processed MW SL pin detector	45
3.6	(a) Dark current density, and (b) spectral response of MWIR pin SL detector	46
3.7	(a) band alignment, and electron/hole wavefunctions (b) dispersion diagram of 13 MLs of InAs and 7 MLs of GaSb	47

List of Figures

3.8	(a) band alignment, and electron/hole wavefunctions (b) dispersion diagram of 13 MLs of InAs, 0.45 ML of strain compensating layer of InSb and 7 MLs of GaSb	48
3.9	Electron and hole wavefunction overlap and cutoff wavelength for 8 MLs GaSb/ X MLs InAs (X= 8, 10, 12, 14).	49
3.10	The temperature of (1×3) to (2×5) reconstruction transition was taken as a reference for the growth temperatures.	51
3.11	Growth optimization for LWIR structure using (a) InSb layer (b) group V soak time.	53
3.12	Growth temperature optimization for LWIR structure	55
3.13	LWIR nBn structure (b) XRD of LWIR nBn structure, almost zero % lattice mismatch between SL and GaSb substrate and 19 arcsec FWHM for the first satellite peak.	56
3.14	Cross-sectional STEM images of an nBn detector	57
3.15	(a) Schematic of LWIR SL pin detectors; represents three samples with different absorber region doping levels (b) HRXRD of the non-intentionally doped LWIR SL pin detector.	60
3.16	Dark current density at 77 K for the three pin structures.	61
3.17	(a) Responsivity and (b) detectivity measurements of the pin devices at 77 K	64
3.18	Schematic of nBn design. Majority carriers (electrons) are blocked by the barrier and minority carriers (holes) are the source of current.	65
3.19	(a) Structure schematic (b) HRXRD of the LWIR nBn detector.	68

List of Figures

3.20	Main processing steps for LWIR nBn detectors	69
3.21	(a) Shallow etch processing (b) deep etch processing (c) shallow etch processing with indication of diffusion lengths.	70
3.22	Dark current density of shallow, and deep etched nBn devices vs temperature. This comparison shows the effect of dark current density reduction due to reduction of surface leakage currents.	71
3.23	(a) Responsivity and (b) detectivity measurements of the nBn device at 77 K	72
3.24	Spectral response of (a) pin (b) nBn structure, 8 μm cutoff wavelength is shown in the two diagrams.	73
3.25	Dark current density at 77 K for nBn and pin structures	74
3.26	(a) Responsivity and (b) detectivity measurements of the pin and nBn devices at 77 K; nBn structure has the highest responsivity and detectivity values as compared to the pin structure.	75
4.1	(a) mid-wave infrared image (b) long-wave infrared image (c) long-wave subtracted from midwave images taken to locate fire spots from South America lands.	80
4.2	(a) cross-section schematic, and (c) typical I-V characteristic for a single-mesa, single-indium bump, dual-color detector design. With the appropriate polarity and voltage bias at the pixel contact, the Band 1 and Band 2 p-n junctions respond to shorter and longer wavelength infrared radiation, respectively.	82
4.3	(a) Schematic (b) SEM picture of two-color InAs/GaSb superlattice detector	83

List of Figures

4.4	(a) structure A: two color MWIR detector ($\lambda_{c1} \sim 3.5 \mu\text{m}$ and $\lambda_{c2} \sim 4.5 \mu\text{m}$) and b) structure B: dual band MW-LWIR ($\lambda_{c1} \sim 3.5 \mu\text{m}$ and $\lambda_{c2} \sim 8.0 \mu\text{m}$).	84
4.5	Current density at different temperatures for both shallow and deep etched devices.	85
4.6	Current density at different temperatures for (a) structure A and (b) structure B.	87
4.7	Spectral response of structure (a) A and (b) B at different temperatures under forward bias and reverse ; V_{bis} the applied voltage to the device.	88
4.8	Two color nBn detector under (a) forward bias and (B) reverse bias	89
4.9	The responsivity (solid black line, left axis) and quantum efficiency (dotted red line, right axis) for (a) structure A, and (b) structure B.	90
4.10	Structure C: Dual band MWIR/LWIR detector	91
4.11	Dark current density of two-color SL detector (structure C)	92
4.12	Spectral response of the bi-color structure at different temperatures under forward and reverse bias ; V_b is the applied voltage.	92
4.13	(a)The spectral response of structure C between 0 and +0.1V bias voltage, that is compatible with the bias range of present day ROICs. (b) the intensity study of MWIR, LWIR, and MWIR to LWIR ratio vs applied bias voltage at 77 K.	94

List of Figures

5.1	Cross-sectional TEM image of 120 nm of GaSb on GaAs showing a highly periodic array of misfit dislocations at the GaSb layer and the GaAs substrate [1].	98
5.2	a) Hall resistivity, b) Hall carrier concentration, and c) Hall mobility of non-intentionally doped mid-wave SL versus measurement temperature; SL is residually p-type at temperatures below 200 K and n-type at temperatures above 200 K. From Hall resistivity two activation energies of 193 meV and 23.86 meV were extracted which indicates existence of shallow and deep impurity levels in the SL. . .	101
5.3	a) Hall resistivity of non-intentionally doped long-wave SL versus measurement temperature, b) Hall carrier concentration versus measurement temperature, and c) Hall carrier concentration dependence on growth temperature; SL is residually n-type at all of the measurement temperatures. At low measurement temperatures extrinsic carriers and at high measurement temperatures intrinsic carriers are the dominant source of carriers in the LW SL.	103
5.4	a) Hall mobility versus measurement temperature, and b) Hall peak mobility of non-intentionally doped long-wave SL versus growth temperature; As the growth temperature increases, interface scattering becomes the dominant source of scattering in the SL which decreased the mobility and causes temperature independent behavior of the mobility. Also due to interface roughness scattering peak mobility decreases.	104
5.5	(a) Long-wave SL structure schematic (b) HRXRD of the sample grown at $T_t=45^\circ C$ used for transport studies.	106
5.6	Main steps of processing for substrate removal (flip-chip method) . .	107

List of Figures

5.7	Classical form of the sample for van der Pauw method measurements.	108
5.8	The van der Pauw configuration for lateral LW SL transport studies	108
5.9	(a) Hall experimental data for magnetic field rang of 0-12 T (b) Mobility spectra obtained from QMSA algorithm at 77 K (c) Mobility spectra obtained from QMSA algorithm at temperature range of 32-290 K .	112
5.10	(a) Carrier concentration versus $1/T$ for LWIR SLs on GaSb substrate; Two activation energies are extracted, indicating (b) shallow impurity donor levels close to the SL conduction band	113
6.1	Mechanical and chemical processing steps for GaSb substrate removal	120
6.2	SL sample geometry for vertical transport study	120
6.3	(a) next-nano band alignment simulation of 16 MLs InAs/0.86 MLs InSb/7 MLs GaSb (b) next-nano dispersion diagram which indicates a cut-off wavelength of 12 μm at 0 K (c) Growth optimization for VLWIR SL structure using InSb strain compensating layer	124

List of Tables

1.1	Subdivisions of the infrared spectrum	3
1.2	Some important parameters for InAs and GaSb at 300 <i>K</i>	17
1.3	A summary of reported MW/LW/VLW IR	19
3.1	Summary of dark current density, responsivity and detectivity of pin and nBn devices measured at 77 K, 7 μm	76

Chapter 1

Introduction

In this chapter general concept of infrared detection, infrared detectors and their figures of merit are introduced. Different types of infrared detectors and competing technologies and their advantages/disadvantages are covered. Finally, an alternative detector technology, type II InAs/(In)GaSb superlattice based detectors, for Mid-wave and Long-wave infrared detection is introduced.

1.1 Basics of infrared detection

An electromagnetic spectrum is the distribution of all electromagnetic waves arranged according to their wavelength or corresponding energy (see figure 1.1).

The infrared region of the electromagnetic spectrum corresponds to the region that is bounded on the short-wavelength side by visible light and on the long-wavelength side by microwaves. Since heated objects radiate energy in infrared, this region of the electromagnetic spectrum is referred to as the heat region as well. The infrared region of the electromagnetic spectrum is divided into subdivisions based on the atmospheric absorption. IR spectral region are affected by strong absorptions

Chapter 1. Introduction

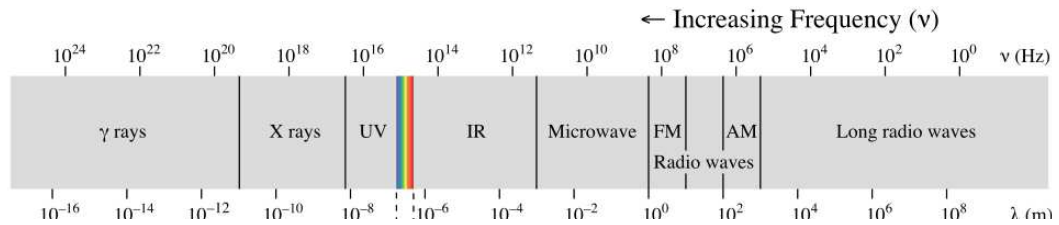


Figure 1.1: The Electromagnetic Spectrum

due to molecules in the earth's atmosphere, particularly CO_2 and H_2O and Ozon. Some minor constituents, including carbon monoxide, nitrous oxide, methane, and nitric oxide, are less significant absorbers. The transmission of IR in atmosphere is shown in figure 1.2.

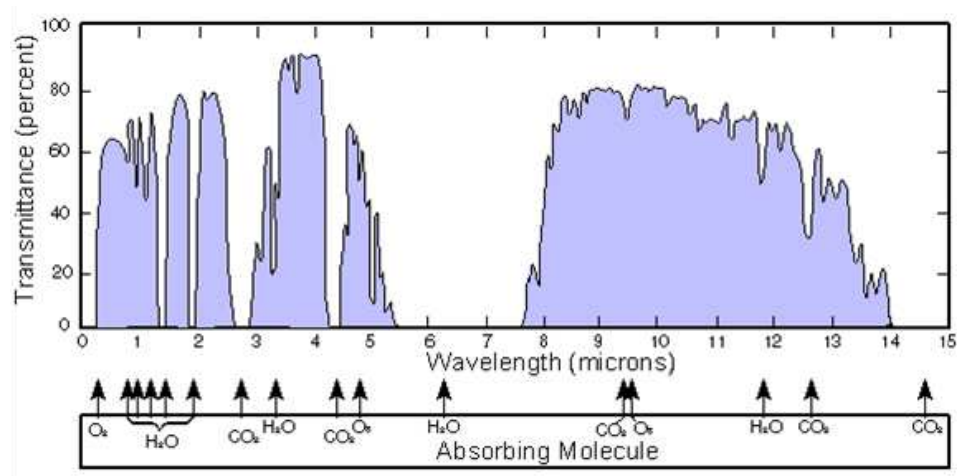


Figure 1.2: Transmission of IR in atmosphere

The atmosphere is relatively transparent from about 3 to 5 μm and 8 to 13 μm . These regions are referred to as atmospheric windows and are commonly used

Chapter 1. Introduction

by IR detectors. The infrared spectrum considering the atmospheric absorption is subdivided in to five regions which are summarized in the table below:

Table 1.1: Subdivisions of the infrared spectrum

Designation	Abbreviation	Limits(μm)
Near Infrared Radiation	NIR	0.7-1.5
Short Wavelength Infrared Radiation	SWIR	1.5-2.5
Medium Wavelength Infrared Radiation	MWIR	3-5
Long Wavelength Infrared Radiation	LWIR	8-12
Very Long Wavelength Infrared Radiation	VLWIR	12-32

1.1.1 Thermal Radiation Laws

- *Planck's law* describes the spectral distribution of the radiation from a black-body as (see figure 1.3)

$$W_\lambda = \frac{2\pi hc^2}{\lambda^5} \frac{1}{\frac{hc}{e\lambda kT} - 1} \quad (1.1)$$

Where W_λ is spectral radiant emittance ($Wcm^{-2}\mu^{-1}$), k is the Boltzmann's constant, h is the plank's constant and c is the speed of th light. This law describes the probability distribution of emitted wavelengths at a given temperature.

- *Wien's displacement law* describes the wavelength at which the maximum spectral radiant emittance occurs,

$$\lambda_m(\mu\text{m}) = \frac{2898}{T(K)}. \quad (1.2)$$

It is derived differentiating Plank's law and then solving for the maximum spectral radiant emittance. The wavelength varies inversely with the absolute temperature as expressed by equation 1.2.

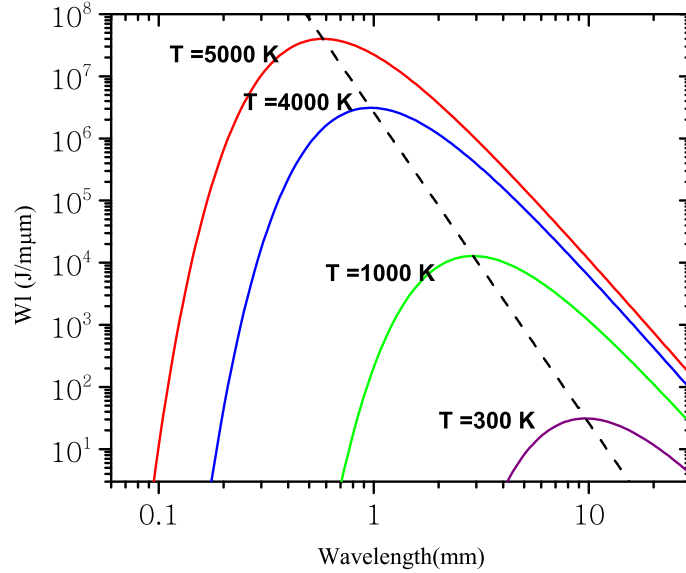


Figure 1.3: Planck's laws: spectral radiant emittance of a black body vs wavelength at various temperatures . The dashed line is the Wien's law.

- *Stefan-Boltzmann law* is achieved by integrating the Planck's law over wavelength limits extending from zero to infinity which gives an expression for the radiant emittance :

$$W = \sigma T^4 \tag{1.3}$$

Where W is the radiant emittance (Wcm^{-2}), and σ is Stefan-Boltzmann constant ($5.6697 \times 10^{-12}Wcm^{-2}K^{-4}$). In figure 1.3 the rapid increase in radiant emittance with increasing temperature is evident.

All of the above formulae describe the radiation from a blackbody. For sources that are not blackbodies a factor (emissivity (ϵ)) can be added. Emissivity is given by the ratio of the radiant emittance of the source to the radiant emittance of a black body at the same temperature. Its value can lie between zero for a nonradiating source to unity for blackbody.

1.2 Infrared detectors

The central element of any IR detection system is the detector. The detector is the device which converts an optical signal into some other form, in most cases, electrical. By the method of transduction, detectors may be divided in two classes: thermal detectors and photon detectors.

1.2.1 Thermal Detectors

When thermal detectors are heated by incoming IR radiation their temperature increases and the temperature changes are measured by any temperature-dependent mechanism, such as voltage, or resistance. The main advantage of the thermal detectors is their room temperature operation without any requirement for cooling which has made them a good candidate in spaceborne applications. The main disadvantage of thermal detectors is their long time constant which is usually a few milliseconds or longer and therefore, they are rarely used in applications that high data rates are required. The most common thermal detectors providing an electrical output are:

- Bolometers are the thermal detectors which their electrical resistance changes when heated by the incident radiation.
- Thermocouples consist of two dissimilar metals, joined together at one end. When infrared radiation is absorbed by the junction of the two metals, a voltage is produced that can be correlated back to the temperature. Several thermocouples connected in series form a thermopile.
- Pyroelectric detectors operate when a change occurs in the temperature due to a change in incident radiation which causes an electrical polarization of the material. This polarization change occurs on the surface of the element creating a current that can be measured.

1.2.2 Photon detectors

Photon detectors operate by the direct interaction of radiation with the atomic lattice of the material. This interaction of light and matter produces electrical parameter changes that are detected by associated circuitry. Electrical parameters that can change in a photon detector are resistance, inductance, voltage and current. Understanding the concept of quantum efficiency is the key element to understand the photon-detection process. The quantum efficiency is the number of independent electrons produced per photon. Quantum efficiency takes into account reflectance, absorptance, scattering, and electron recombination. The ideal quantum efficiency is a binary function of wavelength which either photon has sufficient energy to produce a photogenerated electron or it does not. As the monochromatic optical radiation moves further into the infrared, the photon energy decreases and does not have sufficient energy to create a free electron. This limit defines the upper cutoff wavelength (λ_c) of response. Figure 1.4 illustrates a plot of quantum efficiency versus wavelength for both ideal detectors and real detectors.

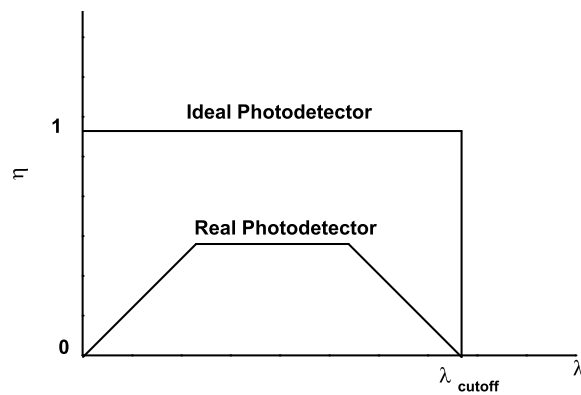


Figure 1.4: Ideal quantum efficiency vs. wavelength.

There are two distinct types of photon detectors: photoconductive (PC) and photovoltaic (PV).

Chapter 1. Introduction

- PC detectors are poor conductors whose conductivity is made larger by the presence of the photon-generated carriers. If light of high enough energy enters the device, photons excite bound electrons with sufficient energy to jump to the conduction band. The photo-generated carriers are collected by the opposite contacts resulting in free carriers that conduct electricity, thereby lowering the device resistance (see figure 1.5)

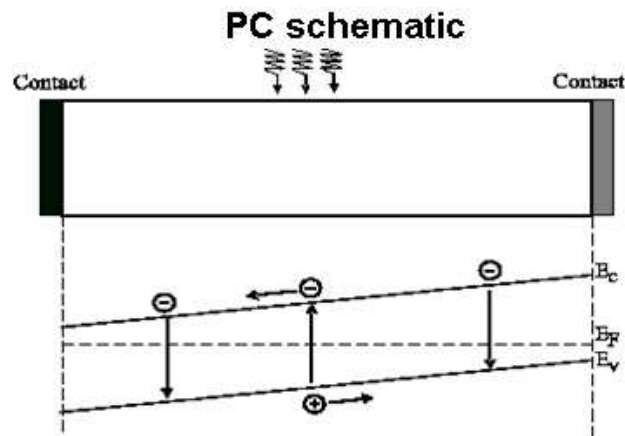


Figure 1.5: Schematic of a photoconductor detector and its band diagram.

- The photovoltaic detector produces a voltage or current from incident optical radiation. It is often called a photodiode because it is a semiconductor diode (p-n junction), which is light sensitive. In a photodiode, the optical radiation is absorbed at the junction of the two materials. The absorbed photons thus produce an electron-hole pair. These electron-hole pairs experience an internal electric field generating an external current or voltage, which can be measured. Figure 1.6 shows when a photovoltaic detector is under applied bias.

Because of the existence of an internal electric field in the depletion region of the PV detectors, thermally generated carriers are extracted from the depletion

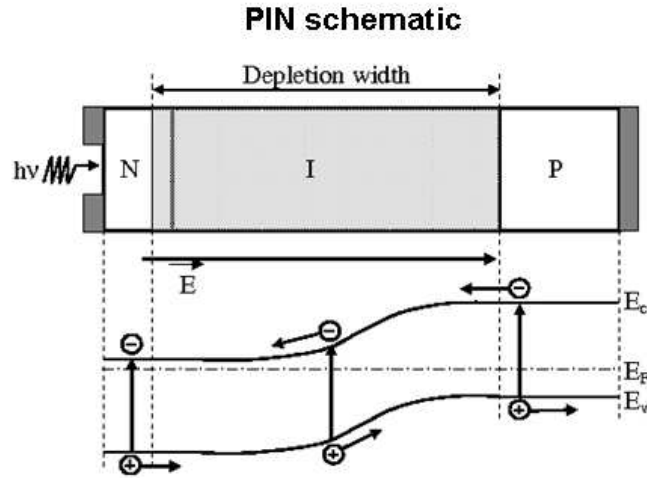


Figure 1.6: Schematic of a pin detector and its corresponding band diagram.

region which would not have the chance of recombination in the depletion region. However, since the internal electric field does not exist in the PC detectors, recombination is an added factor to the dark current. Thus dark current in PV is smaller as compared to PC detectors.

1.3 Figures of merit for infrared detectors

Figures of merit enable user to compare relative performance among different detectors. These figures of merit are applicable to any type of detector, and are independent of the generic optical-detector process. Most of the figures of merit are expressed in energy based units due to historical reasons. The general figures of merit are: responsivity, noise equivalent power, and detectivity.

1.3.1 Responsivity

The spectral responsivity is defined as the output per watt of monochromatic radiation. The output can be either current or voltage, per watt of monochromatic radiation. Photogenerated carriers are expressed as:

$$i_g = \eta \Phi_q q \quad (1.4)$$

Where i_g is the photogenerated carriers, η is the quantum efficiency, and Φ_q is the photon flux measured in photons/sec.

Using the above definition for the photogenerated carriers, responsivity is defined as following:

$$R_i = \frac{i_g}{\Phi_e} = \frac{\eta \Phi_q q}{\Phi_e} \quad (1.5)$$

Where Φ_e is the radiant power (flux) input given in watts.

The radiant power is related to the photon flux by:

$$\Phi_e = \frac{hc}{\lambda} \Phi_q \quad (1.6)$$

Therefore, responsivity is:

$$R(\lambda) = \frac{\eta \Phi_q q \lambda}{\Phi_q hc} = \frac{\lambda}{hc} q \eta \quad (1.7)$$

Equation 1.7 gives the relation between quantum efficiency and current responsivity as a function of wavelength for photon detectors.

Although responsivity of a detector is useful to predict an expected signal level for a given radiant power on the detector, the responsivity is of limited usefulness from a sensitivity point of view. In addition to the signal level, the noise level must also be considered to quantify the signal-to-noise ratio (SNR).

1.3.2 Noise Equivalent Power

The minimum radiant-flux level a detector can discern depends on the detector noise level. The signal current produced by the input power must be above the noise current to be easily detected. The SNR can be expressed as responsivity:

$$\frac{S}{N} = \frac{R\Phi_e}{i_n} \quad (1.8)$$

Where R is the responsivity, Φ_e is the radiant power (flux) in watts, and i_n is the noise current.

The radiant power, Φ_e incident on a detector that yields $SNR=1$ is called the noise-equivalent-power. Setting equation 1.8 equal to 1 and solving for the required power,

$$\Phi_e = \frac{i_n}{R} = \frac{\Phi_e}{i_{sig}/i_n} \quad (1.9)$$

Where i_{sig}/i_n is the current SNR. As the responsivity is a function of wavelength and frequency, so is NEP. The units of which are watts. The NEP can also be found using the voltage noise and the voltage responsivity. A more sensitive detector will have a lower NEP. To compare NEP of different detectors, parameters like optically active detector area, noise-equivalent electrical bandwidth, and other measurement parameters needs to be taken into account. An important parameter that facilitates comparison among different detectors with different geometries is the specific detectivity (D^*).

1.3.3 Detectivity

The figure of merit D^* called normalized detectivity is:

$$D^* = \frac{\sqrt{A_d \Delta f}}{NEP} \quad (1.10)$$

Chapter 1. Introduction

where A_d is the area of the detector and Δf is the bandwidth of the measurement. This figure of merit is sensitivity normalized to a 1-cm^2 area and 1-Hz noise-equivalent bandwidth. It can be interpreted as an SNR out of a detector when 1 W of radiant power is incident on the detector, given an area equal to 1 cm^2 and noise-equivalent bandwidth of 1 Hz . The units of D^* are Jones defined as $[cm\sqrt{Hz}/watt]=[Jones]$. D^* can be related to the responsivity by:

$$D^* = \frac{R\sqrt{A_d}}{i_n/\sqrt{\Delta f}} \quad (1.11)$$

D^* allows for comparison between detectors regardless of size or measurement parameters.

1.4 Focal Plane Arrays (FPAs)

A Focal Plane Array (FPA) is the main component used in advanced infrared imaging systems. An IR FPA is an array of single pixel devices used to capture an infrared signal. FPAs increase the efficiency of collection compared to a single pixel by decreasing acquisition time. Both thermal and photon detectors can be made into FPAs.

1.4.1 Thermal detector FPAs

Thermal focal plane arrays are typically operated at ambient temperature. Because thermal detection involves heating phenomena, and the temperature change process is slow, thermal FPAs have slow response. They also have low sensitivity. The fundamental limit to the sensitivity of any thermal detector is set by temperature fluctuation noise, i.e., random fluctuations in the temperature of the detector element due to fluctuations in the radiant power exchange between the detector and its

surroundings. On the other hand, in thermal FPAs the response is independent of wavelength, which is important for LWIR applications. They are also cheap and convenient to use. They have found widespread use in low cost applications, which do not require high performance and speed. They are frequently used in infrared spectrometers.

1.4.2 Photon detector FPAs

The first two generations of IR detectors were used in scanning and staring systems for military and civilian applications. The simplest scanning system consists of a row of detectors; The two-dimensional (2-D) image is generated by scanning the scene across the strip using a mechanical scanner. First generation scanning systems used linear arrays of intrinsic HgCdTe sensors. The invention of charge coupled devices (CCD) coupled with advances in silicon chip technology helped development of second generation detector arrays containing larger number of detector elements (staring systems). A staring system is a two-dimensional (2-D) array of detector pixels which are scanned electronically by circuits integrated with the arrays [2]. 2-D arrays used in staring systems have higher sensitivity as compared to the scanning systems due to their larger number of pixels. Higher frame rates are also achievable by electronic scanners in staring systems as compared to the mechanical scanners in scanning systems. Medium format 320×240 2D arrays operating in MWIR range were made with HgCdTe or indium antimonide detectors. Although the first and second generation IR detectors provided promising results in the MWIR and LWIR range, the need for larger number of pixels ($2K \times 2K$ pixels), higher frame rates, better thermal resolution and multi-color functionally led to third generation IR detectors [2].

Mercury Cadmium Telluride (HgCdTe) detectors

$\text{Hg}_{1-x}\text{Cd}_x\text{Te}$ is a II-VI material system. HgCdTe detectors can be made to operate in different spectral regions by controlling the Cd/Hg ratio of the material. CdTe and $\text{Hg}_{0.9}\text{Cd}_{0.1}\text{Te}$ are almost lattice matched (0.27%) which leads to the ability to grow high quality heterostructures. Also HgCdTe detectors have large optical coefficients leading to high quantum efficiencies (>80%). Another advantage of this type of detectors is that they have favorable inherent recombination mechanisms that lead to high operating temperatures. The mentioned features are the consequences of energy band structure of zinc-blend structure of HgCdTe.

One of the advantages of HgCdTe detectors is that it is possible to fabricate two color detectors. The read out integrated circuits (ROIC) of these two color HgCdTe detectors use two back-to-back photodiodes to individually bias the different layers. The two colors are achieved by changing the polarity of applied bias on the back-to-back photodiodes.

One of the main disadvantages of HgCdTe detectors is high nonuniformity in the growth process, and high pixel outage rates. This is especially true for LWIR/VLWIR material. The variation of x across the $\text{Hg}_{1-x}\text{Cd}_x\text{Te}$ wafer causes much larger spectral nonuniformity in the LWIR range. Therefore, for applications that require LWIR or two color LWIR/VLWIR bands, HgCdTe detectors are not the optimal solution. Thus, infrared detectors based on HgCdTe are very sensitive to the alloy composition ratio; this dependence requires a precise control over the temperature ($\Delta T=1-5^\circ\text{C}$) during the growth process. Nonuniformity increases the calibration requirements for HgCdTe detectors because this variation must be compensated for in software.

Quantum well infrared photodetectors (QWIPs)

Another alternative infrared technology for MWIR and LWIR bands is the quantum well infrared photodetectors (QWIPs). QWIPs are commercially fabricated using the GaAs/AlGaAs quantum well material system. In QWIP detectors, the low bandgap material acts as a trap for the electron. The electrons stay in the well until excited by incoming photons, until they gain enough energy to escape the well. When electrons obtain enough energy to leave the well, they contribute to the device current. The number and levels of discrete energy states in a well can be changed by the variations in the depth and width of the well. Absorption of LW radiation in a wide quantum well can originate from bound to bound state transitions [3]. Thus, when a photon hits the quantum well with energy equal or greater than the energy difference between the two states, an electron in the ground state is excited to the first excited state. Via an applied voltage, these excited electrons can be extracted (and thus can contribute to the photocurrent). The energy levels and thus the absorption wavelength can be adjusted by changing thickness of constituent well (GaAs) and barrier ($\text{Al}_x\text{Ga}_{1-x}\text{As}$) layers. The schematic diagram of GaAs/AlGaAs QWIP is shown in figure 1.7.

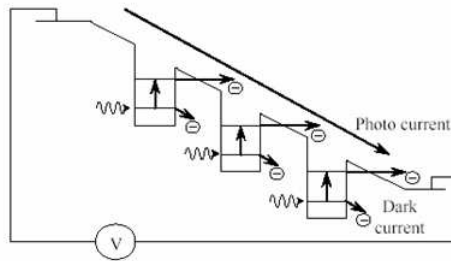


Figure 1.7: Schematic diagram of GaAs/AlGaAs QWIP

GaAs/AlGaAs QWIPs have the following advantages:

- Use of standard manufacturing techniques based on mature GaAs growth and

Chapter 1. Introduction

processing techniques

- Highly uniform and well-controlled MBE growth on large substrates(6")
- GaAs wafers are low cost, and have high thermal stability

However, QWIP detectors have high values of thermally generated dark current which is caused by electron tunneling between wells, resulting in a low signal-to-noise ratio. Due to intersubband transitions in QWIPs, LWIR QWIPs have performance limitation especially at higher temperatures ($>70 K$). Also, due to absorption selection rules, optical transition is forbidden for normal incidence of light; this limitation is usually overcome by the incorporation of a grating on the detector surface, however this drastically limits the quantum efficiency (typically less than 10%) [4].

InSb detectors

Indium antimonide (InSb) is one of the most highly developed and widely used detector materials for the near-infrared portion of the spectrum (1 to 5 μm). InSb is a member of the III-V semiconductor materials. The crystal structure of pure InSb is cubic zinc-blend. The p-type material is formed if more indium is used in the compound and an n-type material is formed if more antimony is used. Indium material is an intrinsic semiconductor with a direct room energy band-gap of 0.17 eV. Thermally generated carriers are the dominant noise source at high temperature requiring InSb detectors to be cryogenically cooled. Large uniform substrates are available allowing for fabrication of large area FPAs (1024 \times 1024 pixels). InSb detectors are used in forward looking infrared heat seeking missiles and thermal imaging. The drawbacks of the material system include the cooling requirement, the material specific cutoff wavelength limit and the tendency of the FPA characteristics to drift between uses.

Type-II InAs/(In)GaSb SL detectors

InAs/(In)GaSb can be considered as an alternative to HgCdTe and GaAs/AlGaAs QWIP IR detectors. Thin layers of InAs and GaSb have slightly different lattice constants and when brought together, form a strain layer superlattice (SL) with the lattice match taken up by the biaxial strain in the plane of two layers. The heterojunction of InAs and GaSb has a type-II broken bandgap where the conduction band of InAs is 0.129 eV lower than the valence band of GaSb. The heterojunction formed between InAs and GaSb in SL is shown in figure 1.8. Band structure parameters for InAs, and GaSb are summarized in Table 1.2 [5, 6, 7]

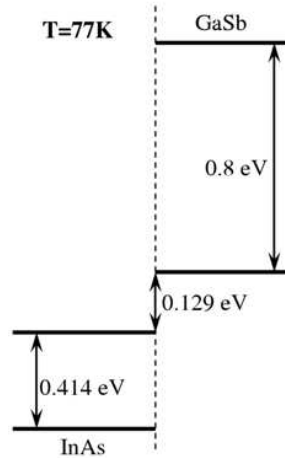


Figure 1.8: Heterojunction formed by InAs and GaSb

Due to the type II band alignment, the electron and hole wavefunctions are localized in InAs and GaSb, respectively. The bandgap of SL structures is determined by the energy difference between the electron miniband and the first heavy hole state at the Brillouin zone center and can be changed in the range of 0 to 250 meV . The schematic of band edge diagram of InAs/InGaSb SL is shown in figure 1.9 [2].

The optical absorption in InAs/GaSb SL is related to the overlap of electron and

Chapter 1. Introduction

Table 1.2: Some important parameters for InAs and GaSb at 300 K

Parameters	InAs	GaSb
Lattice constant (\AA)	6.0583	6.0959
Energy gap (eV)	0.356	0.725
Valence band offset (eV)	0.56 (300 K) 0.482 (77K)	0
Electron mobility ($cm^2/V.s$)	20000	5000
Hole mobility ($cm^2/V.s$)	480	880
Dielectric constant	15.15	15.69
m_e/m_0	0.0183	0.042
m_{hh}/m_0	0.263	0.222
m_{lh}/m_e	0.0247	0.045
m_{so}/m_e	0.0557	0.075

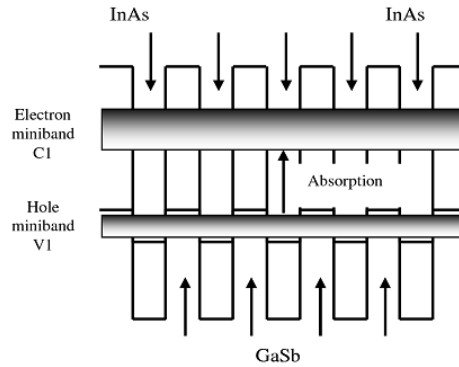


Figure 1.9: Band edge diagram illustrating the confined electron and hole minibands which form the energy band gap.

hole wavefunctions. Thin layers of SL have large overlap wavefunctions and therefore large absorption coefficients. The overlap between the wavefunction appear near the hetero-interfaces and therefore the optical absorption is restricted to the vicinity of interfaces [8]. From the mentioned characteristics of InAs/GaSb SL, one can conclude that by atomic engineering of the superlattice interfaces and by changing the thicknesses of InAs and GaSb, we can change the detector cutoff wavelength from 3 to more than 40 μm . The main advantages of SL are as following:

Chapter 1. Introduction

- Normal incidence absorption due to interminiband transitions
- Tunable cutoff wavelengths due to adjustable bandgap
- Supression of Auger related dark current based on SL band structure engineering [9] (quantum confinement and large splitting of heavy-hole and light-hole valence subbands in SL)
- Reduction of tunneling currents due to large electron effective mass
- High uniformity due to mature III-V semiconductor materials growth techniques

All of the above features lead to higher operation mode for SL photodetectors as compared to the state of the art HgCdTe detectors, InSb detectors, and QWIPs.

InAs/(In)GaSb SL detectors have been reported by different groups in MWIR, LWIR, and VLWIR regions. Table 1.3 provides an overview of different SL single pixel detector performance results.

1.5 Conclusion

General concepts concerning infrared detection were presented followed by description of different technologies for infrared imaging. Thermal detectors have the advantage of room-temperature operation however, they have low sensitivity and are very slow as compared to the photon detectors. IR detector figures of merit were discussed in detail. Competitive third generation FPAs material systems were covered with their disparate strengths and weaknesses, providing motivation for other material systems to overcome the present photon detector limitations. Detectors based on InAs/GaSb SL were presented as an alternative technology which has all

Table 1.3: A summary of reported MW/LW/VLW IR

Superlattice type	Device type	λ_c	η	D^* [Jones]	Ref.
12ML InAs/7ML GaSb	P-on-n	10 μm	46%		[10]
14ML InAs/7ML GaSb	Barrier type	9.9 μm	29%	10^{11}	[11]
16ML InAs/9ML GaSb	Barrier type	14 μm	17.5%	10^{10}	[12]
8ML InAs /11ML GaSb	n-on-p	5 μm @ 300 K	25%	10^9	[13]
9ML InAs /4ML GaSb	n-on-p	7 μm @ 77 K	12- 32%	10^{12}	[14]
14ML InAs/7ML GaSb	n-on-p	11 μm	36%		[15]
W-Structure 14ML InAs/9ML GaSb 14ML InAs/7ML Al _{0.4} Ga _{0.49} /In _{0.11} Sb	p-on-n	10.5 μm @ 78 K	20- 34%		[16]
M-Structure 18ML InAs/3ML GaSb /5ML AlSb/3ML GaSb	n-on-p	10.5 μm @ 77 K	27%		[16]
Dual band	nBn	4.5 μm and $\sim 8\mu\text{m}$			[17]
Dual band	n-on-p	11 μm and $\sim 17\mu\text{m}$	4-5%		[18]

of the advantages of the state of the art photon detectors as well as potential to overcome the existing limitations in the competing technologies. It has principal advantages like flexibility of the material system allowing multispectral detection, lower tunneling currents due to higher electron effective masses and mature III-V epitaxial growth technology.

The recently proposed nBn heterostructure design has demonstrated a 100 K increase in background-limited infrared photodetection (BLIP) for InAs-based device, by decreasing Shockley-Read-Hall generation currents and by suppressing surface currents using specific processing.

Chapter 1. Introduction

Third generation IR detectors have three main emphasis, High operating temperature (HOT), multicolor capability, and large format arrays. This work concentrates on multicolor and HOT IR detectors based on nBn design. Contributions of this thesis include, 1) Development of design and growth procedure for the LW SL detectors leading to an improved detector performance. 2) Optical and electrical characteristics of single pixel devices in the MWIR, LWIR, and bi-color SL detectors. 3) Careful evaluation of carrier transport in SL in order to understand and improve SL device performance.

Chapter 2

Materials and Methods

2.1 Introduction

This chapter covers the design and experimental methods required for testing of infrared photodetectors. First, design tools for analyzing different SL systems and structures are introduced. Next section covers Molecular Beam Epitaxy (MBE) technique. MBE growth of SL material is the first step in the realization of IR photodetectors. X-ray diffraction (XRD) measurements are used to study the structural properties of as-grown material, and atomic force microscopy (AFM) is used to image and evaluate the surface morphology of the materials.

The bandgap of the as-grown materials is determined by optical absorption measurements. After growth and non-destructive structural and optical measurements, single pixel devices are processed using standard photolithography methods. The electrical behavior of the processed detectors was investigated by current-voltage (I-V) measurements. Detector performance also was characterized by spectral response and responsivity measurements.

2.2 Design tools

To lower the cost, and time associated with experimental processes used for testing SLs (growth, processing, characterization) first principle calculations were performed using commercially available softwares. These simulation are used to predict the band gap of the SL material and to optimize the designs to achieve the best device performance.

The main design parameters involving the SL material system are: the cutoff wavelength associated with different thicknesses of different SL constituent materials, and absorption of the SL which is directly related to the electron and hole wavefunctions overlap. To design the SL material system targeted at a specific region of the infrared spectrum as well as to study the absorption of that material system next-nano software is used. Next-nano software implements the 8×8 k.p modeling which is an approximation scheme for calculating the band structure (particularly effective mass) and optical properties of crystalline solids [19, 20, 21].

To study the device characteristics such as energy band alignment of the structures as well as dark current at different applied biases Sentaurus TCAD software is used. Sentaurus combines advanced, calibrated physical models, robust algorithms and numeric, and efficient meshing and structure editing capabilities to generate accurate and predictive simulation results.

- a. Nextnano software [22] is used generally for the simulation of electronic and optoelectronic semiconductor nanodevices and materials. For the design of the SLs 8×8 k.p method is used to generate the electron and hole wavefunctions in the SL layers. The 8×8 k.p provides the dispersion diagram of the simulated structure which the cutoff wavelength at different temperatures can be extracted. Figure 2.1(a) shows the conduction, heavy hole and light hole band edges as well as their respective ground state wavefunctions. Figure 2.1(b)

Chapter 2. Materials and Methods

shows the calculated ground state dispersion diagram of the electron, heavy hole and light hole of the same SL system.

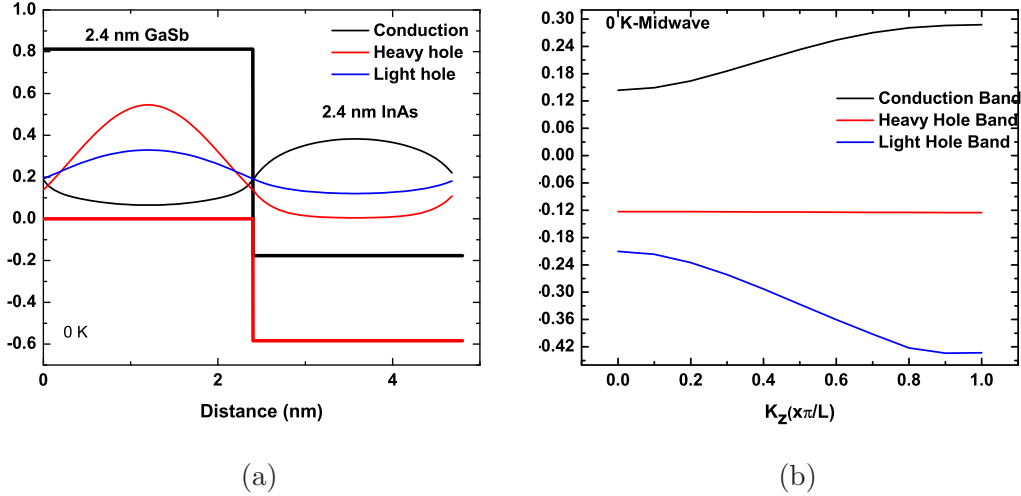


Figure 2.1: (a) wavefunctions (b) dispersion diagram at 0 K for 2.4nm GaSb/2.4 nm InAs.

- b. Sentaures Tcad software is used as a design tool to simulate different device structures. Using this software structures are generated using the graphical user interface which doping profiles and meshing strategies can also be defined. Generated structures can be used as an input file to a program written by the user to show electrical and optical characteristics. For SLs, band alignment and dark current of different structures with different materials and doping profiles are studied and simulated before designing the final structure. Figure 2.2(b) shows band alignment simulation of a pin MWIR SL detector which the doping profile is shown in figure 2.2(a).

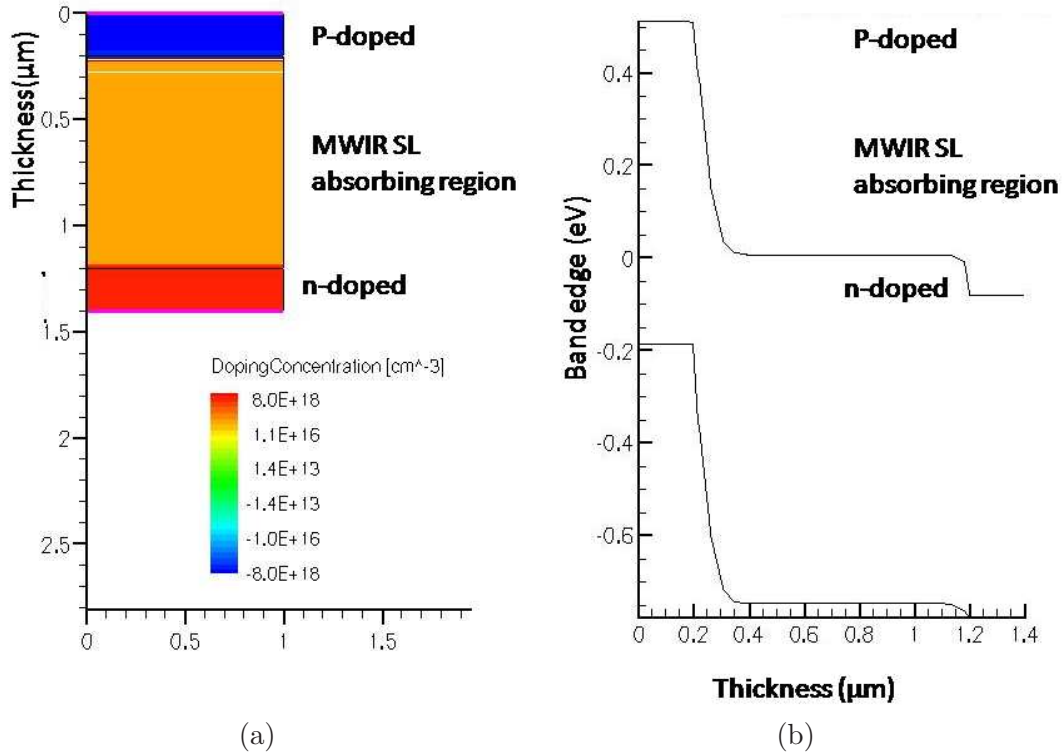


Figure 2.2: (a) doping profile (b) band alignment of a pin MWIR SL detector

2.3 Molecular Beam Epitaxy (MBE)

Molecular beam epitaxy (MBE) is a modern technique for growing III-V compound semiconductors as well as several other materials with atomic precision. MBE was invented by Alfred Cho of Bell Telephone Laboratories in the late 1960's. Molecular beam epitaxy takes place in high vacuum or ultra high vacuum (10^{-8} Torr). The most important aspect of MBE is the slow deposition rate, which allows the films to grow epitaxially. The slow deposition rates require proportionally better vacuum to achieve the same impurity levels as other deposition techniques. Since growth rates are typically less than an atomic monolayer per second and the beams can be shuttered in a fraction of a second, nearly atomically abrupt transitions from one material to another as well as good control of thickness, doping and composition can

be realized. Structures presented in this work were grown in solid source VG-80 MBE reactor, which consists of two identical growth chambers, preparation chamber and a load lock. Load lock is used to take samples in and out of the preparation chamber. To take out samples from the load lock, it must be vented to atmosphere, and to put samples back to chamber it needs to be pumped down with a mechanical pump and a turbo pump to vacuum (1×10^{-8} Torr). The preparation chamber is used for substrate transfer, substrate storage and substrate heating for initial outgassing. The preparation sample is equipped with a trolley system used to transfer samples between the preparation and growth chambers. The preparation chamber is equipped with an ion pump which allows to achieve pressure of $\sim 1 \times 10^{-10}$ Torr. Each of the growth chambers hold UHV level (pressure $\sim 10^{-10}$ Torr) which are equipped with an ion pump, a He closed loop cryopump and a Titanium sublimation pump. The stainless steel shroud around the growth chamber is filled with Liquid Nitrogen (LN₂) which captures residual gases in the chamber. Growth chamber is also equipped with the following: effusion cells, tools for in situ monitoring of growth process (Reflection High Energy Electron Diffraction (RHEED) gun, pyrometer for measuring substrate temperature and ion gauge for monitoring flux pressure during the growth process). Also it contains residual gas analyzer to monitor pressure of residual gases such as H₂O, CO₂, N₂ and CO. A schematic of MBE growth chamber is shown in figure 2.3.

2.3.1 Growth of InAs/GaSb superlattice

In order to achieve high signal-to-noise ratio in the photodetector, the quality of the SL interfaces has to be accurately controlled. In InAs/GaSb SL, two types of interfaces form grown along the [001] growth direction, the “InSb-like” or “GaAs-like” interface. The existence of these interfaces have been clearly shown by other research groups using scanning tunneling microscopy [23, 24]. Since the lattice constant of

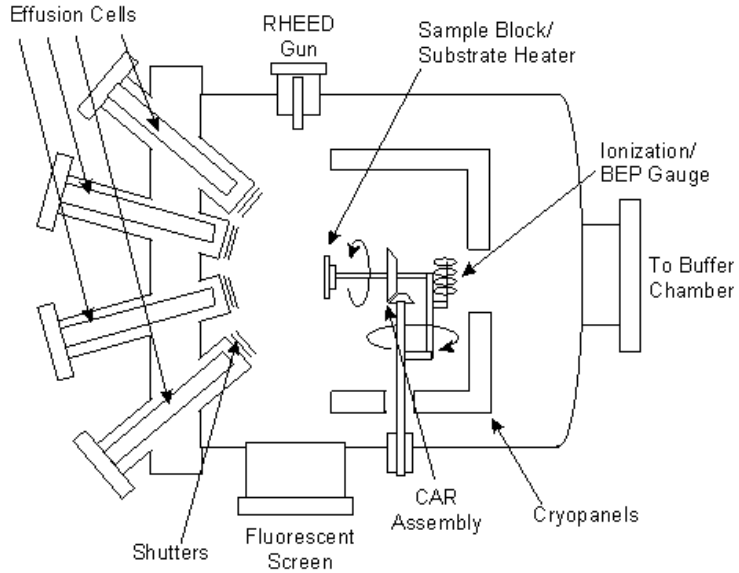


Figure 2.3: Schematic of a Molecular Beam Epitaxy growth chamber

InSb (GaAs) is much larger (smaller) than that of the GaSb substrate, insertion of a few monolayers of these materials leads to a large compressive (tensile) strain, thereby dramatically changing the structural, optical and electrical properties of the SL. Development of an optimized growth procedure for the strain-balanced SL with well-ordered constituent and interfacial layers is critical for the realization of a photodetector with a high absorption coefficient and reduced dark current. This study is done for midwave regime by introducing Sb and As soak times before GaSb and InAs respectively. The interface optimization for LWIR regime will be discussed in chapter 3.

2.4 X-ray diffraction

X-ray scans are used to determine the structural properties of the SLs. Double crystal X-ray diffraction (XRD) is a non-destructive technique for the structural characteri-

zation of thin crystalline films. When an X-ray beam bombards a crystalline lattice in a given orientation, the beam is scattered in a definite manner characterized by the atomic structure of the lattice. X-ray diffraction, occurs when the wavelength of X-rays and the interatomic distances in the lattice have the same order of magnitude. X-rays diffracted from an ordered array of scattering centres can give rise to interference maxima and minima. In order to observe x-ray diffraction from a crystalline lattice, the Bragg condition (equation 2.1) must be satisfied. When the waves are scattered from lattice planes separated by the interplanar distance d , the scattered waves interfere constructively. The path difference between two waves undergoing constructive interference is given by $2d \sin \theta$, where θ is the scattering angle. Therefore, Bragg's law is given as following:

$$2d_{h,k,l} \sin \theta = n \cdot \lambda \quad (2.1)$$

Where $d_{h,k,l}$ is the distance between the atom planes (h, k, l are the Miller indices), θ is the incident angle, n is the order of diffraction and λ is X-ray wavelength.

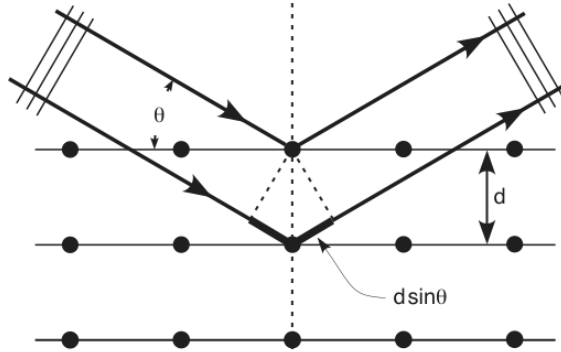


Figure 2.4: Schematic diffraction of X-rays in the crystal

X-ray scans in this work were performed with a Philips double-crystal X-ray diffractometer using the $\text{Cu-K}_{\alpha 1}$ line.

A typical XRD spectrum from InAs/GaSb SL is presented in figure 2.5 .

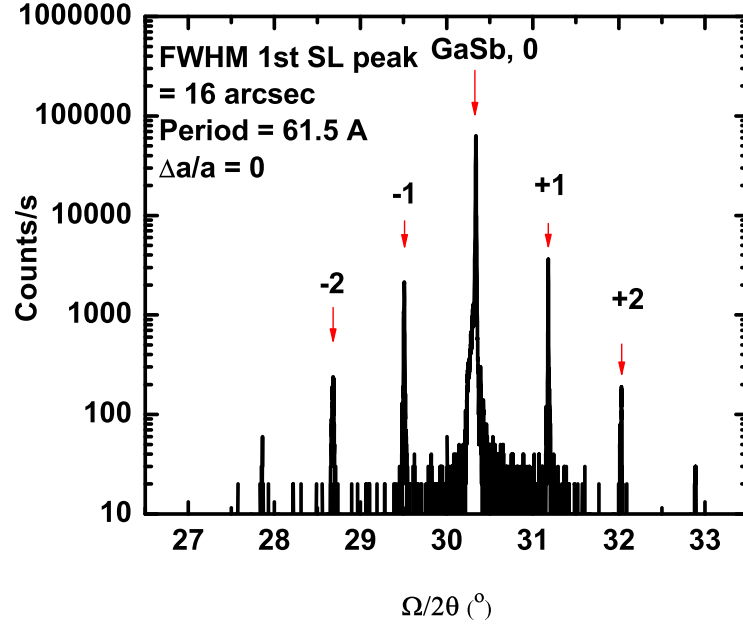


Figure 2.5: Typical XRD spectrum from InAs/GaSb SL

Parameters, which can be extracted from this spectrum, are:

- a. Lattice constant of substrate and average lattice constant of the SL can be obtained using the following equation:

$$a = \frac{n\lambda}{2 \sin \theta} \quad (2.2)$$

Where n is equal to 1, λ is known and equal to 1.5406 \AA , angle θ can be determined directly from the XRD spectrum. For the SL average lattice constant angle θ is corresponding to SL zero order peak.

- b. Strain relation between substrate and epilayer which can be found from the following equation:

$$\frac{\Delta a}{a_s} = \frac{a_e - a_s}{a_s} = \frac{\sin \theta_e - \sin \theta_s}{\sin \theta_s} \quad (2.3)$$

Chapter 2. Materials and Methods

Where a_s and a_e correspond to the lattice constants of the substrate and the epi-layer respectively.

- c. Superlattice thickness can be achieved from different methods. One of the methods proposed by Biefeld et al [25] is to calculate the superlattice period P as:

$$P = 4Nd_0 \quad (2.4)$$

Where

$$N = \frac{nd}{4(d_0 - d_n)} \quad (2.5)$$

here n is the diffraction order, $d_0(d_n)$ is the distance between atomic planes for different diffraction orders. For the SL presented in the figure 2.5 average value of period was found to be 6.15 nm which is in good agreement with the value extracted from the Bragg's law.

The above method for the determination of SL period thickness can be formalized and implemented as a computer program . Rocking curves presented in this work were analyzed with an automated algorithm based on the dynamical theory of diffraction (Bede RADs software).

- d. Full-Width at Half-Maximum (FWHM) is a good qualitative measure of crystalline quality of the structure. Narrow and symmetrical SL peaks indicate perfectly ordered structure with compositionally abrupt interfaces. On the contrary, broad and asymmetrical satellite peaks indicate variation of period thickness and growth defects accumulating at the interfaces of SL. Typically, FWHM for the first satellite peak of SL is calculated.

2.5 Atomic Force Microscopy (AFM)

Atomic force microscopy (AFM) is used to study the morphology of GaSb buffer layer as well as the SL grown on the top of the buffer layer. Atomic force microscopy (AFM) is a surface imaging technique, providing the topographic information of the surface with nanometer resolution. An AFM unit is mainly composed of a laser diode, a flexible cantilever, a piezoelectric motor, and a position-sensitive photodetector, as shown in figure 2.6. AFM is designed on the basis of the atomic force between the tip and sample surface. A sharp tip is mounted on a flexible cantilever, a few angstroms away from the sample surface. The repulsive Van der Waals force between the tip and the surface causes the cantilever to deflect. The motion of the cantilever is magnified by a laser beam reflection and recorded as the vertical displacement of the tip. In this way, the surface topography can be imaged by scanning the tip over the sample surface. AFM is typically operated in one of the two basic modes: contact mode or tapping mode. Contact mode is a fast and convenient way of imaging a relatively hard surface, but the drawback for this mode is that there are large lateral forces on the sample as the tip is dragged over the surface. In tapping mode, on the other hand, the cantilever is oscillated at or near its resonant frequency (often hundreds of kilohertz), and the tip gently taps the surface with a significantly reduced contact time. Tapping mode is thus extremely useful for topographical imaging of soft samples. To study the SL and GaSb growth quality, RMS roughness was studied through AFM measurements.

2.6 Absorption measurements

To verify the cutoff wavelength of a specific designed SL, absorption measurement are used. To conduct an absorption measurement a sample is loaded onto a sample

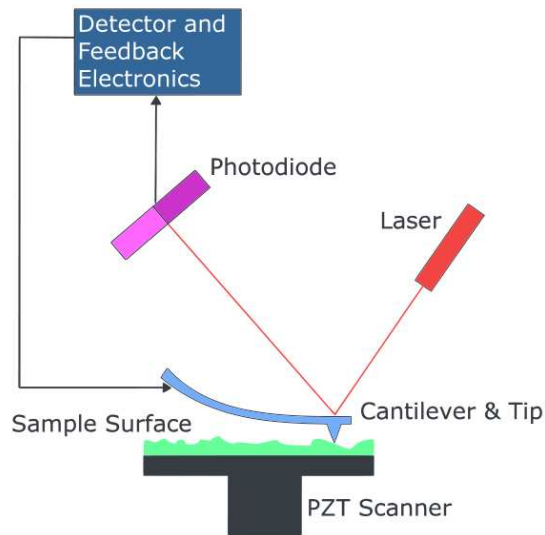
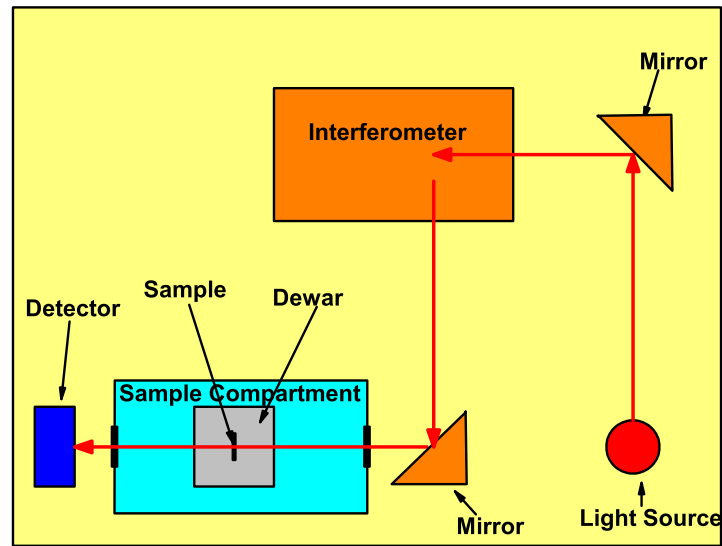


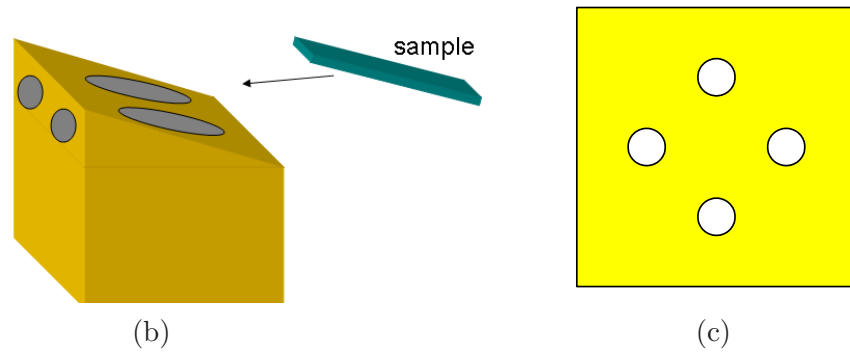
Figure 2.6: Essential components of atomic force microscopy (AFM)

holder which is then loaded in the main compartment of the FTIR. Prior to this, a background measurement is taken of either atmospheric conditions or the sample's substrate. The percent transmission is the ratio of the signal transmitted through the sample and the background measurement signal multiplied by 100%. The absorption is then computed as $100\% - \text{transmission}$.

The sample can either be loaded into a room temperature sample holder or a liquid nitrogen cooled dewar. The room temperature sample holder is a simple metallic stand with a hole in it. The sample is held in place over the hole with a magnetic strip. The liquid nitrogen cooled dewar, as shown in figure 2.7, has a normal incident sample holder, figure 2.7(c), and a Brewster angle sample holder, figure 2.7(b). The samples are held in place using thermal grease or indium.



(a)



(b)

(c)

Figure 2.7: (a) Optical absorption measurement set-up, sample holder is loaded in the main compartment of the FTIR (b) Brewster angle sample holder (c) Normal incidence sample holder

2.7 Processing

The next step after the growth of the material is the processing. For determining the quality of FPA, single pixel devices are tested. The processing of single pixel detectors are divided in to three steps of: top contact metalization, mesa isolation, and bottom

Chapter 2. Materials and Methods

contact metalization. Optical photolithography is a common step for formation of top, bottom and mesa isolation. The typical steps in a photolithographic process are: wafer cleaning, dehydration bake, adhesion promoter application, photoresist application, soft bake, exposure and develop cycle. Wafers are cleaned consecutively in acetone, isopropanol (IPA) and de-ionized (DI) water (5 minutes each) and then blow dried with nitrogen (N_2). After cleaning, dehydration bake is performed to drive off most of the adsorbed water on the surface of the wafer. The dehydration bake is for 6 minutes at 150 degrees. Immediately after the bake, the wafer was primed with hexamethyldisilazane (HMDS), which acted as an adhesion promoter. After applying HMDS, resist is applied at the top. For the top metalization positive photoresist was spun on the wafer. After resist application, the wafer was baked at 90 degrees for 90 seconds. The purpose of this step is to drive off most of the solvents in the resist. After bake, the wafers are exposed with the mask aligner using mask 1 as shown in figure 2.8(a). After the exposure the sample was baked, then flood exposed again without the mask for resist reversal. After the final exposure, the sample was developed leaving the photoresist in the desired places for metal deposition. After photolithography, the metal contact is deposited. We used Ti (500 Å)/Pt (500 Å)/Au (3000 Å) to achieve ohmic contact. The next step is the mesa isolation etch. The photolithographic steps for the mesa isolation etch are similar to the steps used for top contact metallization. First the sample is pretreated and primed. Then positive resist was spun on and baked. Using Mask 2 in figure 2.8(b) the sample was exposed on the mask aligner. After that samples are etched (it can be both wet etched or dry etched) to the bottom contact layer. After the mesa isolation etch, photoresist was applied as it was for the top contact metallization except Mask 3 in figure 2.8(c) was used. The bottom contact metal is Ti (500 Å)/Pt (500 Å)/Au (3000 Å) is then applied. Finally the sample is soaked in acetone for lift-off. The final mesa size of a single-pixel device is $410 \times 410 \mu\text{m}$. To study the effect of surface leakage current on the performance of a single pixel, devices with aperture

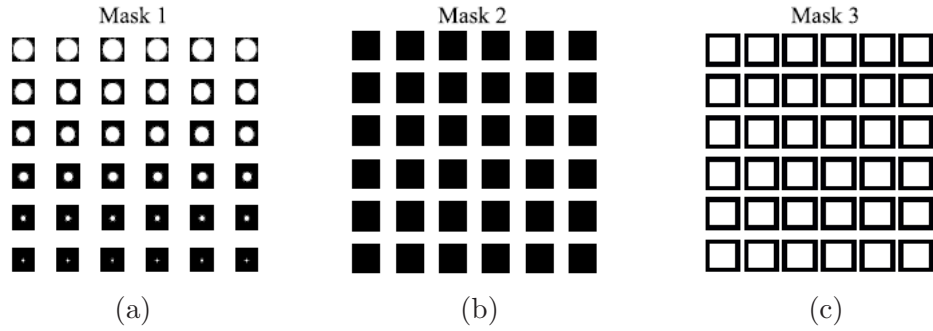


Figure 2.8: Schematics of the masks used in fabrication process of the superlattice detectors

diameters of 300, 200, 150, 100, 50 and 25 μm are fabricated. The schematic of the fully processed single-pixel photodiode with contact metallization is shown in figure 2.9.

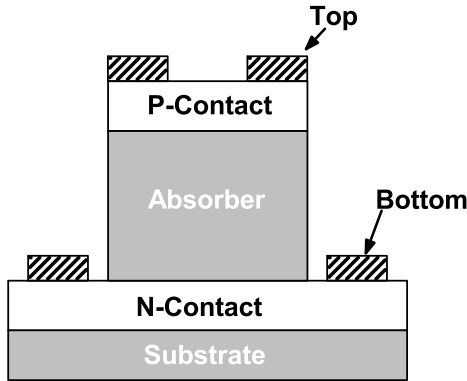


Figure 2.9: Conventionally processed pin diode

2.8 Characterization

After processing, devices were cleaved and wire-bonded to a leadless chip carrier (LCC). To evaluate the electrical and optical performance of photodetectors the de-

Chapter 2. Materials and Methods

vice to be tested was placed in a close-cycle Helium cryostat. Bias dependent dark Current-voltage measurements were performed using a semiconductor parameter analyzer. The dark current was measured with a cold radiation shield, which was painted black to avoid signals due to reflections. From the dark current measurements, we can determine the dynamic resistance:

$$R_d A = A \left(\frac{dI}{dV} \right)^{-1} \quad (2.6)$$

where A is the mesa area, and the derivate is calculated from the measured dark current. Spectral response measurements were performed on devices at temperatures ranging from 50 K to 300 K using a Nicolet 670 Fourier transform infrared (FT-IR) spectrometer and a Keithley 428 preamplifier. The FTIR contains a glow bar source, a Michelson interferometer with a movable mirror, and internally mounted Deuterated Triglycine Sulfate (DTGS) thermal detector. For the spectral response measurement, the IR beam is directed outside of the FTIR off of a parabolic mirror and onto the detector mounted in the close-cycle He cryostat. Relative spectral response was obtained by dividing the photocurrent of the SL detectors with that obtained using a calibrated DTGS thermal detector [26]. A schematic of the spectral response is shown in figure 2.10.

The responsivity R of a photodiode characterizes its performance in terms of the photocurrent generated per incident photon flux which is estimated using radiometry.

$$R = \frac{signal}{\Phi_e}. \quad (2.7)$$

Spectral responsivity of the detector is calculated by:

$$R(\lambda) = R_{max} NR(\lambda) \quad (2.8)$$

where ($NR(\lambda)$) is the normalized spectral response and multiplied by the peak responsivity (R_{max}).

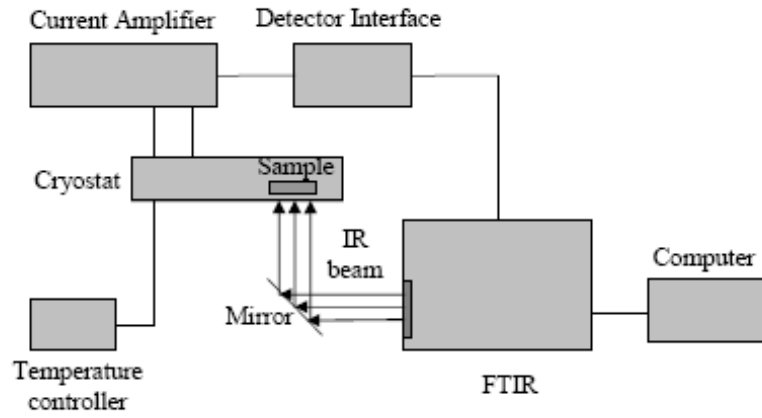


Figure 2.10: Spectral response measurement setup

To measure reponsivity, infrared radiation from a black body source with controllable temperature is directed through a chopper onto the SL detector mounted inside the dewar. The electrical signal produced by the detector is then aplimfied by a Keithley amplifier and measured using a network analyzer. The radiant power from the blackbody can be calculated by:

$$\Phi_e = \int_0^{\infty} M_{e,\lambda}(\lambda, T) \cdot A_{bb} \cdot \frac{A_{det}}{r^2} d\lambda \quad (2.9)$$

Where $M_{e,\lambda}$ is the radiant existence, A_{bb} is the area of the blackbody aperture, A_{det} is the area of the detector and r is the distance from the blackbody to the detector. A schematic of the responsivity setup is shown in figure 2.11.

The maximum responsivity can be calculated from:

$$I(Amps) = \int_0^{\lambda_{cut}} M_{e,\lambda}(\lambda, T) \cdot A_{bb} \cdot \frac{A_{det}}{r^2} \cdot NR(\lambda) \cdot R_{max} d\lambda. \quad (2.10)$$

Solving for R_{max} ,

$$R_{max} = \frac{I}{A_{bb} \cdot \frac{A_{det}}{r^2}} \cdot \int_0^{\lambda_{cut}} M_{e,\lambda}(\lambda, T) \cdot NR(\lambda) d\lambda \quad (2.11)$$

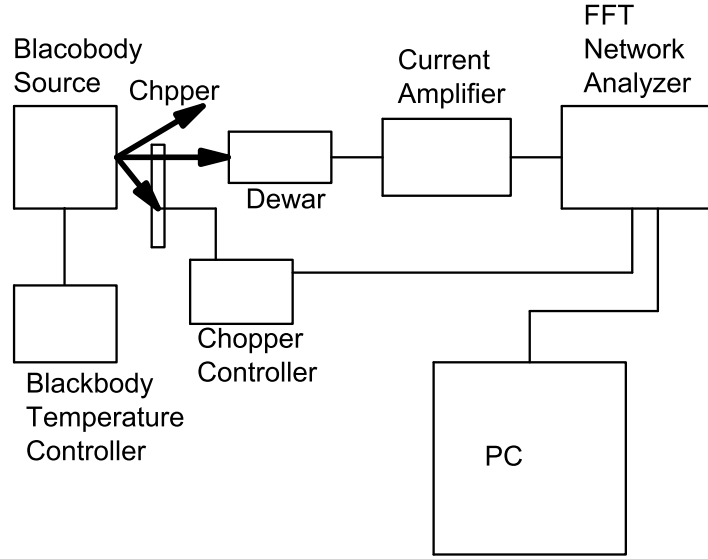


Figure 2.11: Responsivity measurement setup

From R_{max} quantum efficiency, other figure of merit of the detectors, can be calculated,

$$\eta(\lambda) = \frac{R_{max}NR(\lambda)hc}{\lambda q}. \quad (2.12)$$

Detectivity can be found using

$$D^* = \frac{R(\lambda)\sqrt{Ad}}{i_n/\sqrt{\Delta f}} \quad (2.13)$$

where i_n is the current noise measured by the spectrum analyzer when the blackbody is no longer incident on the detector and Δf is given by

$$\Delta f = \frac{1}{2\tau_{AVG}} \quad (2.14)$$

where τ_{AVG} is the integration time of the measurement.

2.9 Conclusion

In this chapter we discussed growth, processing and characterization of InAs/GaSb SL infrared single-pixel detectors. Detailed description of characterization techniques used in this work and their applications for structural, optical and electrical characterization of as grown materials and processed devices were presented. Physical foundations underlying X-ray diffraction, atomic force microscopy and transmission measurements were discussed. Schematic of experimental set up used for spectral response, transmission, and responsivity measurements were presented.

Chapter 3

Mid-wave and Long-wave pin and nBn SL detectors

3.1 Introduction

In this chapter the design, growth, processing and characterization of single pixel midwave pin InAs/GaSb SL detectors will be described. Next, longwave SL design and growth optimization will be covered. Definition and advantages of the nBn devices will be discussed. Growth, processing and characterization of single pixel longwave pin and nBn InAs/GaSb SL detectors are also presented. I-V characteristics and responsivity of the longwave nBn detector are compared with a pin photodiode with the same absorber region structure. The nBn exhibits lower dark current density than the pin diode at equivalent applied electric field. The unique processing of the nBn detector and the consequent removal of the sidewall surface, as well as the depletion region width shrinking result in lower dark current densities in nBn devices.

3.2 Midwave superlattices (MW SLs)

3.2.1 Design and growth of MW SLs

8 MLs of InAs and 8 MLs of GaSb was used for all of the MW SL designs. Nextnano simulations of this material system is shown in figure 3.1. As it is shown in figure 3.1(a) the electron wavefunction is defined in the InAs layer where as hole wavefunction is mostly confined to the GaSb layer. Figure 3.1(b) shows the dispersion diagram for 8 MLs InAs/8 MLs GaSb at 0 K indicating a cut off wavelength of 4.6 μm .

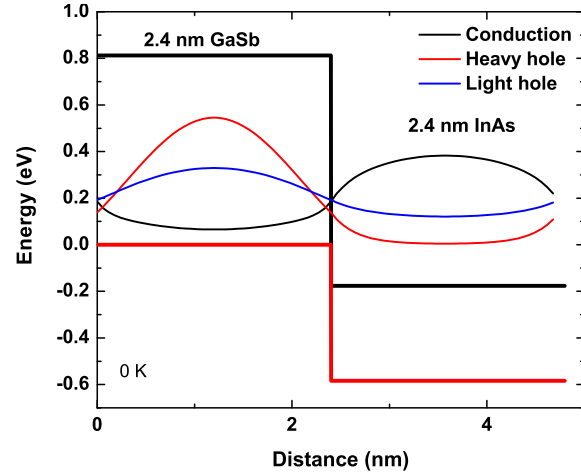
3.2.2 Calibration of the group III elements for SL growth

Reflection high energy electron diffraction (RHEED) oscillations are used to calibrate the group III cells during the MBE growth. For the purpose of exact growth rates for the SL growths, a method proposed by Kaspi et al [27] was utilized for tuning of group III sources. Two calibration samples with structures formed by different binary III-V compounds (InAs and GaSb, AlSb and GaSb etc.) with different periods were grown under the same growth conditions. Then from the spacing between the satellite fringes in the scans, the exact growth rates can be determined by solving the following system of equations (3.1 and 3.2),

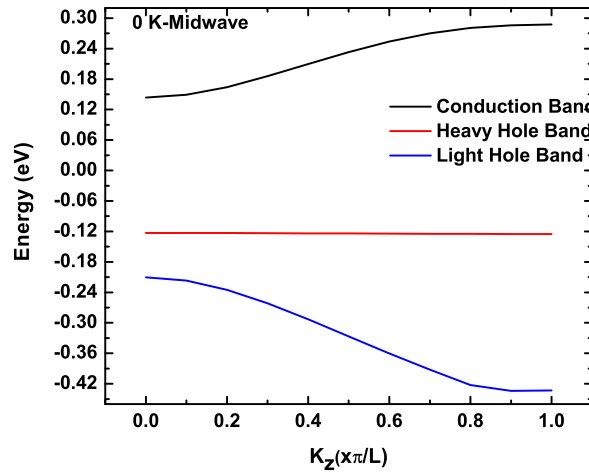
$$r_{Ga} \cdot t_{Ga} + r_{In} \cdot t_{In} = T_1 \quad (3.1)$$

$$r_{Ga} \cdot t_{Ga} + r_{In} \cdot t_{In} = T_2 \quad (3.2)$$

where T_1 and T_2 are the SL periods determined from the (004) X-ray scan, r_{Ga} and r_{In} are the growth rates of Ga and In, and t_{Ga} and t_{In} are the times of Ga and In deposition, respectively.



(a)



(b)

Figure 3.1: (a) electron and hole wavefunctions (b) dispersion diagram at 0 K for 2.4 nm GaSb/2.4 nm InAs.

This method is illustrated in figure 3.2 for In and Ga sources. One calibration sample with 50 periods of 8ML InAs/8ML GaSb SL and 50 periods of 8ML InAs/12ML GaSb SL was grown on GaSb substrate. Symmetric (004) X-ray scans were performed on the samples with a Philips double-crystal X-ray diffractometer and growth rates were determined as $r_{Ga} = 0.48$ ML/s and $r_{In} = 0.29$ ML/s.

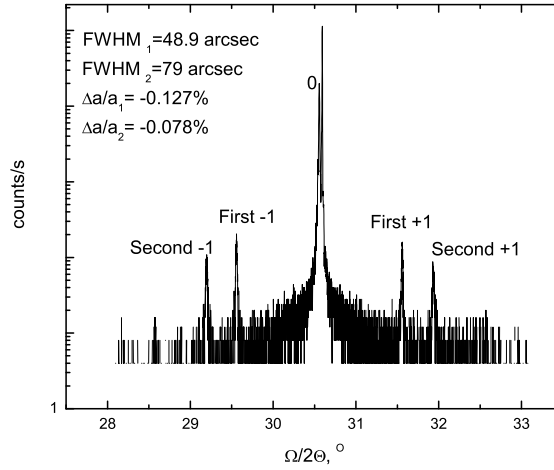


Figure 3.2: Estimation of the growth rates by X-ray scan of SLs width different period

3.2.3 MW SL growth optimization

As mentioned in the previous chapter, interfaces are one of the key elements in the growth of the SLs. Growth of MW SLs has been previously developed in our group and 2 seconds of As before 8 MLs of InAs layer and 12 seconds of Sb before 8 MLs of GaSb layer provide the optimum interface conditions for the MW SLs. Figure 3.3 shows the shutter sequence used for th MW SLs. More details on the MW SL growth conditions can be found in [28].

3.3 Midwave pin InAs/GaSb SL detector

3.3.1 Growth

All of the structures in this chapter were grown on Te-doped epi-ready (100) GaSb substrates. The structure consisted of a 360 nm thick bottom contact layer formed by

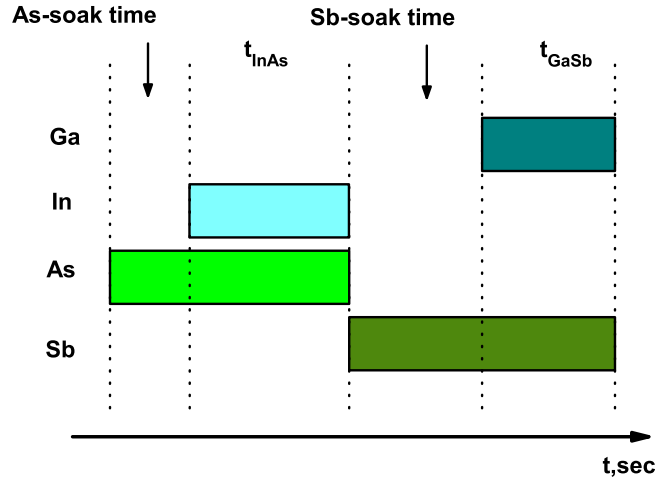


Figure 3.3: shutter sequence for the growth of MW SLs

8 MLs InAs:Si ($n = 4 \times 10^{18} \text{cm}^{-3}$) / 8 MLs GaSb SL followed by 192 nm thick doping graded layers of 8 MLs InAs:Si / 8 MLs GaSb SL to achieve doping concentration of $n = 1 \times 10^{17} \text{cm}^{-3}$ before the absorbing layer. Then a 1.3 μm thick absorber formed by 8 MLs InAs/8MLs GaSb SL was grown followed by 192 nm thick p-doping graded layers. The structure was terminated by a 50 nm thick GaSb p-type ($p = 4 \times 10^{18} \text{cm}^{-3}$) top contact layer with the same composition as the bottom contact layer. A schematic of the structure is shown in figure 3.4

3.3.2 Processing

The devices were processed using $410 \times 410 \mu\text{m}^2$ square mesas with circle apertures with varying radii from 25 to 300 μm . Processing was initiated by standard optical photolithography for top contact metal deposition. Then, ICP dry etch to the middle of the bottom contact layer was performed. SiN passivation was performed for pin detectors in this chapter. Finally, samples were patterned and bottom contact metal was deposited. Ti/Pt/Au (500/500/3000 Å) were used as contact metals for both

GaSb(p) 50 nm
SLS InAs/GaSb 8x8 MLs 192 nm graded doping
InAs/GaSb 8x8 MLs 1.3 μm nid
SLS InAs/GaSb 8x8 MLs 192 nm graded doping
SLS InAs/GaSb 8x8 MLs 360 nm n-doped
GaSb:Te

Figure 3.4: A schematic of pin InAs/GaSb SL MWIR detector

top and bottom contacts. A schematic of processed pin structure is shown in figure 3.5.

3.3.3 Characterization

Current-voltage measurements were obtained using a semiconductor parameter analyzer. Figure 3.6(a) presents the dark current density of MW SL pin detector at different temperatures ranging from 77 K to 300 K . The data shows current density of 1.34×10^{-6} at -0.3 V which indicates the low level dark current density of the device which is comparable to the lowest published dark current densities reported by other groups [13, 29].

Spectral measurements were performed at temperatures ranging from 77 K to

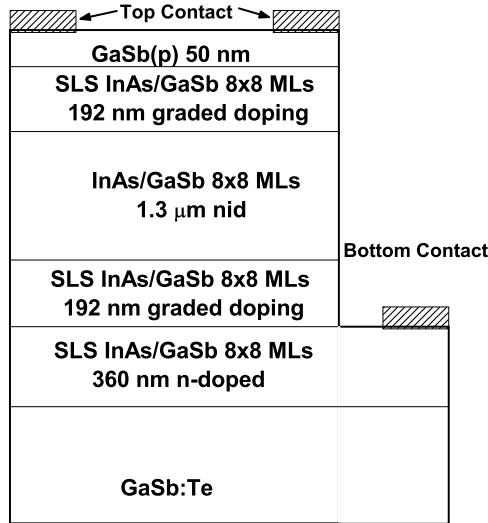


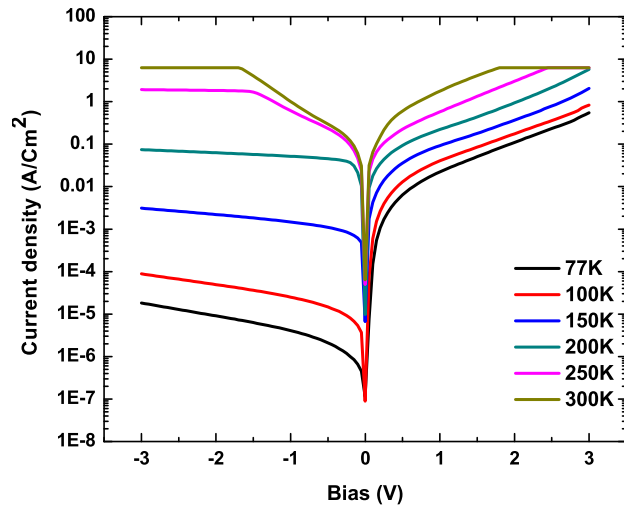
Figure 3.5: A schematic of processed MW SL pin detector

300 K using a Nicolet 670 Fourier transform infrared (FT-IR) spectrometer and a Keithley 428 preamplifier. Relative spectral response was obtained by dividing the photocurrent of the 300 μm -diameter aperture SL detectors with that obtained using a calibrated [26] deuterated triglycine sulfate (DTGS) thermal detector. A cut off wavelength of $\lambda_{c1} \sim 4.5 \mu\text{m}$ was seen at 77 K (figure 3.6(b)) which is in great agreement with the nextnano simulations.

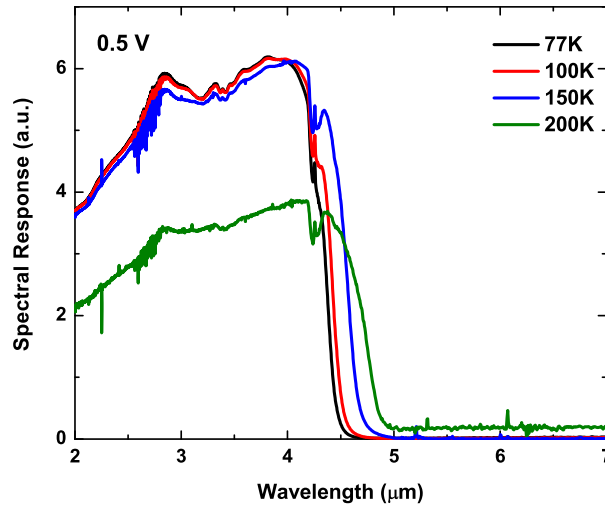
3.4 Longwave SLs

3.4.1 Design of the LW SLs

13 MLs of InAs and 7 MLs of GaSb was used for the LW SL designs. Nextnano simulations of this material system are shown in figures 3.7(a) and (b). Similar to the MW SL, the electron wavefunction is defined in the InAs layer where as hole wavefunction are defined in the GaSb layer (Figure 3.7(a)). Figure 3.7(b) shows



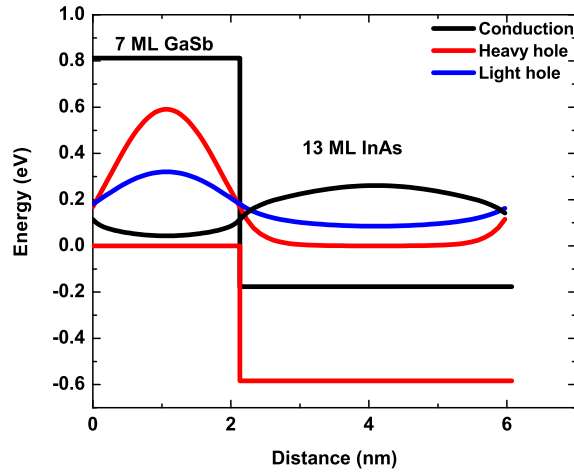
(a)



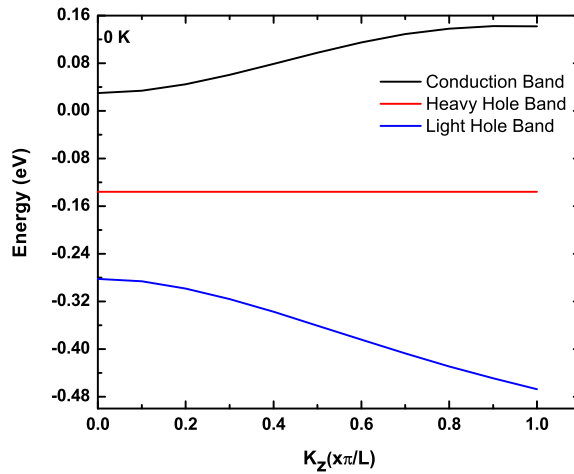
(b)

Figure 3.6: (a) Dark current density, and (b) spectral response of MWIR pin SL detector

the dispersion diagram for 13 MLs InAs/7 MLs GaSb at 0 K which indicates a cut off wavelength of 7.48 μm. Since InAs is -0.6% lattice mismatched to GaSb, InSb is used as strain compensating layer which shifts the cutoff wavelength to 8.3 μm (figures 3.8(a) and (b)).



(a)



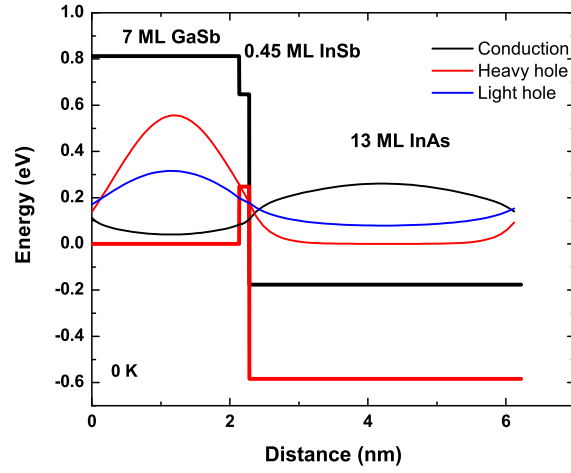
(b)

Figure 3.7: (a) band alignment, and electron/hole wavefunctions (b) dispersion diagram of 13 MLs of InAs and 7 MLs of GaSb

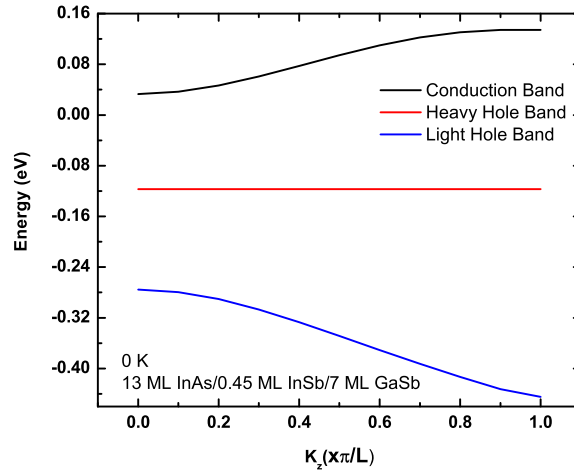
Optical absorption in semiconductor materials is proportional to the overlap between the of electron and hole wavefunctions which is described as following:

$$\alpha \propto |\langle \Phi_e | \Phi_h \rangle|^2 = \left| \int_{SLperiod} \Phi_e \cdot \Phi_h^* dr \right|^2 \quad (3.3)$$

Where Φ_e and Φ_h refer to the electron and hole wavefunctions, respectively. When the InAs layer thickness is increased to extend the cutoff wavelength of the SLs into



(a)



(b)

Figure 3.8: (a) band alignment, and electron/hole wavefunctions (b) dispersion diagram of 13 MLs of InAs, 0.45 ML of strain compensating layer of InSb and 7 MLs of GaSb

LW operation regime, the electron and hole wavefunctions overlap decreases which causes the absorption to decrease and therefore lowers the device performance. Figure 3.9 shows the electron and hole wavefunction overlap for 8 MLs GaSb/ X MLs InAs (X= 8, 10, 12, 14). The figure indicates that as the InAs layer thickness increases, the cutoff wavelength increases towards longer infrared spectrum and the electron

and hole wavefunction overlap decreases.

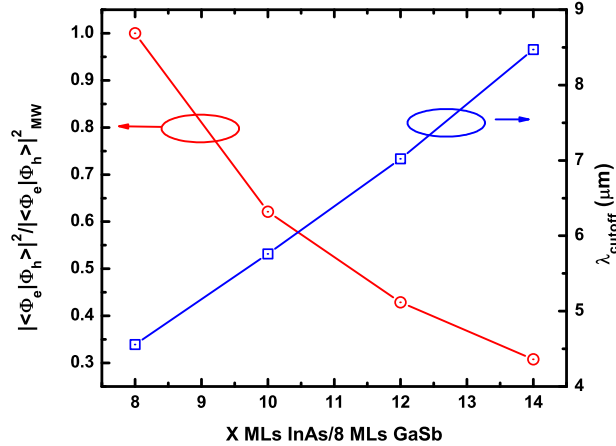


Figure 3.9: Electron and hole wavefunction overlap and cutoff wavelength for 8 MLs GaSb/ X MLs InAs (X= 8, 10, 12, 14).

Different material systems or strain compensating layers can be designed to overcome the LW SL absorption challenge. One possible way is to use the ternary InGaSb instead of GaSb layer to increase the electron and hole wavefunctions overlap.

3.4.2 Growth optimization of InAs/GaSb SLs for LWIR region

As it was discussed earlier, the quality of the SL interfaces is one of the important factors in growth of the SL detectors since the “InSb-like” or “GaAs” like interfaces can dramatically influence the device performance. For MWIR (3-5 μm) regime, it was shown [28] that combination of Sb (12 sec) and As (2 sec) soak times as strain compensating layers during SL growth provides the best structural properties in terms of lattice mismatch between the SL and the GaSb substrate as well as the lowest full width half maximum (FWHM) of the first SL satellite peak.

In this section, the influence of the thickness of the InSb layer formed at the GaSb-on-InAs interface and the growth temperature on the structural and optical quality of type-II InAs/GaSb SL designed to operate in LWIR range is discussed.

To optimize the growth of strain-balanced SL, two methods were undertaken. In the first approach, an InSb layer was intentionally grown between the binary compounds in each SL period to suppress the natural tensile strain of the InAs layer on GaSb-layer [30]. In second approach, the strain compensation was achieved by forming “InSb-like” interfaces on InAs layers using an “Sb soak” that enabled preferential group V exchange on the growth front. Structural quality of this material was studied using high resolution X-ray diffraction (HRXRD) and cross sectional scanning transmission electron microscopy (STEM) whereas surface morphology and optical quality was assessed by atomic force microscopy (AFM) and Fourier transform infrared (FTIR) spectroscopy, respectively.

Experimental procedure

All of the structures presented in this study were grown on n-type (Te-doped with $n \sim 5 \times 10^{17} \text{ cm}^{-3}$) epi-ready GaSb (001) double side polished substrates. Indium and gallium growth rates were determined by monitoring intensity oscillations in the reflected high-energy electron diffraction (RHEED) patterns and were set to 0.5 ML/s for Ga (which corresponds to the beam equivalent pressure (BEP) of 1.46×10^{-7} Torr) and 0.45 ML/sec for In (which corresponds to the BEP of 2.5×10^{-7} Torr). Group-V fluxes were adjusted using a conventional ion gauge to satisfy group V/III BEP flux ratio equal to 7.5 for GaSb and 3.8 for InAs. All the growths were performed on cleaved $10 \times 10 \text{ mm}^2$ pieces of GaSb:Te substrate. The substrates were initially outgassed in vacuum, and the surface oxide was then removed at high (535°C) temperature under Sb flux. The temperature of (1×3) to (2×5) reconstruction transition (T_t) on GaSb surface observed on the RHEED pattern was taken as a reference for

all the growth temperatures (figure 3.10). This transition temperature is the same for all the GaSb substrates under given Sb flux [31].

Prior to the interface study, two samples with 8MLs InAs/ 8MLs GaSb and 8MLs InAs/ 24 MLs GaSb and the same thickness ($0.144 \mu\text{m}$) were grown on GaSb substrates to verify the growth rates. From the spacing between the satellite fringes in symmetric (004) X-ray scans, the exact growth rates of the InAs and GaSb layers were determined [27].

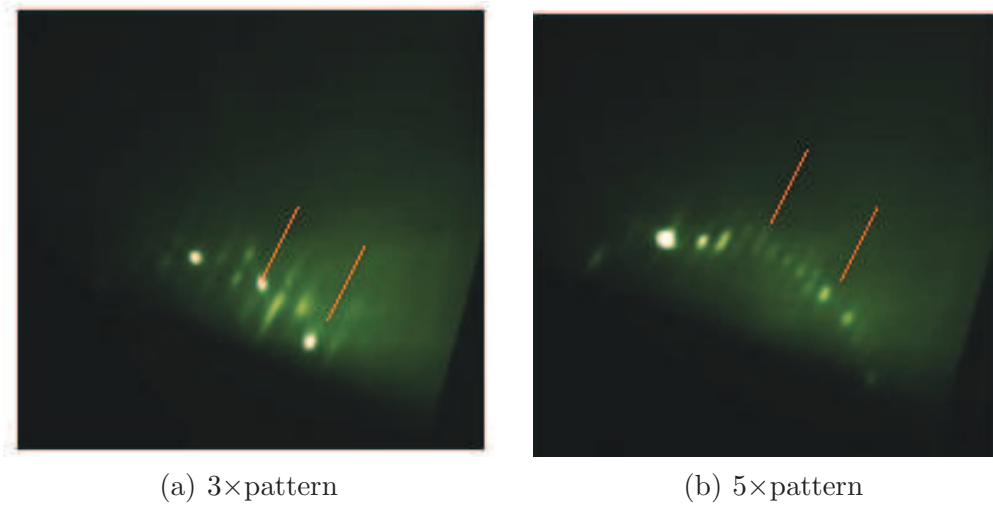


Figure 3.10: The temperature of (1×3) to (2×5) reconstruction transition was taken as a reference for the growth temperatures.

Epitaxial growth of strain-balanced SL

For the purpose of strain optimization in LWIR SL structure, two sets of samples with 60 periods of SL with the same composition (13 MLs InAs/ 7 MLs GaSb) and different methods of InSb interface formation were investigated.

Set A includes four SL samples with variable thickness (0, 0.45, 0.9 and 1.35 ML) of InSb layer inserted between InAs and GaSb layers. Set B includes three SL

samples grown with "InSb-like" interfaces formed by Sb-to-As exchange on GaSb-on-InAs interface through the inclusion of variable Sb soak times (16, 18 and 20 sec) in the shutter sequence [32]. Since it was recently shown [28] that combination of Sb and As soak times during SL growth provides additional flexibility in control of average strain in the structure, we included a fixed As soak time (2 sec) in the shutter sequence during the growth of set B. It should be noted that both sets of the samples studied here were grown at 45 degrees below the T_t .

The bandgap of all of the samples was determined through room temperature absorption measurements, which were performed using a Nicolet-870 Nexus Fourier transform infrared (FTIR) spectrometer and the reflectivity module associated with it. The reflectance of sample was calculated as ratio of reflected signals measured from sample and reference substrate (n-type GaSb). In order to eliminate the transmission component from the consideration, a thin layer of gold (50 nm) was deposited on the backside of both the sample and the reference substrate. Thus, the absorbance, A , as a function of wavelength is calculated using $A = (1 - R)$ relation, where R is the measured two pass reflectance of the sample. No significant changes in absorbance were observed with the variation of growth procedure of SL. The cut-off wavelength (defined as the wavelength where the response went to zero) was found to be $\sim 8\mu\text{m}$ (at 300K).

Full width at half maximum (FWHM) for the first-order peak of SL as well as lattice mismatch between zero-order peak of SL and GaSb substrate were calculated for both sets and are presented in figures 3.11(a) and (b). It should be noted that SL grown without any interfacial control has a FWHM of first order SL peak equal to 343 arcsecs and lattice mismatch between zero-order peak of SL and GaSb-substrate of + 0.09% (tensile strain). This implies poor crystalline quality and fluctuations in the thickness of the period due to, probably, anion exchange on SL interfaces during the SL growth.

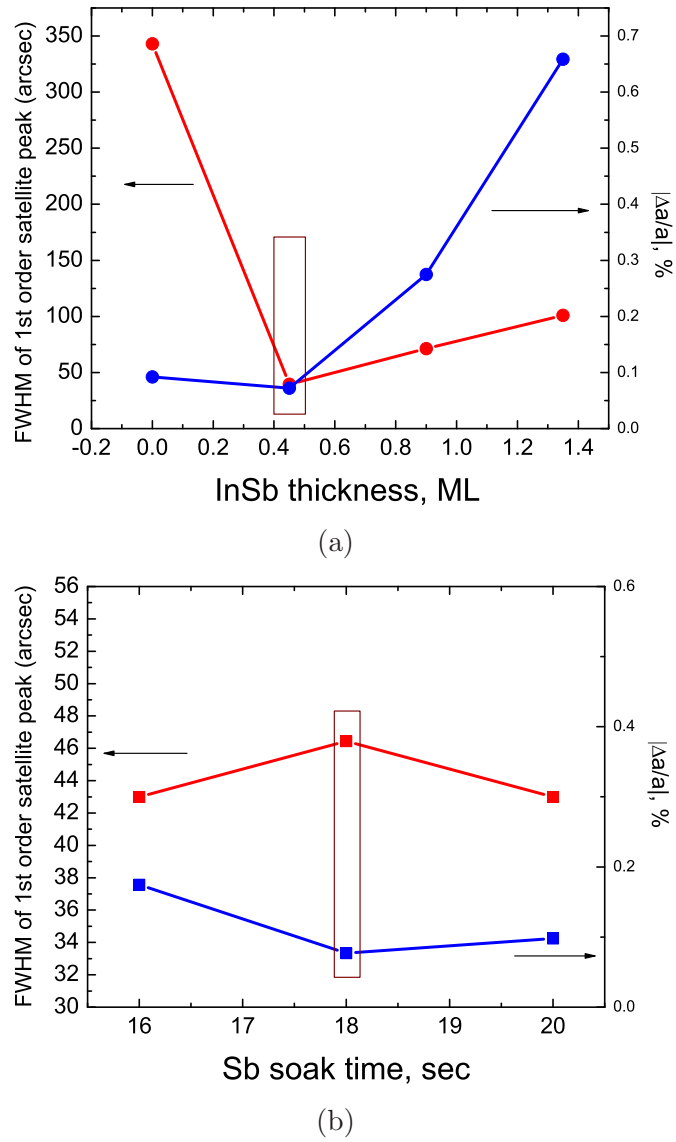


Figure 3.11: Growth optimization for LWIR structure using (a) InSb layer (b) group V soak time.

In set A, with presence of 0.45 ML thick InSb layer in each SL period, the lattice mismatch and FWHM of first order SL peak improves, reaching - 0.07% and 40 arcseconds, respectively. However, with further increase in InSb layer thickness, structural quality of SL degrades (Figure 3.11(a)). We attribute this degradation to

the possible change in growth mode from layer-by-layer (InSb thickness of 0.45 ML) to the 3D island formation (InSb thickness exceeds 0.45 ML). In set B, the thickness of "InSb-like" interfaces is formed by controlling the duration of Sb soak-time. Based on the MWIR InAs/GaSb SL optimization [28] and due to 13 MLs thickness of InAs layer in the LWIR SL, we used 18 seconds of Sb soak time which was used as a base line for the study. Figure 3.11(b) indicates that the FWHM of first order SL peak and lattice mismatch of SL to the substrate does not change significantly with increase in the Sb soak time. This can be explained by the fact that Sb-for-As exchange on the InAs surface during Sb-soak is thermodynamically less favorable than the As for Sb exchange. It is evident, that both the above mentioned approaches did not lead to totally "strain-balanced" SL material. However, the SL grown with the 0.45 ML InSb layer inserted in every period of SL possesses the lowest value of lattice mismatch to the substrate (- 0.07%) and FWHM of the first order SL satellite peak (40 arcsec). Therefore, this growth procedure is undertaken for the further studies.

Optimum growth temperature

Using the optimum thickness of InSb (0.45 ML) as strain compensation layer, we grew another set of samples to study the optimum growth temperature. The temperature dependent surface diffusion of the ad-atoms affects the structural and optical properties of the SL. It is necessary to have a substrate temperature high enough to avoid excessive element V deposition, but low enough to limit the atom exchanges at the different interfaces.

This set (C) includes three samples with 60 periods of 13 ML InAs/ 0.45 ML InSb/ 7 ML GaSb SL structure grown at 25, 45 and 65 degrees below T_t . FWHM of first order SL peak as well as lattice mismatch of zero-order peak of SL and GaSb-substrate were calculated for this set and are presented in figure 3.12. The data indicates a clear minimum at 45 below the T_t , with 40 arcsec FWHM and -

0.07% (compressive strain) lattice mismatch. The - 0.07% compressive strain can be further compensated by combination of "GaAs-like" (formed by As-to-Sb exchange on InAs-on-GaSb interface) and InSb interfaces.

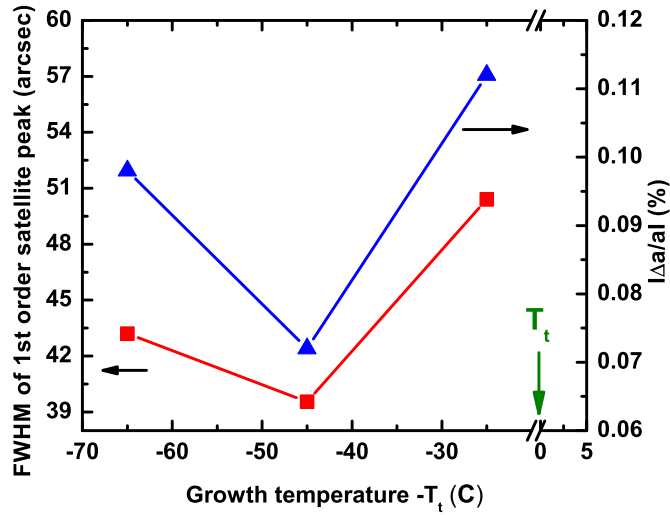


Figure 3.12: Growth temperature optimization for LWIR structure

To complete the structural investigations on the three sets of samples, the surface morphology and roughness was assessed by AFM on a $5 \times 5 \mu\text{m}^2$ scan area. For the set A, 0.9 ML of InSb showed the lowest averaged roughness with a value equal to 0.15 nm. For the sets B and C the lowest averaged roughness was equal to 0.15 nm for Sb soak-time of 18 sec, and 0.13 nm for the SL grown at $(T_t - 65^\circ)$, respectively.

nBn based detector structure grown with optimized SL

After verifying the structural and optical properties of the superlattice, an n-B-n infrared photodetector was grown. More detailed description of nBn detector will be provided in the next section In order to compensate for the residual compressive strain, a combination of "GaAs-like" interface (formed by using one second of As soak time) and InSb interface was used. The absorption region of detector consisted

of 625 periods of [1sec As-soak time/13 ML InAs/0.45 ML InSb/ 7 ML GaSb] SL with total thickness of $\sim 2\mu\text{m}$. The top and bottom contact layers were formed by the same SL with Si-doped ($n = 4 \times 10^{18} \text{cm}^{-3}$) InAs layers and thickness of $0.13 \mu\text{m}$ and $0.47 \mu\text{m}$, respectively. The HRXRD along with the heterostructure schematic of the detector is shown in figures 3.13(a) and (b). The HRXRD exhibits intense satellite peaks with a FWHM of the first-order peak equal to 16 arcsec and lattice mismatch of 0%, attesting the good crystalline quality of the layers and high reproducibility rate in the SL period.

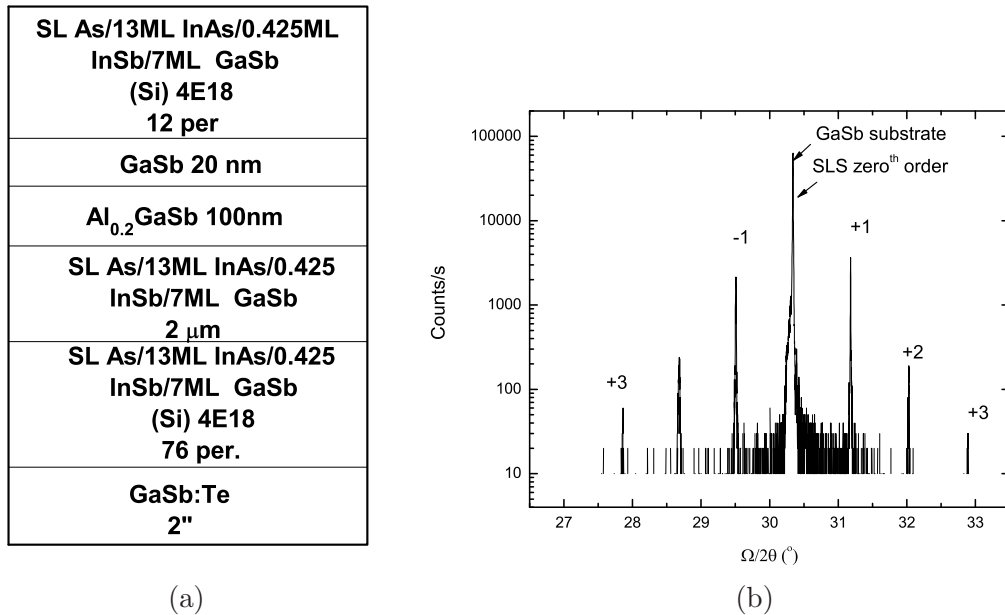


Figure 3.13: LWIR nBn structure (b) XRD of LWIR nBn structure, almost zero % lattice mismatch between SL and GaSb substrate and 19 arcsec FWHM for the first satellite peak.

Finally, the quality of interfaces in the detector structure is studied by cross-sectional STEM. Transmitted electron images were acquired at various magnifications in atomic number contrast mode (ZC) using a High-Angle Annular Dark-Field (HAADF) detector. The dark field imaging allows the chemical identification of the respective epilayers displaying periodic InAs/InSb/GaSb layers over the total SL

structure as shown in figure 3.14.

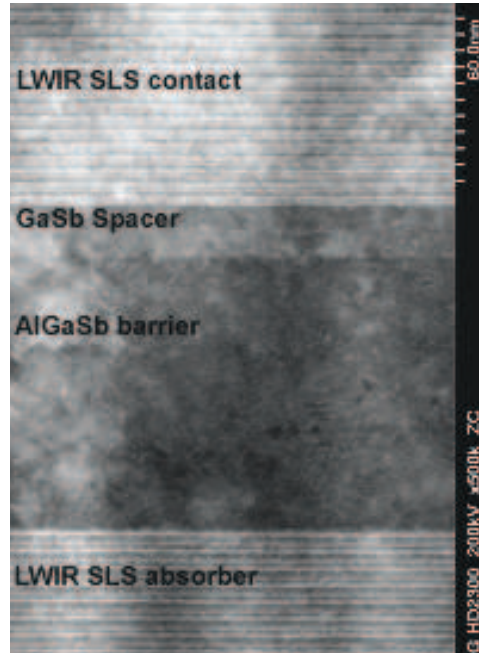


Figure 3.14: Cross-sectional STEM images of an nBn detector

3.5 Longwave pin detectors

For the design of narrow gap devices, the doping level is a critical parameter in determining the electrical and optical qualities of the device. The dark current mechanisms for the net transport of electrons and holes across the depletion region can be classified into two categories, fundamental mechanisms, which depend only on the material properties and device design, and defect-related mechanisms, which require a defect as an intermediate state. Band-to-band tunneling occurs in the depletion region of the p-n junction, together with the diffusion process in the neutral region and the generation-recombination (G-R) process in the depletion region.

In this section a series of long wavelength InAs/GaSb pin diodes grown on n-type GaSb substrates has been analyzed using current-voltage (I-V) and responsivity measurements. The series contains of one non-intentionally doped pin diode, along with two p-doped absorbing region pin diodes. Non-intentionally doped LWIR SL system is a residually n-type system due to thicker layers of residually n-type InAs layers as compared to the residually p-type GaSb layers. The dopant material and its concentration is an important parameter in long-wave (LW) InAs/GaSb type-II SL design and growth, that can affect the optical and electrical properties of SLs structures. Beryllium (Be) doping the InAs layers is an effective method in decreasing the dark current by lowering the diffusion, generation-recombination and tunneling currents and increase the quantum efficiency of the device by switching to high mobility minority electron concentration [33]. In this section, investigation of LWIR pin detector and the influence of absorber p-doping on the optical and electrical properties of the devices is presented.

3.5.1 LWIR InAs/GaSb pin diodes growth and processing

To study the influence of p-doping of the absorbing region of pin SL detectors on the device performance, a set of three pin detectors were grown. To enable device comparisons, all three samples had exact same thicknesses for the absorbing region. Devices were grown on Te-doped epi-ready (100) GaSb substrates using a solid source molecular beam epitaxy VG-80 system. The system was equipped with SUMO cells for gallium and indium, a standard effusion cell for aluminum and cracker cells for antimony and arsenic.

The designs consisted of a 473 nm thick bottom contact layer formed by 13 MLs InAs:Si ($n = 4 \times 10^{18} \text{cm}^{-3}$) / 0.75 ML InSb / 7 MLs GaSb SL followed by 250 nm thick doping graded layers of 13 MLs InAs:Si / 0.75 ML InSb / 7 MLs GaSb SL to

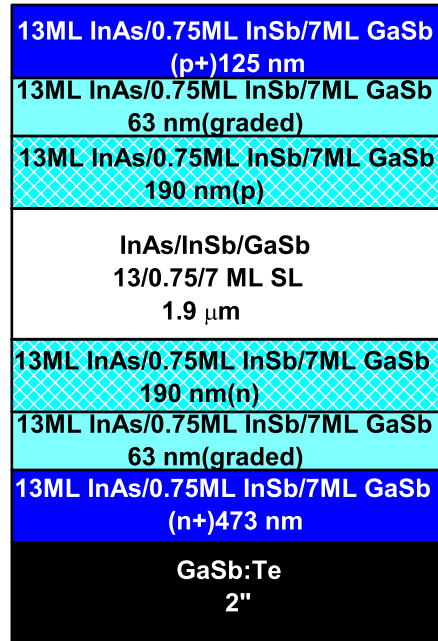
achieve doping concentration of $n = 1 \times 10^{17} \text{cm}^{-3}$ before the absorbing layer. Then a $1.9 \mu\text{m}$ thick absorber formed by 13 MLs InAs/ 0.75 ML InSb/ 7 MLs GaSb SL was grown followed by 250 nm thick p-doping graded layers. The structure was terminated by a 125 nm thick p-type ($p = 4 \times 10^{18} \text{cm}^{-3}$) top contact layer with the same composition as the bottom contact layer. The absorber region doping level was varied during the growth of the three pin detectors. The first sample, absorbing region was non-intentionally doped. In second and third samples the doping of the absorbing regions were $\text{Be}: 5 \times 10^{15} \text{cm}^{-3}$ and $\text{Be}: 1 \times 10^{16} \text{cm}^{-3}$, respectively. The heterostructure schematic along with the HRXRD of the non-intentionally doped pin are presented in figures 3.15(a) and (b), respectively. The HRXRD exhibits intense satellite peaks with a full-width at half maximum (FWHM) of the first-order peak equal to 46.8 arcsec and a lattice mismatch of $\sim 0\%$, attesting to the good crystalline quality of the layers and the high reproducibility rate in the SL period. The devices were processed using the same procedure described in section 3.3.2.

3.5.2 Characterization of LWIR InAs/GaSb pin diodes

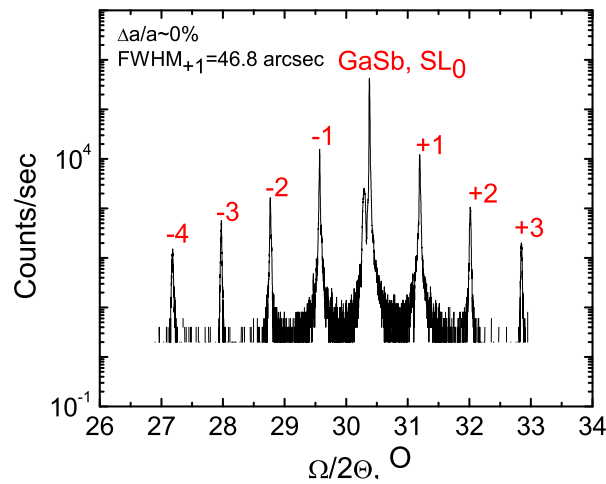
Figure 3.16 presents the dark current density of pin structures at 77 K.

The data shows that the dark current density of the pin detectors decreases with p-doping the InAs layers in the absorbing region. The lowest dark current density is associated with the sample which the Be doping concentration in InAs layers is $5 \times 10^{15} \text{cm}^{-3}$. In this comparison we neglect the effect of surface leakage currents since all three pin samples were identically processed and passivated. The main dark current components in these detectors are diffusion, generation-recombination and tunneling current.

$$\frac{1}{R_0 A} = \frac{1}{(R_0 A)_{diff}} + \frac{1}{(R_0 A)_{G-R}} + \frac{1}{(R_0 A)_{tunn}} \quad (3.4)$$



(a)



(b)

Figure 3.15: (a) Schematic of LWIR SL pin detectors; represents three samples with different absorber region doping levels (b) HRXRD of the non-intentionally doped LWIR SL pin detector.

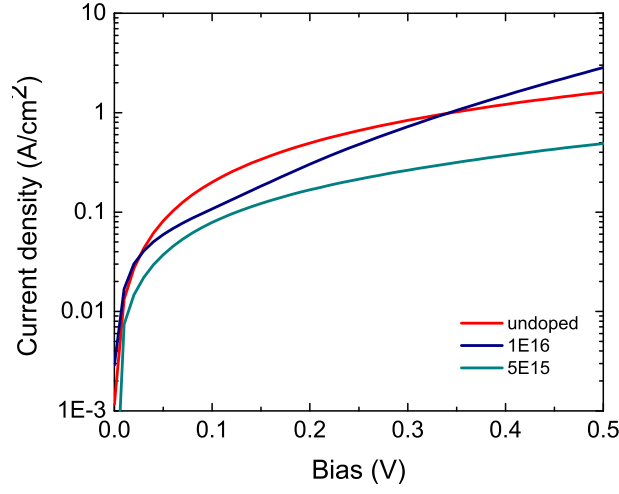


Figure 3.16: Dark current density at 77 K for the three pin structures.

Where R_0A is the dynamic resistance at zero bias, and the thermal diffusion resistance, $(R_0A)_{diff}$, is expressed as following:

$$(R_0A)_{diff} = \frac{(KT)^{1/2}}{q^{3/2}} \frac{1}{n_i^2} \left[\frac{1}{N_A} \left(\frac{\mu_e}{\tau_e} \right)^{1/2} \tanh\left(\frac{d_p}{L_e}\right) + \frac{1}{N_D} \left(\frac{\mu_h}{\tau_h} \right)^{1/2} \tanh\left(\frac{d_n}{L_h}\right) \right]^{-1} \quad (3.5)$$

Where n_i is the intrinsic carrier density, k is the Boltzman constant, $\tau_{e,h}$ is the electron (hole) lifetime, q is the electric charge, $N_{A,D}$ is the acceptor (donor) concentration, and T is the temperature, $d_{P,N}$ is the region thickness of the carrier, and $L_{e,h}$ is the diffusion length of the electrons and holes. So as the doping level increases, R_0A increases which lowers the dark current associated with diffusion mechanism. So, the thermal diffusion current is associated with the minority carriers within a diffusion length of the depletion region. As the doping level increases, the minority carrier concentration decreases, therefore the diffusion current decreases.

R_0A associated with Generation-Recombination mechanism is described as following:

$$(R_0A)_{G-R} = \frac{2V_{Bi}}{qn_iW} (\tau_{G-R}) \quad (3.6)$$

Where τ_{G-R} is the effective G-R lifetime and W is the depletion region with at zero bias voltage. As the doping is increased, depletion width decreases, and therefore, dark current associated with G-R is suppressed.

R_0A associated with band to band tunneling is described as following [33]:

$$(R_0A)_{tunn} = \frac{4\pi^2\hbar^2}{q^3E} \left(\frac{E_{g,100\%}}{2m^*}\right)^{1/2} \exp\left(\frac{4E_{g,100\%}}{3q\hbar} \sqrt{\epsilon_s m^* N_{red}^{-1}}\right) \quad (3.7)$$

Where E is the electric field, ϵ_s is the static dielectric constant of the SLs, m^* is the electron effective mass, $E_{g, 100\%}$ is the cutoff of the photodiode at 77 K and N_{red} is the reduced carrier concentration and is, $N_{red} = [1/N_A + 1/N_D]^{-1}$. From the above expression, as the carrier concentration increases, the band to band tunneling increases as well.

As the doping in a pn junction increases, the depletion region width decreases which results in an increase in tunneling of the majority carriers across the depletion region. Moreover, the decrease in depletion width causes an increase in electric field across the space charge region that increases the tunneling probability furthermore.

Therefore, by increasing the doping level, diffusion current decreases. The G-R current also decreases due to decrease in depletion width. Tunneling current decreases up to a certain doping concentration ($5 \times 10^{15} \text{ cm}^{-3}$ Be doped) but as the doping concentration increases more, the maximum electric field across the depletion region increases which causes the tunneling probability to increase. This can explain the larger dark current for the $1 \times 10^{16} \text{ cm}^{-3}$ Be doped sample compared to the n.i.d sample at bias points larger than 0.35 V.

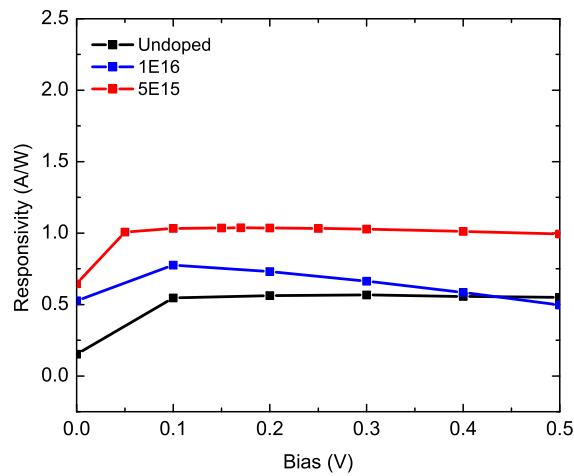
Responsivity and D^* were measured at 77 K using a pourfill dewar and a Micron M365 calibrated 800 K blackbody source. No anti-reflection coating was applied on the devices. As is shown in figure 3.17(a), the responsivity of pin detectors increases with $5 \times 10^{15} \text{ cm}^{-3}$ Be doping of the photodiode absorbing region. Further increase

in the doping concentration ($1 \times 10^{16} \text{cm}^{-3}$) leads to a drop in responsivity of pin photodiodes. To understand this behavior qualitatively, it's worth noticing that the responsivity of a photodetector is the number of collected carriers per incident photon. Therefore, it is proportional to the ratio of photo-carriers leaving the absorbing region and photo-carriers recombining within the absorbing region. When the absorption region is Be doped, the minority carriers switch to high mobility electrons as compared to the non-intentionally doped sample where the minority carriers are holes. The rate that carriers leave the absorbing region is faster in Be doped samples as compared to n.i.d sample. Therefore, the probability of carrier recombination decreases and leads to higher responsivity. However, at higher Be doping concentrations ($1 \times 10^{16} \text{cm}^{-3}$), mobility of minority carriers decreases due to the increase in scattering from the dopants.

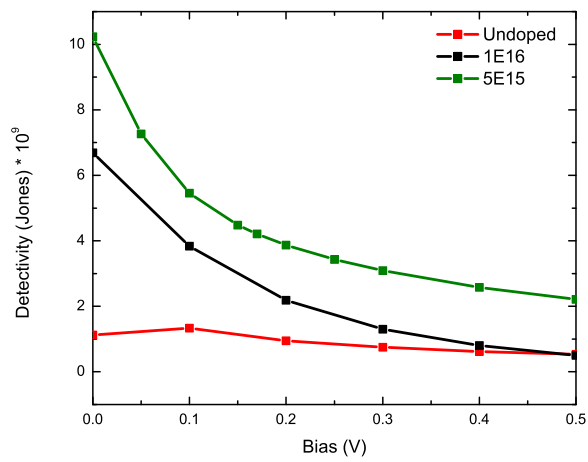
The shot-noise limited spectral detectivity (D^*) of the device was estimated using:

$$D^* = \frac{R}{\sqrt{2qJ + (4kT)/(R_d A_d)}} \quad (3.8)$$

Where R is the responsivity, q is the electronic charge, T is the temperature of the device, k is Boltzmann's constant, J is the current density, R_d is the dynamic resistance, and A_d is the diode area. Detectivity measurements for pin devices is shown in figure 3.17(b). The behavior seen in figure 3.17(b) for detectivities of pin devices is well expected since it is a measure of signal (responsivity) to noise (dark current) ratio.



(a)



(b)

Figure 3.17: (a) Responsivity and (b) detectivity measurements of the pin devices at 77 K

3.6 Longwave nBn detectors

3.6.1 nBn detectors

As it was discussed in the introductory part, the SL technology has potential to enhance performance in key areas such as operating at higher temperature [34].

However, Most of the present day SL photodetectors are based on the pin photodiode design [13, 28]. In focal plane arrays based on pin diodes, pixels are separated from their neighbor pixels by an etched mesa. During the mesa isolation process, the periodic nature of the crystal structure ends abruptly at the mesa lateral surface. Disturbance of the periodic potential function due to a broken crystal lattice leads to allowed electronic quantum states within the energy band gap of SL resulting in large surface leakage currents. The suppression of these currents by using a stable passivation layer for the etched mesa surface for the SL photodiodes is one of the primary limitations of the SL based technology. A class of IR detectors named nBn has shown promising results in eliminating the currents associated with Shockley-Read-Hall centers and mesa lateral surface imperfections, which have resulted in an increase of the operating temperature [35] as compared to the pin design. This so-called nBn structure consists of a n-type narrow bandgap contact and absorber layers separated by a 50-100 *nm* thick wide bandgap barrier layer. A schematic of ideal nBn structure is shown in figure 3.18.

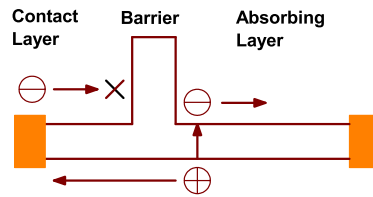


Figure 3.18: Schematic of nBn design. Majority carriers (electrons) are blocked by the barrier and minority carriers (holes) are the source of current.

Implementation of the nBn design for InAs/GaSb midwave infrared (MWIR) SL single element and FPAs have been reported [17, 36, 37], but to date, little work has been reported on the performance of LWIR nBn based devices [11].

Photoconductive gain in nBn detectors

In a photoconductor with ohmic contacts (injecting contacts), the photoconductor exhibits photoconductive gain, which is defined as the ratio of the number of electrons/holes collected in the external circuit to the number of absorbed photons. An absorbed photon photogenerates an electron hole pair, which drift in opposite directions. The electron drift velocity is larger than the hole drift velocity and hence reaches the opposite contact first. The sample however must be electrically neutral which means another electron must enter the sample from the negative electrode. This new electron also drifts across quickly to reach the contact while the hole is still drifting slowly across the sample. Thus another electron must enter the sample to maintain neutrality, and so on, until either the hole reaches the negative electrode or recombines with one of these electrons entering the sample. The external photocurrent therefore corresponds to the flow of many electrons per absorbed photon, which leads to a photoconductive gain. The gain is also defined as the ratio of the recombination lifetime to the transit time. For nBn detectors since no depletion region exists, therefore the behavior of these devices is closer to that of photoconductors than photodiodes. However, since for every photon absorbed, the electron is blocked by the barrier and cannot reach the contact, thus nBn devices do not have photoconductive gain. This has recently been shown by Klipstein [38].

3.6.2 Growth and processing of LWIR SL detector based on nBn design

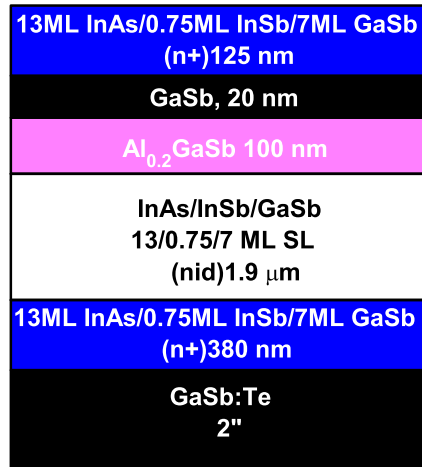
The detector consisted of a 380 nm bottom contact layer formed by 13 MLs InAs:Si ($n = 4 \times 10^{18} \text{cm}^{-3}$) / 0.75 ML InSb / 7 MLs GaSb SL. Then a 1.9 μm thick non-intentionally doped (n.i.d.) absorber region formed by 13 MLs InAs / 0.75 ML InSb / 7 MLs GaSb SL was grown followed by a 100 nm thick $\text{Al}_{0.2}\text{Ga}_{0.8}\text{Sb}$ barrier layer.

The $\text{Al}_{0.2}\text{Ga}_{0.8}\text{Sb}$ barrier layer was capped with a 20 nm thick GaSb spacer to avoid oxidation of the Al during the processing steps. The structure was terminated by a 125 nm thick n-type ($n = 4 \times 10^{18} \text{cm}^{-3}$) top contact layer with the same composition as the bottom contact layer. The heterostructure schematic along with the HRXRD of the detector is shown in figure 3.19 3.19(a) and 3.19(b), respectively.

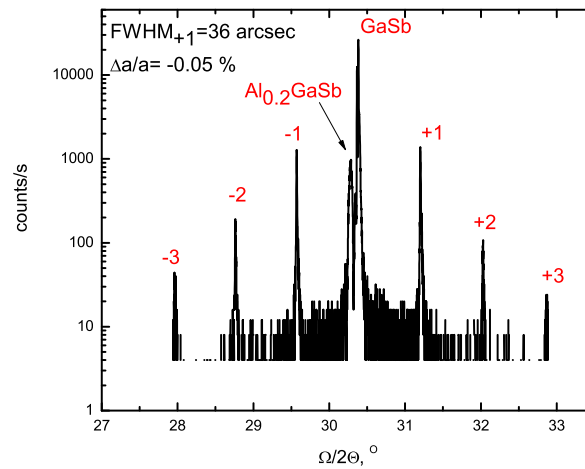
One of the advantages of the nBn structures is its unique processing technique which eliminates surface currents. Unlike p-i-n diodes where each pixel is defined with a deep etch (standard processing), in nBn processing (shallow etched devices), the diffusion length in the absorber is the parameter that isolates one device from the device next to it. This eliminates the presence of surface leakage currents. In order to show the reduction of surface leakage currents in shallow etching as compared to the deep etched processing, both methods were implemented on the LWIR nBn structure. Specific processing used for the nBn structures is as follows.

The material was processed into normal incidence single pixel photodiodes with apertures ranging from 25-300 μm in diameter using standard optical photolithography technique. Processing was initiated with the formation of ohmic contacts to the n-type top contact layer followed by etching of this contact layer to the top of the barrier ($\sim 125 \text{ nm}$) for the mesa definition. Using this approach, the active layer was encapsulated by the barrier and there was no need for development of an additional passivation coating. We used inductively coupled plasma (ICP) etching for this purpose. Then part of the wafer was masked with the photoresist and the ICP deep dry etching to the middle of the bottom n-type contact layer was performed on the other part. An ohmic contact was evaporate. An ohmic contact was evaporated on the bottom contact layer. We used a Ti (50 nm)/Pt (50 nm) /Au (300 nm) as n-contact metal for both top and bottom contacts.

Figure 3.20 shows the main processing steps which are used for nBn devices to make both shallow and deep devices.



(a)



(b)

Figure 3.19: (a) Structure schematic (b) HRXRD of the LWIR nBn detector.

Figures 3.21(a) and (b) present schematic of a completed shallow etched, and deep etched devices, respectively.

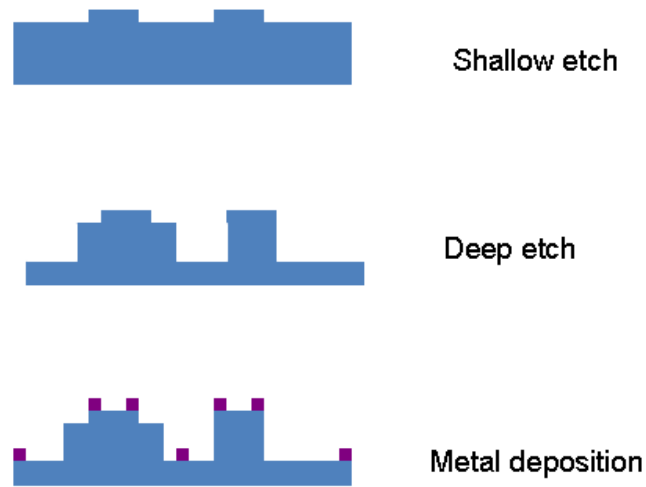


Figure 3.20: Main processing steps for LWIR nBn detectors

3.6.3 Characterization of the LWIR SL detector based on nBn design

Figure 3.22 shows the dark current density for shallow etched and deep etched processed nBn devices. A reduction of the dark current density in shallow etched device can be seen at in comparison with the deep etched device. This is attributed to the reduction of leakage surface currents.

Responsivity and detectivity of LWIR SL detectors based on nBn design is measured in the same as the LWIR SL pin detectors discussed in the previous chapter. Figure 3.23(a) and (b) shows the responsivity and detectivity of the shallow etched nBn device.

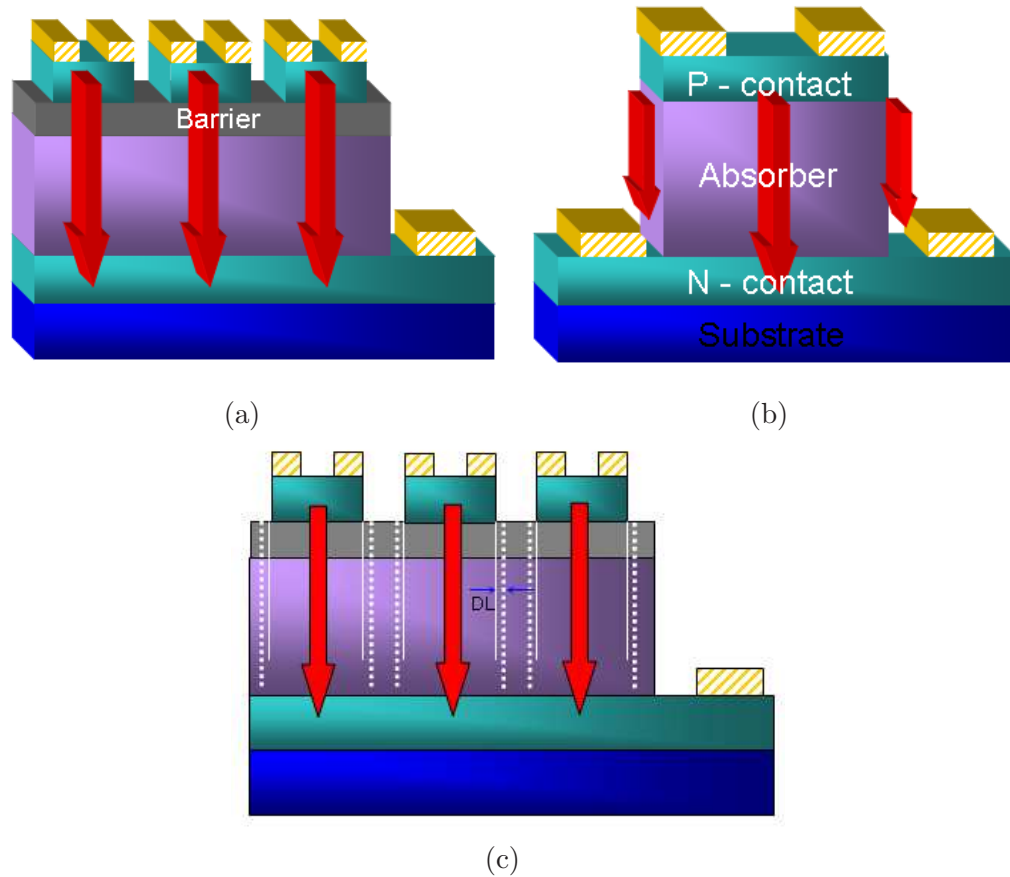


Figure 3.21: (a) Shallow etch processing (b) deep etch processing (c) shallow etch processing with indication of diffusion lengths.

3.7 Comparison of the LWIR pin and nBn detectors

In this section device characteristics comparison between the LWIR pin devices presented in section 3.5 and the shallow etched nBn device presented in section is presented.

- Processing:

Processing of both types of the devices is discussed in the earlier sections.

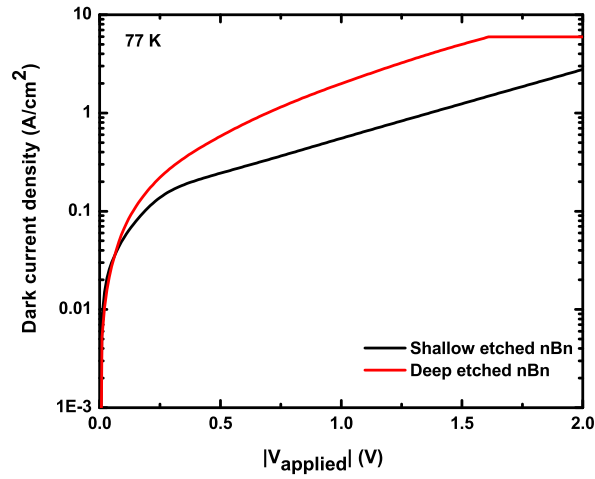


Figure 3.22: Dark current density of shallow, and deep etched nBn devices vs temperature. This comparison shows the effect of dark current density reduction due to reduction of surface leakage currents.

The only difference is that in pin devices one device is separated from the neighboring device by the mesa etching which creates side walls exposing to the atmosphere and results in presence of surface leakage current as a dark current mechanism in the device. However, in nBn designs one device is defined from the neighboring device by the diffusion length of the minority carriers. Therefore, it allows for a shallow etch process that helps to reduce the surface leakage currents.

- Spectral response:

The relative spectral responses of pin and nBn structures as a function of wavelength are shown in figures 3.24(a) and (b), respectively. The data clearly shows cutoff wavelength of $\lambda_c \approx 8 \mu\text{m}$ for both pin and nBn designs. The only difference is that forward bias in nBn design is defined where negative bias is applied on the top of device and reverse bias in pin design is defined where negative bias is applied on the top of device.

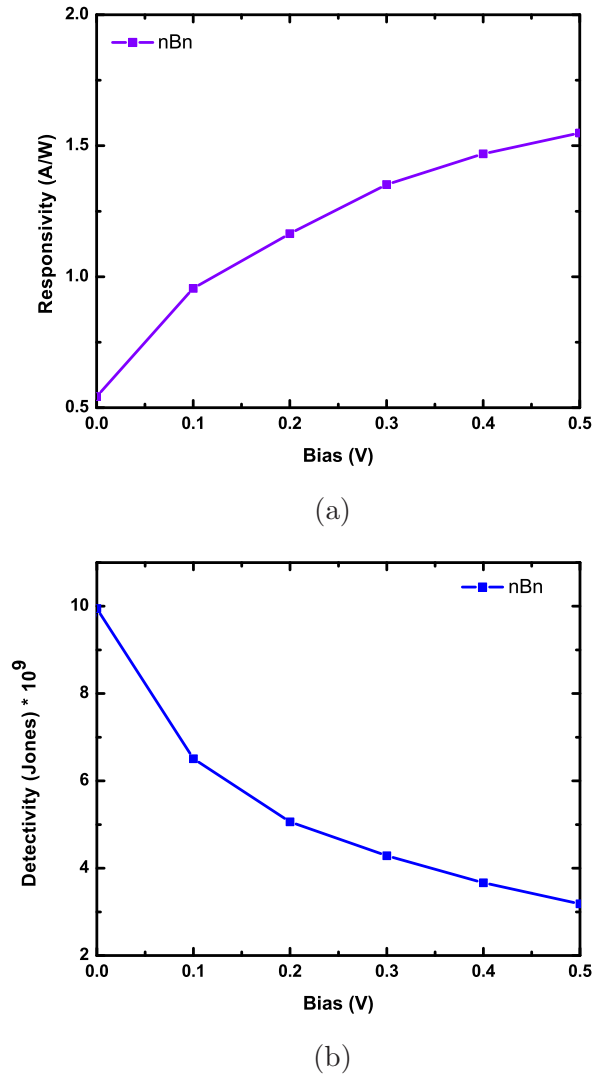
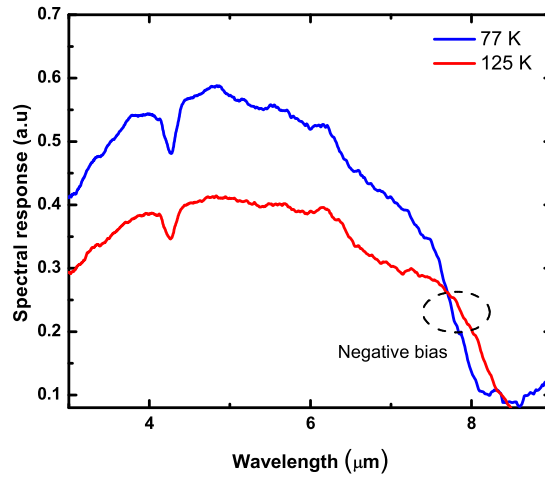


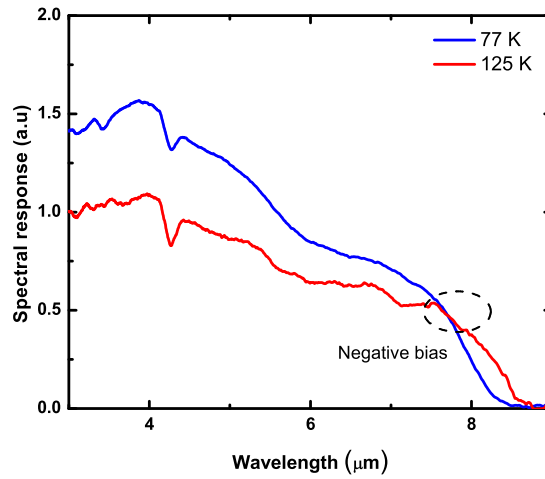
Figure 3.23: (a) Responsivity and (b) detectivity measurements of the nBn device at 77 K

- Dark current density:

Figure 3.25 presents the dark current density of the optimized pin detector with absorbing doping of $\text{Be}:5 \times 10^{15} \text{cm}^{-3}$ as compared to the shallow etched nBn device. Dark current density in $(5 \times 10^{15} \text{cm}^{-3} \text{ Be doped})$ pin structure is $(0.08 \text{ A/cm}^2 \text{ at } -100 \text{ mV})$ as compared to the nBn based design $(0.05 \text{ A/cm}^2 \text{ at } -100 \text{ mV})$



(a)



(b)

Figure 3.24: Spectral response of (a) pin (b) nBn structure, $8 \mu\text{m}$ cutoff wavelength is shown in the two diagrams.

+100 mV). It is worth mentioning that the dark current density measurements of the nBn design were measured with a 300 K background while the pin dark current density measurements are performed with a cold shield which can further decrease the dark current density associated with nBn devices. This lower dark current density in nBn design is due to a reduction of the

currents associated with Shockley-Read-Hall centers and mesa lateral surface imperfections in nBn design. However, nBn structure, could also have lateral diffusion of minority carriers (holes), which is ignored in this analysis [39].

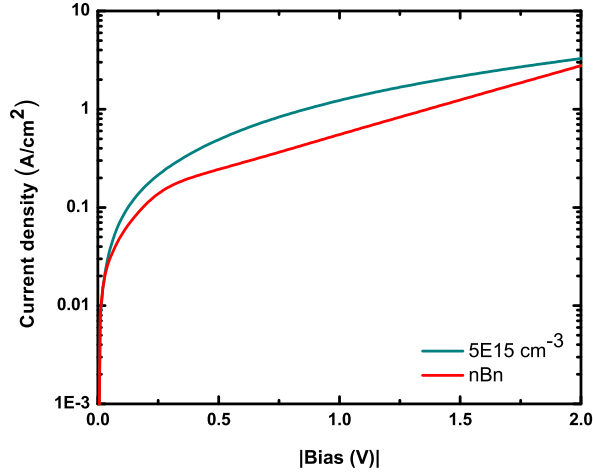


Figure 3.25: Dark current density at 77 K for nBn and pin structures

- Responsivity:

Figure 3.26(a) and (b) present the responsivity and detectivity of the optimized pin detector with absorbing region doping of $\text{Be}:5 \times 10^{15} \text{cm}^{-3}$ as compared to the shallow etched nBn device, respectively.

Figure 3.26(a), shows that nBn device has a higher responsivity as compared to the pin devices. Photodiodes based on nBn design eliminate SRH recombination centers associated with depletion regions which are the main source of recombination mechanisms in pin photodiodes, and therefore, more carriers are extracted from the absorbing region which increases the responsivity of these devices. It is worth mentioning that the responsivity of nBn devices can be improved further with optimizing the barrier band offsets and thickness of these structures.

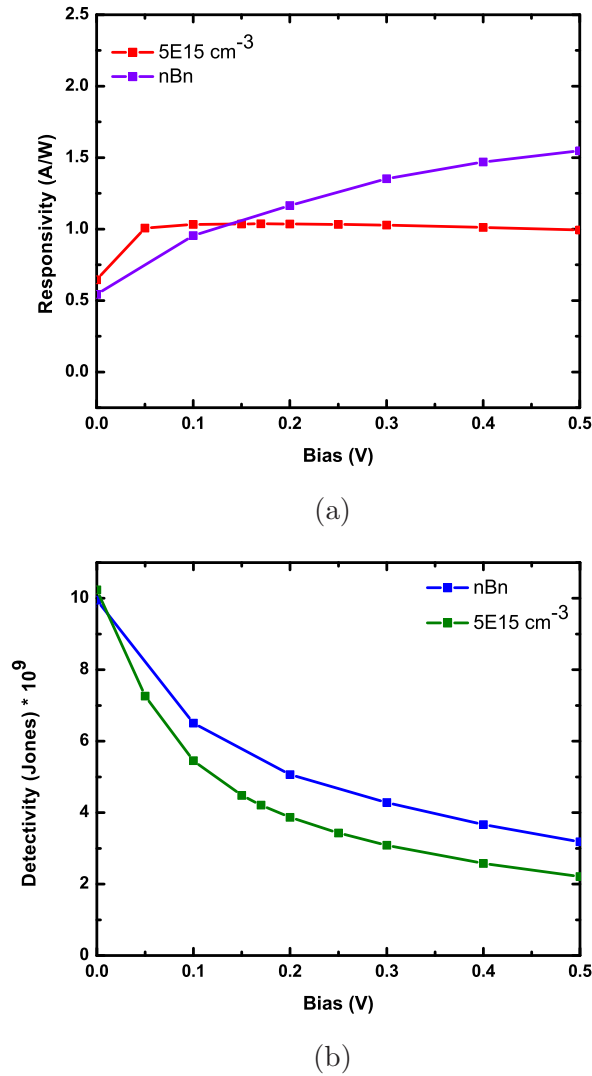


Figure 3.26: (a) Responsivity and (b) detectivity measurements of the pin and nBn devices at 77 K; nBn structure has the highest responsivity and detectivity values as compared to the pin structure.

Figure 3.26(b) shows that the nBn device has the higher detectivity as compared to the pin device which is well expected since it is a measure of signal (responsivity) to noise (dark current) ratio. Table I, shows summarized values of dark current, responsivity and detectivity of pin and nBn devices.

Table 3.1: Summary of dark current density, responsivity and detectivity of pin and nBn devices measured at 77 K, 7 μm .

Sample	Dark Current Density (A/cm ²) 0.1 V	Responsivity (A/W) 0.2 V	Detectivity (cm Hz ^{1/2} W ⁻¹) 0.1 V
pin (n.i.d)	0.2	0.62	1.3×10 ⁹
pin (1×10 ¹⁶ cm ⁻³)	0.11	0.8	4.2×10 ⁹
pin (5×10 ¹⁵ cm ⁻³)	0.08	1.03	6.1×10 ⁹
nBn	0.05	1.28	7.2×10 ⁹

3.8 Conclusion

In this chapter, we discussed high performance mid-infrared pin InAs/GaSb SL detector ($\lambda_{cut-off}$ was $\lambda \sim 4.5 \mu\text{m}$ at 77 K) grown by molecular beam epitaxy. The structural, optical and electrical properties were characterized using X-ray crystallography, IV and responsivity measurements. At $V_b = -0.3 \text{ V}$, the total dark current was equal to 1.34×10^{-6} at 77 K which is comparable to the lowest published dark current densities reported by other groups. Design and growth of long-infrared SLs showed that highest structural properties were achieved by the insertion of InSb layer as a strain compensating layer between the InAs and GaSb layers. Devices based on nBn design have lower dark current density as compared to the conventional pin designs due to suppression of the currents associated with SRH centers and mesa lateral surface imperfections. Temperature dependent I-V measurements showed 0.05 A/cm² dark current density at +0.1 V for an nBn device as compared to 0.2 A/cm² at -0.1 V at 77 K for a pin device. Also nBn devices showed higher responsivity as compared to the pin devices due to elimination of SRH recombination centers associated with depletion regions. Therefore, more carriers are extracted from the

Chapter 3. Mid-wave and Long-wave pin and nBn SL detectors

absorbing region which increases the responsivity of the nBn devices. It is worth mentioning that optical and electrical performance of both pin and nBn devices can be improved by detailed passivation study for pin and optimized barrier and absorber doping level as well as barrier material and composition for nBn devices.

Chapter 4

Dual Band nBn InAs/Ga(In)Sb SL detectors

4.1 Introduction

In this chapter, for the first time the multi-spectral properties of infrared photodetectors based on type II InAs/Ga(In)Sb using an nBn heterostructure design are shown. The optical and electrical properties of the MWIR and LWIR absorbing layers are characterized using spectral response and current-voltage measurements, respectively. Present day two color SL detector require two contacts per pixel leading to a complicated processing scheme and expensive specific ROICs. For the first time, the dual-band response is achieved by changing the polarity of applied bias using single contact processing. The spectral response shows a significant change in the LWIR to MWIR ratio within a very small bias range (~ 100 mV) making it compatible with commercially available read out integrated circuits (ROICs).

4.2 Background and applications of Bi-color infrared detectors

Multicolor detectors are desirable in a variety of IR applications related to remote sensing and object identification. Today's state-of-the-art multispectral imagers use special optical and mechanical components like, e.g., filter wheels, beamsplitters and lenses in order to spectrally separate and focus the radiation onto one or more monospectral IR FPAs or even separate cameras [40]. These systems, due to their technical complexity, are difficult to manufacture (and thus expensive) and difficult to handle. Moreover, the images generated by these systems have an inherent temporal and spatial registration problem. These problems and limitations can be overcome by real multispectral FPA which have been under development during the last few years.

The first approach to build multispectral imagers are FPAs operating at two different spectral ranges, either in two separate atmospheric windows ("dual-band") or within one atmospheric window ("dual-color"). Dual-band detectors simply offer the advantage that the pros of both infrared bands can be combined in one imager. For example, MWIR imagers exhibit smaller blur spot for longer ranges and better performance in hot humid areas, whereas LWIR imagers deliver better performance in case of stray light or when the object under investigation is close to hot sources. A dual-band imager can be used in a wider range of ambient conditions. Moreover, dual-band detection permits the spectral discrimination of unique object features and thus a better distinction between targets and background clutter due to specific emissivity features.

Dual band, MWIR and LWIR, detectors have also interesting applications such as computed-tomography imaging spectrometer (CTIS) [41].

Chapter 4. Dual Band nBn InAs/Ga(In)Sb SL detectors

Figure 4.1 shows images taken by a dual-band detector and its application is locating the fire spots in South America [42]. Both the 4 and 11 micron figures (figures 4.1(a), 4.1(b)), respectively show the contrast between the cooler tropical forest in the west and the warmer grassland in the east. The 4 micron panel also shows a number of hotter regions corresponding to fires along the forest/grassland boundary and along a road in the west. The 4-11 micron panel (figure 4.1(c)) shows the differences between the 3.9 and 10.7 micron bands. The differences become larger when part of the pixel contains fire activity. The 3.9 micron band is much more sensitive to sub-pixel hot spots.

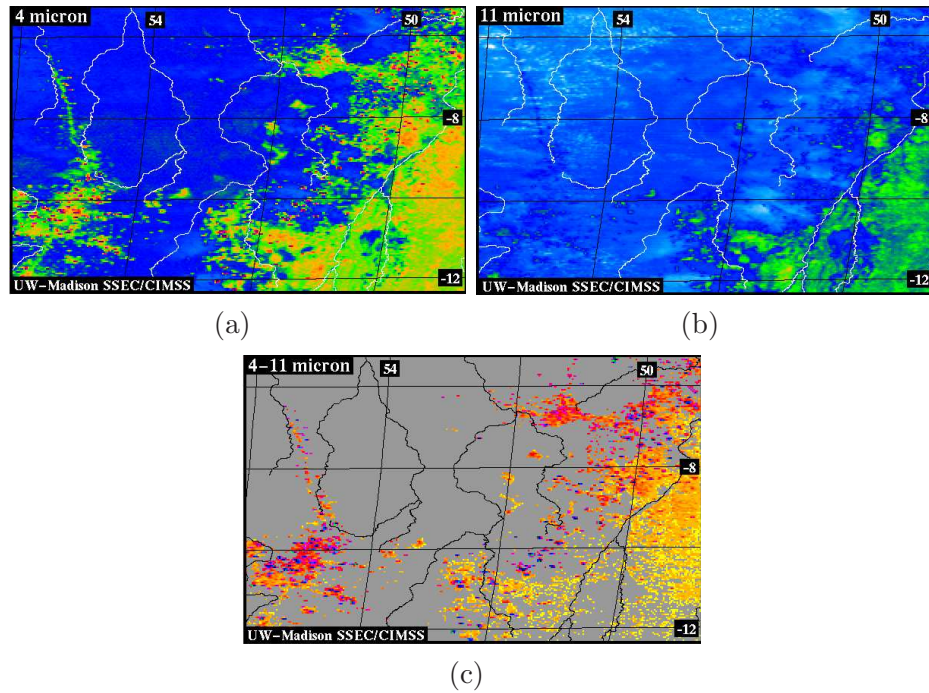


Figure 4.1: (a) mid-wave infrared image (b) long-wave infrared image (c) long-wave subtracted from midwave images taken to locate fire spots from South America lands.

4.3 Present bicolor detectors

Multicolor capabilities have been demonstrated with MCT and QWIP and more recently in the SL system [43]. Present day two color SL detector require two contacts per pixel leading to a complicated processing scheme and expensive specific ROICs. Below are two examples of common bi-color infrared detectors.

- Illustrated in figure 4.2(a) shows a crosssection schematic of a 30- μm unit-cell, single-mesa, single-contact dual-color detector, in addition to the typical current-voltage (I-V) characteristic for this detector design, figure 4.2(b). The two-color MCT architecture [44] leaves the p^+ layer floating, and the polarity of the voltage bias at the single pixel contact selects the spectral sensitivity by reverse-biasing the p-n junction of interest. The CdTe/HgTe alloy composition or x value of the n-type absorber layers determines the spectral cutoff characteristics of the detector in both detection bands. A positive (negative) operating bias voltage at the pixel contact with respect to the FPA common-ground contact provides reverse bias to the Band 2 (Band 1) p-n junction while forward biasing the Band 1 (Band 2) p-n junction for detection of longer (shorter) wavelength radiation.

Bi-color detectors based on HgCdTe are difficult to grow due to the strong dependency of the bandgap on the alloy composition. Slight variations of the growth temperature and the temperature non-uniformity across the CdZnTe substrates result in different alloy compositions and a shift of the cut-off wavelength over the FPA. Also, using back to back diodes to achieve the multicolor detectors increases the complexity and therefore, the cost of the associated ROICs.

- The two color SL detector structure ([43]) along with fully processed SL-FPA SEM picture are shown in figures 4.3(a) and 4.3(b), respectively.

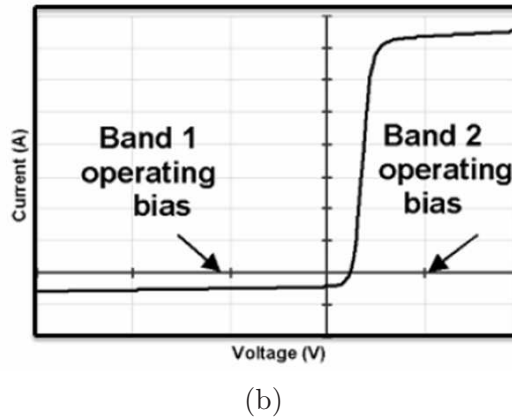
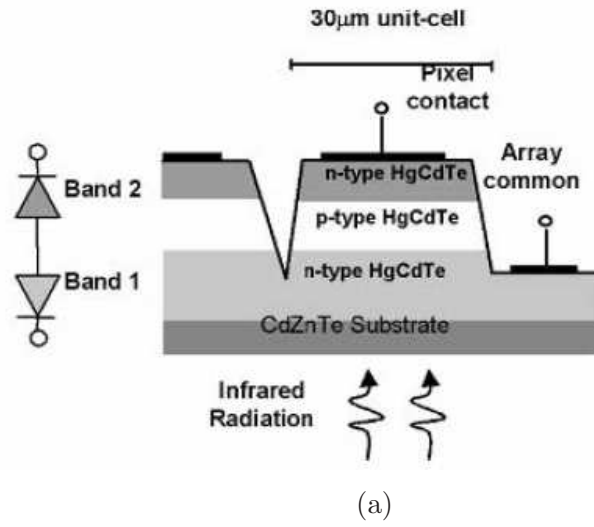


Figure 4.2: (a) cross-section schematic, and (c) typical I-V characteristic for a single-mesa, single-indium bump, dual-color detector design. With the appropriate polarity and voltage bias at the pixel contact, the Band 1 and Band 2 p-n junctions respond to shorter and longer wavelength infrared radiation, respectively.

The blue and red channel absorbing regions are achieved by changing the InAs and GaSb layer thickness. The common p-type contact layer and to the n-type contact layer of the lower diode are etched by a chlorine-based chemical assisted ion beam etching (CAIBE) process. CAIBE is also used to etch deep trenches for the electrical isolation of each pixel.

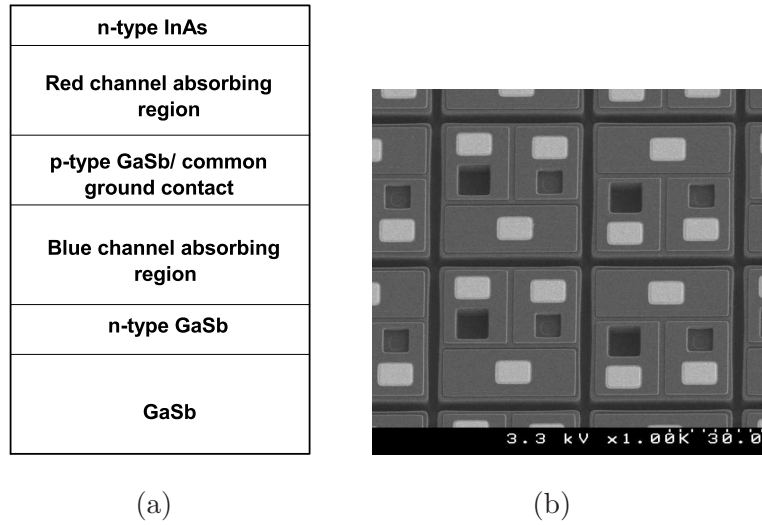


Figure 4.3: (a) Schematic (b) SEM picture of two-color InAs/GaSb superlattice detector

This two color SL FPA is based on two back to back diodes which has two disadvantages of high cost ROICs associated with this specific design. Also, two contacts per pixel leads to a complicated processing scheme.

In next section, we present a bias dependent dual band SL detector operating in the MWIR and LWIR region. One of the advantages of this design is that it is compatible with the standard single bump per contact processing, which reduces the cost and complexity associated with the fabrication process.

4.4 Epitaxial growth and fabrication of dual-color nBn SL detectors

To study the devices with type II InAs/(In)GaSb SL absorbers based on nBn design, we grew two samples, referred to structures A and B. Both structures A and B

were grown on a Te-doped GaSb(001) substrates. The device consists of 365 nm SL Si-doped InAs(8 monolayers (MLs), $n = 4 \times 10^{18} \text{ cm}^{-3}$)/GaSb(8MLs) bottom contact layer grown at 400°C , followed by an absorber layer. For structures A and B, it is an unintentionally doped 1.44 μm thick SL InAs(8MLs)/GaSb(8MLs), and 2.52 μm thick SL InAs(9MLs)/In_{0.25}Ga_{0.75}Sb(5MLs), respectively, grown at 400°C . A 100 nm Al_{0.2}Ga_{0.8}Sb follows the SL which acts as a barrier. The structures are capped with 0.0972 μm SL of Si-doped InAs(8MLs, $n = 4 \times 10^{18} \text{ cm}^{-3}$)/GaSb(8MLs) grown at 400°C . Figures 4.4(a),(b) shows a schematic representation of the heterostructures for both devices.

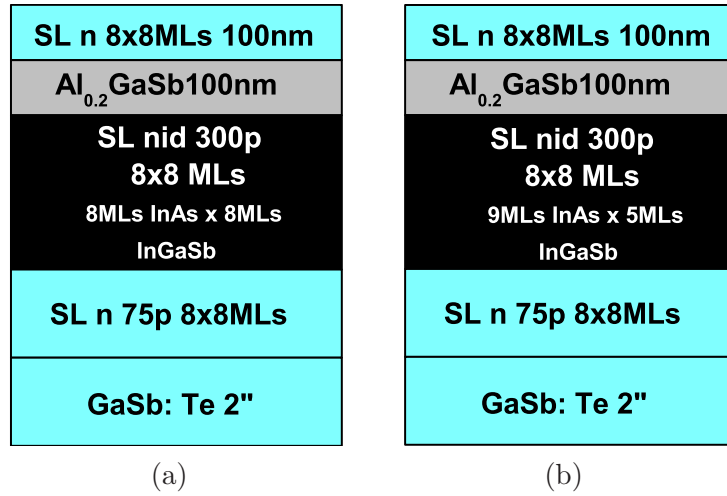


Figure 4.4: (a) structure A: two color MWIR detector ($\lambda_{c1} \sim 3.5 \mu\text{m}$ and $\lambda_{c2} \sim 4.5 \mu\text{m}$) and b) structure B: dual band MW-LWIR ($\lambda_{c1} \sim 3.5 \mu\text{m}$ and $\lambda_{c2} \sim 8.0 \mu\text{m}$).

The structural properties were assessed by high resolution X-ray diffraction. From the X-ray scans, the SL material is found to be lattice-matched to the substrate within 0.02%, while the Al_{0.2}Ga_{0.8}Sb layer peak is compressively strained to 0.32%.

The Al_{0.2}Ga_{0.8}Sb barrier is designed to have nearly zero valence band offset and large conduction band offset, blocking the majority carrier current, while allowing the collection of photocurrent. To obtain zero valence band offset, an optimization

of both the composition and the doping level of the ternary layer is required and is currently under study in our group.

As it was previously mentioned, one of the advantages of the nBn structures is its unique processing technique which eliminates surface currents. Figure 4.5 shows the current density at three temperatures for structure A for shallow ($0.1 \mu\text{m}$) and deep etched ($2 \mu\text{m}$) processed devices. A great reduction of current density in shallow etched device can be seen at lower temperatures in comparison with deep etched device. This is attributed to the reduction of leakage surface current of large devices (in this study $410 \mu\text{m}$) at lower temperature as compared to higher temperatures. processing of nBn structures (A and B) follows the same procedures described for nBn structures in section 3.6.2.

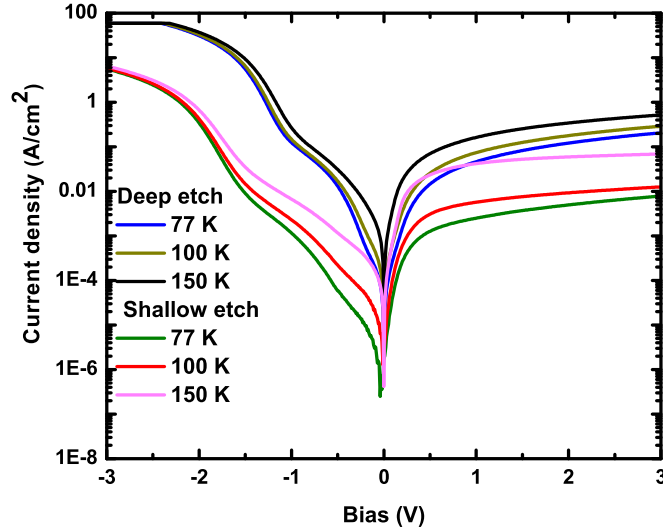


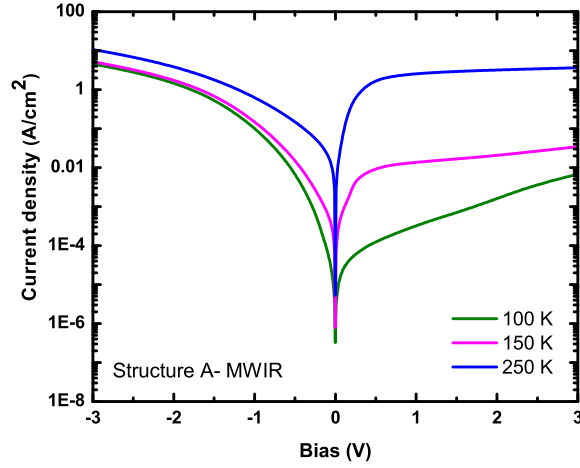
Figure 4.5: Current density at different temperatures for both shallow and deep etched devices.

4.5 Device characterization: results and discussions

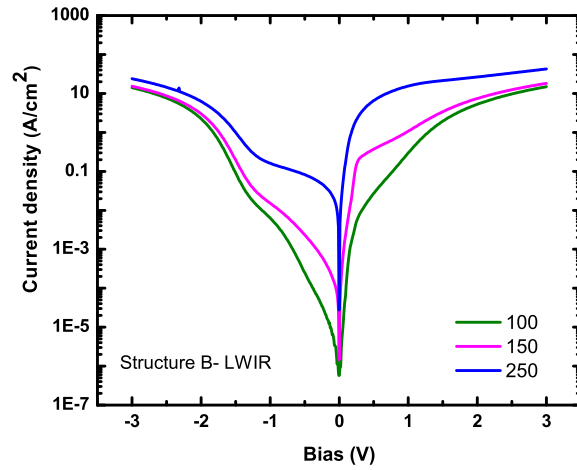
Figures 4.6(a), and (b) present the dark current density of structures A and B at temperatures ranging from 77 K to 300 K. The data shows that dark current density is higher in forward bias regime (positive voltage applied on the bottom contact). We attribute this to the position of $\text{Al}_{0.2}\text{Ga}_{0.8}\text{Sb}$ barrier. From the band alignment, it is clear that the AlGaSb barrier is more effective in reducing the current in the reverse bias (defined as negative voltage on the bottom contact).

The normalized relative spectral responses of structures A and B as a function of voltage bias are displayed in figures 4.7(a) and (b), respectively .

The data clearly show that the two color($\lambda_{c1} \sim 3.5 \mu\text{m}$ and $\lambda_{c2} 4.5 \mu\text{m}$) and($\lambda_{c1} \sim 3.5 \mu\text{m}$ and $\lambda_{c2} \sim 8 \mu\text{m}$) at 100 K and 150 K for A and B , respectively, can be seen under different polarity. Under forward bias (figure 4.8(a)), the photocarriers from the absorber are collected. Absorber layers are SL 8×8 MLs InAs/GaSb ($\lambda_{c2} \sim 4.5 \mu\text{m}$) and SL 9×5 MLs InAs/ $\text{In}_{0.25}\text{Ga}_{0.75}\text{Sb}$ ($\lambda_{c2} \sim 8.0 \mu\text{m}$) for structures A and B, respectively. When the device is under reverse bias (figure 4.8(b)), the photocarriers from the heavily n-doped top contact layer (SL InAs/GaSb 8×8 MLs) are collected and the photocarriers from the absorber are blocked by the barrier. Heavily doped InAs in $0.0972 \mu\text{m}$ InAs/GaSb SL of the top contact layer, results in a larger optical bandgap due to the Moss-Burstein effect and is the source of the signal at the shorter wavelength for both of the structures A and B. It is also important to mention that reverse bias signal is (50-100 times) weaker than the forward bias signal, which is consistent with the fact that the top contact layer is thinner and heavily doped in comparison with the absorber. Thickness optimization of the top contact layer will be studied to obtain a signal under reverse bias as strong as the signal from the absorber under forward bias.



(a)

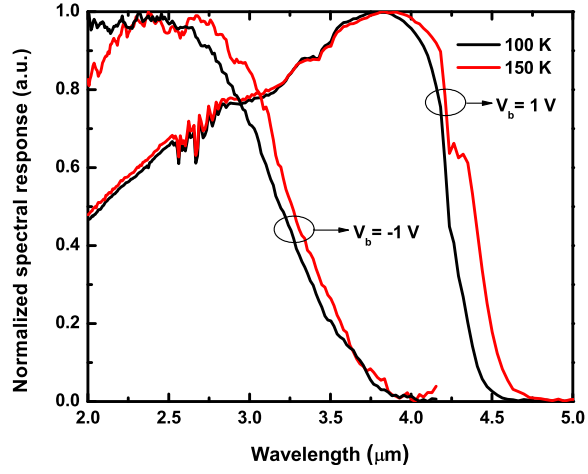


(b)

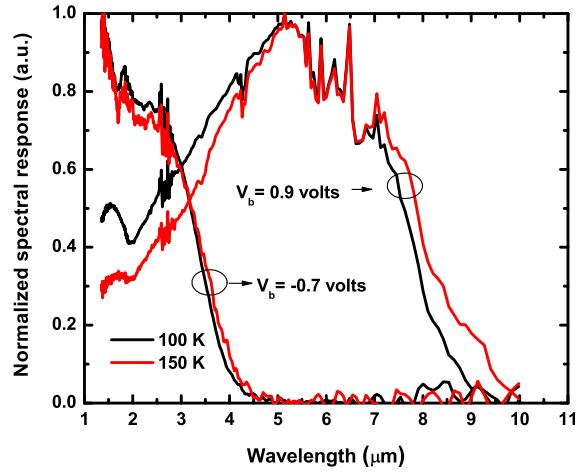
Figure 4.6: Current density at different temperatures for (a) structure A and (b) structure B.

Figure 4.9(a) shows responsivity and quantum efficiency versus wavelength for structure A. The peak responsivity was found to be $0.835 A/W$ at $3.5 \mu m$ with $V_b = 0.5V$. The responsivity and quantum efficiency at $4 \mu m$ was $0.74 A/W$ and 23%, respectively. No Antireflection (AR) coating was applied on the device.

The spectral specific detectivity $D^*(\lambda)$ was estimated using equation 3.8. Peak



(a)



(b)

Figure 4.7: Spectral response of structure (a) A and (b) B at different temperatures under forward bias and reverse ; V_{bis} the applied voltage to the device.

D^* was estimated to be $2.8 \times 10^{11} \text{ cmHz}^{1/2}/\text{W}$ at $4 \mu\text{m}$ at $V_b = 0.5 \text{ V}$.

The responsivity and quantum efficiency were also measured for structure B using the same setup as for structure A. The external quantum efficiency was calculated to be 12% and D^* was calculated to be $2.5 \times 10^{10} \text{ cmHz}^{1/2}/\text{W}$ at $5.5 \mu\text{m}$. The peak responsivity was 0.51 A/W also at $5.5 \mu\text{m}$. The responsivity and quantum efficiency

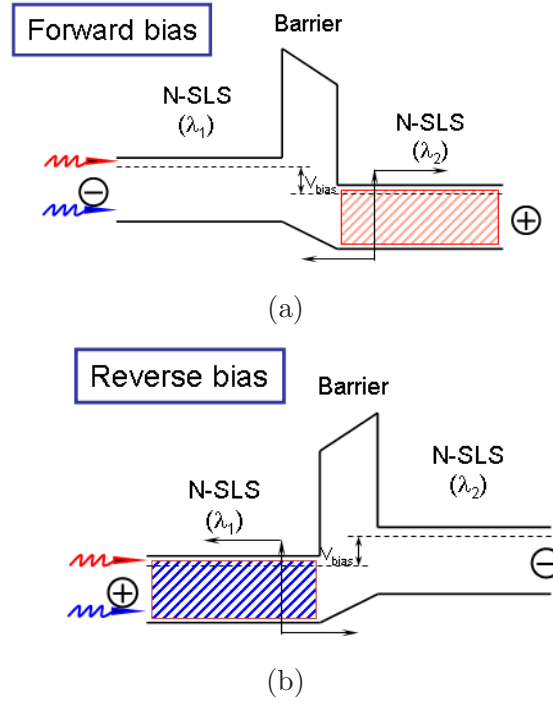
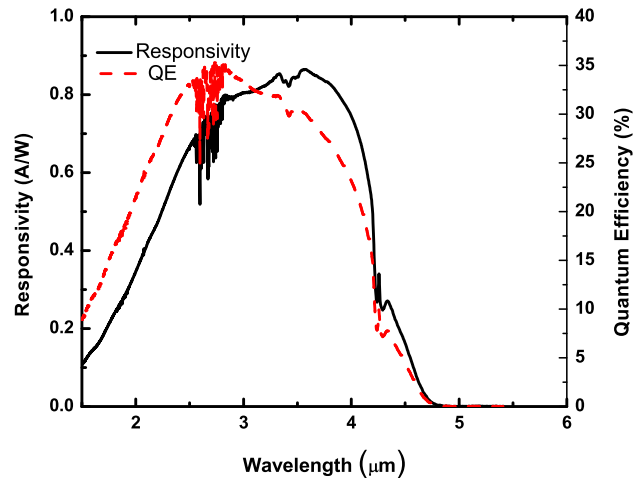


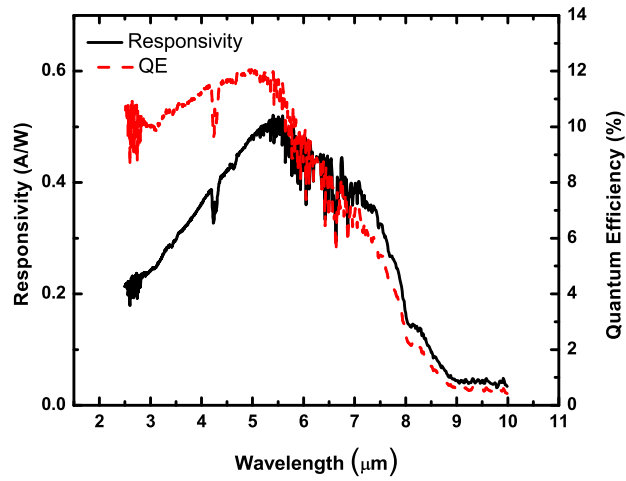
Figure 4.8: Two color nBn detector under (a) forward bias and (B) reverse bias

for structure B are shown in figure 4.9(b). The low responsivity and quantum efficiency for structure B could be due to lower absorption in LWIR SLs as compared to the MWIR SLs. Also the poor alignment of the valence band of the barrier with the 9 ML InAs/5 ML Ga_{0.75}In_{0.25}Sb SL could be an additional possible explanation for the relatively low quantum efficiency.

On the basis of results obtained from structures A and B we grew and fabricated another nBn device (structure C). Structure C was designed to improve the reverse bias signal and consists of thick MWIR and LWIR absorbers on both sides of the barrier. The schematic of structure C is shown in figure 4.10. The growth steps for sample C are as follow: first, a 480 nm bottom contact layer consisting of 8 MLs InAs:GaTe ($n = 4 \times 10^{18} \text{cm}^{-3}$)/8 MLs GaSb SL was grown. Then a 1.8 μm thick LWIR absorber formed by unintentionally doped 9 MLs InAs/ 5 MLs In_{0.25}Ga_{0.75}Sb



(a)



(b)

Figure 4.9: The responsivity (solid black line, left axis) and quantum efficiency (dotted red line, right axis) for (a) structure A, and (b) structure B.

SL was grown followed by a $1.5 \mu\text{m}$ thick MWIR absorber composed of 8 MLs InAs/ 8MLs GaSb SL. A 100 nm $\text{Al}_{0.2}\text{Ga}_{0.8}\text{Sb}$ barrier separated the two absorbers. The structure was capped with $\sim 0.1 \mu\text{m}$ top contact layer consisting of 8 MLs InAs:GaTe/8 MLs GaSb SL with the same doping level as the bottom contact layer. The device processing was similar to that of structures A and B.

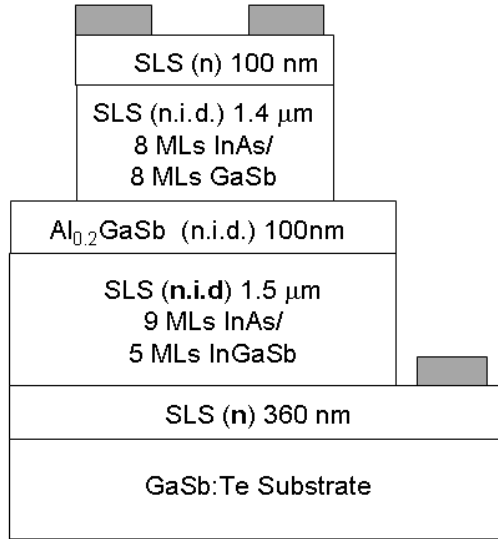


Figure 4.10: Structure C: Dual band MWIR/LWIR detector

As shown in figure 4.11, dark current density is higher in the forward bias regime (1.25 A/cm^2 at $+0.5V$) as compared to the reverse bias (0.338 A/cm^2 at -0.5 V). This is expected since the forward bias is dominated by the generation currents from the LWIR absorber while the reverse bias is dominated by the generation currents from the MWIR absorber. The dark current density in structure C is higher than the current densities found for structures A and B which is due to the larger depth of the first etch ($\sim 1.5 \mu\text{m}$) and therefore larger surface currents as compared to the first etch depth for structures A and B ($\sim 100 \text{ nm}$). The relatively large dark current density in the three structures can be improved with the optimized composition and thickness of the barrier layer.

The relative spectral responses for the bi-color structure is shown in figure 4.12. The data clearly shows cutoff wavelengths $\lambda_{c1} \sim 4.5 \mu\text{m}$ and $\lambda_{c2} \sim 8 \mu\text{m}$ under different polarities of applied bias. When forward bias is applied the carriers from the LW absorber are collected and when the reverse bias is applied the carriers from the MW absorber are collected.

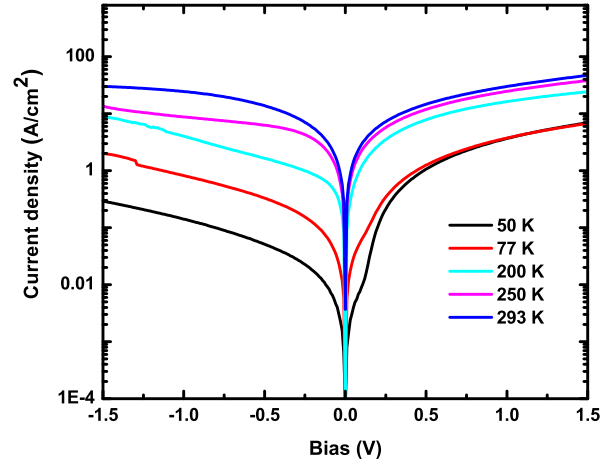


Figure 4.11: Dark current density of two-color SL detector (structure C)

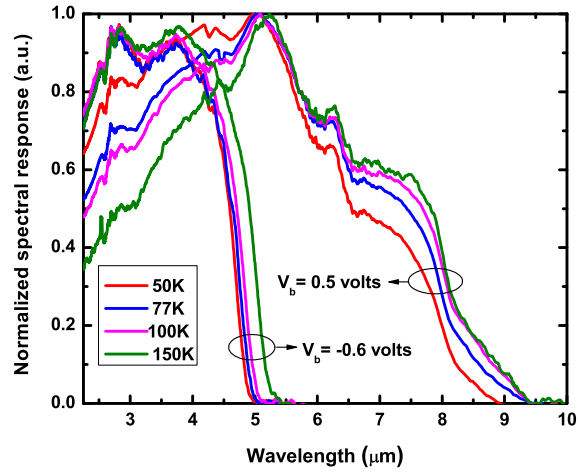


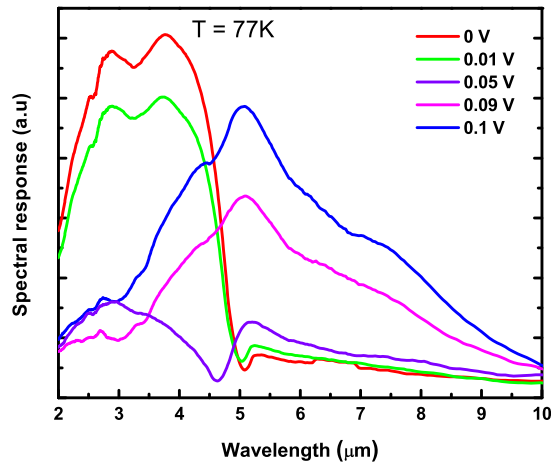
Figure 4.12: Spectral response of the bi-color structure at different temperatures under forward and reverse bias ; V_b is the applied voltage.

Since most present day ROIC apply a very small bias voltage we want to investigate the response close to zero bias. Figure 4.13(a) shows values of the spectral response of structure C between 0 and +0.1 V. The data clearly indicates the response cutoff shifts from MW to LW when the applied bias voltage varies between 0 and +0.1V. Figure 4.13(b) presents the intensity study of MWIR, LWIR, and

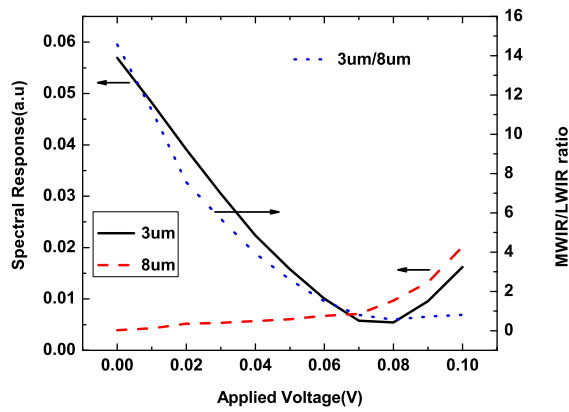
MWIR to LWIR ratio vs applied bias voltage. As the applied bias voltage increases from 0 to +0.1V, the MW intensity decreases, and LW intensity increases. The bias dependent feature of the spectral response, can be exploited by post-processing algorithms [45] to achieve high levels of spectral tuning and matched filtering. Due to this feature, a single detector can be operated at multiple biases sequentially, whereby the detector's spectral response changes each time with the applied bias. Therefore, the bias dependent spectral response can be used in algorithms to reconstruct the sources in the surrounding environment.

4.6 Conclusion

The multi-spectral capabilities of SL-based nBn structures were demonstrated using three different samples. Structure A and structure B showed two-color response with the change of polarity of applied bias at $3.5/4.5\mu\text{m}$, and $3.5/8\mu\text{m}$, respectively. Structure C was designed to have equal signal strengths from its absorbers under different polarities of applied bias. The spectral response for structure C, showed that LW to MW intensity ratio changes within very small bias voltage range which results in less expensive and complex multi-color FPA technology.



(a)



(b)

Figure 4.13: (a) The spectral response of structure C between 0 and +0.1V bias voltage, that is compatible with the bias range of present day ROICs. (b) the intensity study of MWIR, LWIR, and MWIR to LWIR ratio vs applied bias voltage at 77 K.

Chapter 5

Transport properties of type-II InAs/GaSb SLs

5.1 Introduction

In this chapter, first the measurement of the background carrier concentration of type-II InAs/GaSb SLs on GaAs substrates designed for operating in the MWIR and LWIR regimes of infrared spectrum are covered. The transport properties of SLs are characterized using temperature dependent Hall measurements. It is found that the conduction in the MWIR SLs (8ML InAs/8ML GaSb, $\lambda_c=4.5\mu\text{m}$) is dominated by holes at low temperatures ($>200\text{K}$) and by electrons at high temperatures ($<200\text{K}$). However, the transport in LWIR SL (13 ML InAs/7ML GaSb, $\lambda_c=8\mu\text{m}$) is dominated by electrons at all temperatures possibility due to the thicker InAs (residually n-type) and thinner GaSb (residually p-type) layers. By studying the in-plane transport characteristics of LW SLs grown at different temperatures, it is shown that interface roughness scattering is the dominant scattering mechanism at high temperatures (200K-300K). Next, the in-plane transport properties of LW SLs grown on GaSb

are studied. Due to highly conductive GaSb substrate, flip-chip bonding technique was used to remove the substrate. The experimental data was then analyzed using Quantitative Mobility Spectrum Analysis (QMSA) which showed indication of two types of carriers in the LW SL material system with activation energies indicating impurity donors.

5.2 Background and motivation

In order to further improve ambient temperature performance of detector material in terms of issues such as collection efficiency, one needs to have a better understanding of underlying carrier transport in this material. The study of transport in InAs/InGaSb SLs is important in its own right since carrier mobility affects charge collection in both photoconductive and photovoltaic modes of operation.

However, electrical transport measurements on these structures are difficult, especially at high temperatures, as the SLs are grown on highly conductive GaSb substrates. Commercially available GaSb substrates have, at best, a residual doping level of low 10^{17}cm^{-3} and substrates being significantly thicker than SLs, carriers from the former will have an overbearing contribution to electrical transport.

Several techniques have been reported to measure and analyze the electrical properties by different groups [46, 47, 48, 49, 50]. Some groups have reported Hall measurements by introducing a lattice matched quaternary AlGaAsSb buffer layer between the substrate and the superlattice [49], but this technique is only suitable at low temperatures where quaternary layer conductivity is sufficiently low. Temperature dependent capacitance-voltage measurements on “p-i-n” SL-based diodes, have been reported [51] and provide interesting values of background carrier concentration between 20 and 200 K. However, capacitance-voltage measurements do not provide complimentary information such as mobility and polarity of carriers.

In this study, we have grown both MW and LW SLs on GaAs substrates using interfacial misfit dislocation (IMF) arrays [1]. GaAs substrate is used as it suppresses the contribution of carriers from the substrate to the transport characteristics of SLs as compared to highly conductive GaSb substrates. The dislocations associated with large lattice mismatch between GaAs and GaSb are relieved at the GaAs/GaSb interface by 90 degrees misfit dislocation using interfacial misfit dislocation arrays (IMF) growth mode. We also have studied the in-plane transport properties of LW SLs on GaSb, where the substrate has been removed by the flip-chip bonding technique which the results are shown in the second part of the chapter.

5.3 Interfacial misfit dislocation arrays (IMF)

This method allows rapid strain relief at the heteroepitaxial interface through the formation of a two dimensional (2D), periodic, IMF array comprised of pure edge, 90° dislocations along both [110] and $\overline{[110]}$ directions. The IMF growth mode results in a high quality, thick GaSb epilayer on GaAs and exceptionally low defect densities ($<10^5 cm^{-2}$).

5.3.1 Growth of the GaSb/GaAs using IMF method

The GaAs substrate is deoxidized at 600°C prior to the growth of 100 nm of GaAs at 560 °C to obtain a smooth surface. After completion of the homoepitaxy, the substrate temperature is reduced to 510°C under constant As overpressure. Before the Sb growth is initiated, the As valve is closed allowing As adatoms to desorb leaving a Ga-rich surface. This process, confirmed by RHEED transition from an As-rich (2×4) to Ga-rich (4×2) surface, reduces As/Sb intermixing. Once the GaSb growth begins, the RHEED pattern resembles a 1×3 indicating that a thin film of

GaSb forms on the surface.

Figure 5.1 shows the strain-relaxed low defect density GaSb (120 nm) buffer on GaAs and the GaSb/GaAs interface along the [110] direction.

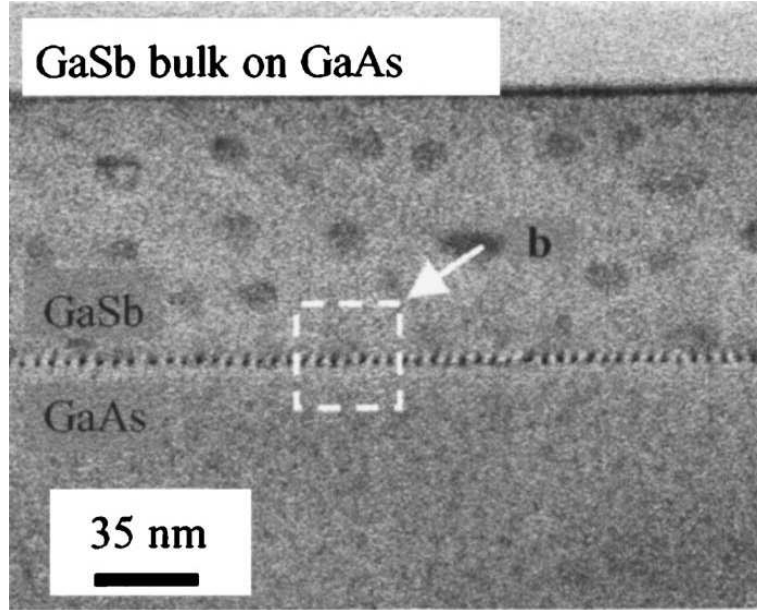


Figure 5.1: Cross-sectional TEM image of 120 nm of GaSb on GaAs showing a highly periodic array of misfit dislocations at the GaSb layer and the GaAs substrate [1].

5.4 Background carrier concentration of mid-wave and long-wave superlattices grown on GaAs

It is interesting to note that the constituent materials of the SLs have different polarity of background concentration. MBE grown InAs is residually n-type whereas GaSb is residually p-type. Thus the background concentration in the SLs is expected to depend on the thickness of the constituent InAs and GaSb layers. In this section, we report on temperature dependent Hall measurements to extract the background car-

rier concentration and activation energies in 8ML InAs/8ML GaSb MWIR ($\lambda_c \sim 4.5 \mu\text{m}$) and 13 ML InAs/7 ML GaSb LWIR ($\lambda_c \sim 8 \mu\text{m}$) SLs grown on GaAs substrates.

The structures were grown on semi-insulating GaAs (100) substrates. After the GaAs buffer layer, a layer of GaSb was grown using a layer of 90° interfacial misfit (IMF) arrays to relieve the strain at the GaAs/GaSb interface [1]. This dramatically reduces the number of threading dislocations that penetrate the active region of the device. GaSb based lasers and solar cells have been realized with defect densities less than 10^6cm^{-2} [52, 53, 54]. In our structures, a non-intentionally doped $2 \mu\text{m}$ thick SL of 8 ML InAs/ 8 ML GaSb was grown for the MW sample, and a non-intentionally doped $2 \mu\text{m}$ thick SL of 13 ML InAs/7 ML GaSb was grown for the LW sample. A 0.45 ML thick InSb layer was used to compensate the strain between the InAs and GaSb layers in the LW SLs. Detailed growth and interface optimization approaches can be found in chapter 3. To study the effect of interface roughness on the transport properties of LW SLs, four samples at different substrate temperatures were grown.

Magnetotransport measurements were performed on cleaved $1 \times 1 \text{cm}^2$ samples in the van-der-Pauw configuration (using a Hall setup with high impedance buffers and fully guarded voltage leads). AC excitation currents in the range of 100 to $500 \mu\text{A}$ at 18 Hz were applied to obtain good signal to noise ratio for these highly conductive samples. To control temperature in the range of 80 to 300 K, samples were mounted inside a vacuum dewar on a Joule-Thomson refrigerator stage (MMR Technologies) using silver paint (Fullam, Inc). Magnetic fields up to ± 0.9 Tesla were applied normal to the samples.

Figures 5.2(a),(b) and (c) show the resistivity, carrier concentration, and mobility of the MW SL at different measurement temperatures, respectively. The bandgap of the SLs is estimated to be 276 meV at 77 K and 248 meV at 300 K. The temperature dependent resistivity of MW SL sample (Figure 5.2(a)) shows a distinct change in the slope with temperatures below 200K showing an activation energy of

~ 24 meV and temperatures above 200 K showing an activation energy of ~ 193 meV. The discontinuous slope in this behavior indicates the presence of two types of carriers, p-type carriers at low temperatures (< 200 K) and n-type carriers at high temperatures (> 200 K) with very different activation energies. We believe that holes arising out of shallow impurities close to the valence band edge with an activation energy of ~ 24 meV are the dominant source of conduction at $T < 200$ K. At higher temperatures (> 200 K), the higher mobility electrons are activated from the deep impurity level (193 meV) and dominate the conduction. One possible source of these deep levels is the shallow level impurities in bulk InAs layers which due to the band line up between the InAs and SLs acts as deep impurity levels in the SL[15]. As shown in figure 5.2(b), Hall measurements reveal a “p-type” material at $T < 200$ K and “n-type” material at higher temperatures. We believe that behavior is due to the residual doping of the two constituent materials and their activation energies. InAs is residually n doped and GaSb is residually p doped. At low temperatures, holes in SL are activated due to their lower activation energy (23.86 meV) than the electrons and as the temperature increases the electrons from deep level impurities (193 meV) are activated and become the dominant source of conduction due to their higher mobility. The measured mobility in the MW sample shown in figure 5.2(c) also confirms the switching of majority carriers from holes to electrons at 200 K. As is expected the holes (p-type carriers) have lower mobility than the electrons (n-type carriers).

In-plane hall measurements were also performed on the LW SL samples which had 13 ML of InAs (residually n-doped) and 7 ML of GaSb, which is residually p-type doped. A 0.45 ML of InSb was introduced to strain compensate the superlattice. The bandgap of LW SL is estimated to be 150 meV at 77 K. This SL demonstrated an n-type behavior across all measurement temperatures possibly due to the large InAs thickness. Figure 5.3(a) shows the resistivity of the LW SL grown at 455 °C as a function of measurement temperature. Activation energy extracted from the

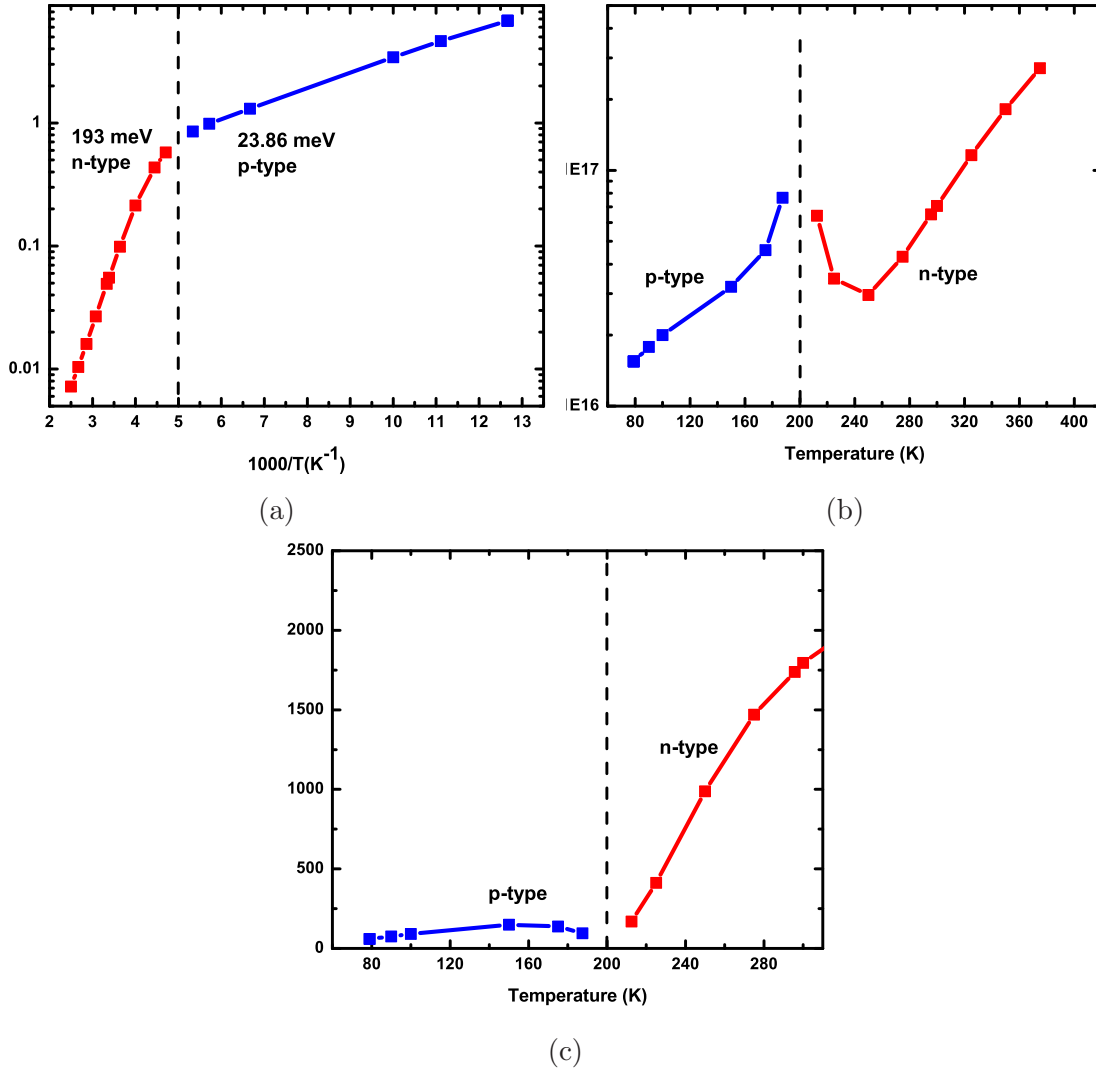


Figure 5.2: a) Hall resistivity, b) Hall carrier concentration, and c) Hall mobility of non-intentionally doped mid-wave SL versus measurement temperature; SL is residually p-type at temperatures below 200 K and n-type at temperatures above 200 K. From Hall resistivity two activation energies of 193 meV and 23.86 meV were extracted which indicates existence of shallow and deep impurity levels in the SL.

resistivity data reveals the existence of carriers with energy of 73.1 meV located in the middle of the band gap.

It has been shown that the growth temperature has a significant effect on the background concentration in LW SLs as shown by Burkle *et al* [49]. Figure 5.3(b) shows the carrier concentration as a function of measurement temperature for the LW SL samples grown at different temperatures. The carrier concentration is temperature independent in 80-125 K temperature range and as the temperature increases it increases exponentially. We believe that the ionized vacancies and defects in the SL are the source of carriers at low temperatures. As figure 5.3(c) shows, the samples grown at higher temperature have larger carrier concentration at low measurement temperatures which is due to larger vacancy and defect density, and the carrier concentration is independent of growth temperatures for measurement temperatures larger than 200 K. The thermally generated intrinsic carriers in the SL are the dominant source of the carriers at these temperatures, therefore there is little carrier concentration variation between samples grown at different substrate temperatures. These carriers are intrinsic carriers associated with generation-recombination mechanism in the LW SL.

Figure 5.4(a) shows the mobility of the LW SL as a function of the measurement temperature for the samples grown at different substrate temperatures. The behavior follows the expected temperature dependence of mobility spectrum where at low temperatures mobility is limited by ionized impurity scattering and at higher temperatures mobility is phonon scattering limited. However, the dependence related to the ionized impurity and phonon scattering for SL do not exactly follow the classical $T^{3/2}$ and $T^{-3/2}$ behavior for bulk material. This deviation is associated with the SL material system in which interface scattering and defects are other sources of scattering affecting the mobility. The effect of interface scattering is significant when mobility spectra of the samples grown at different substrate temperatures are compared. As shown in figure 5.4(a), for temperatures greater than 200 K, the mobility of samples grown at higher substrate temperature is less dependent on the measurement temperature. This behavior suggests that at higher growth tempera-

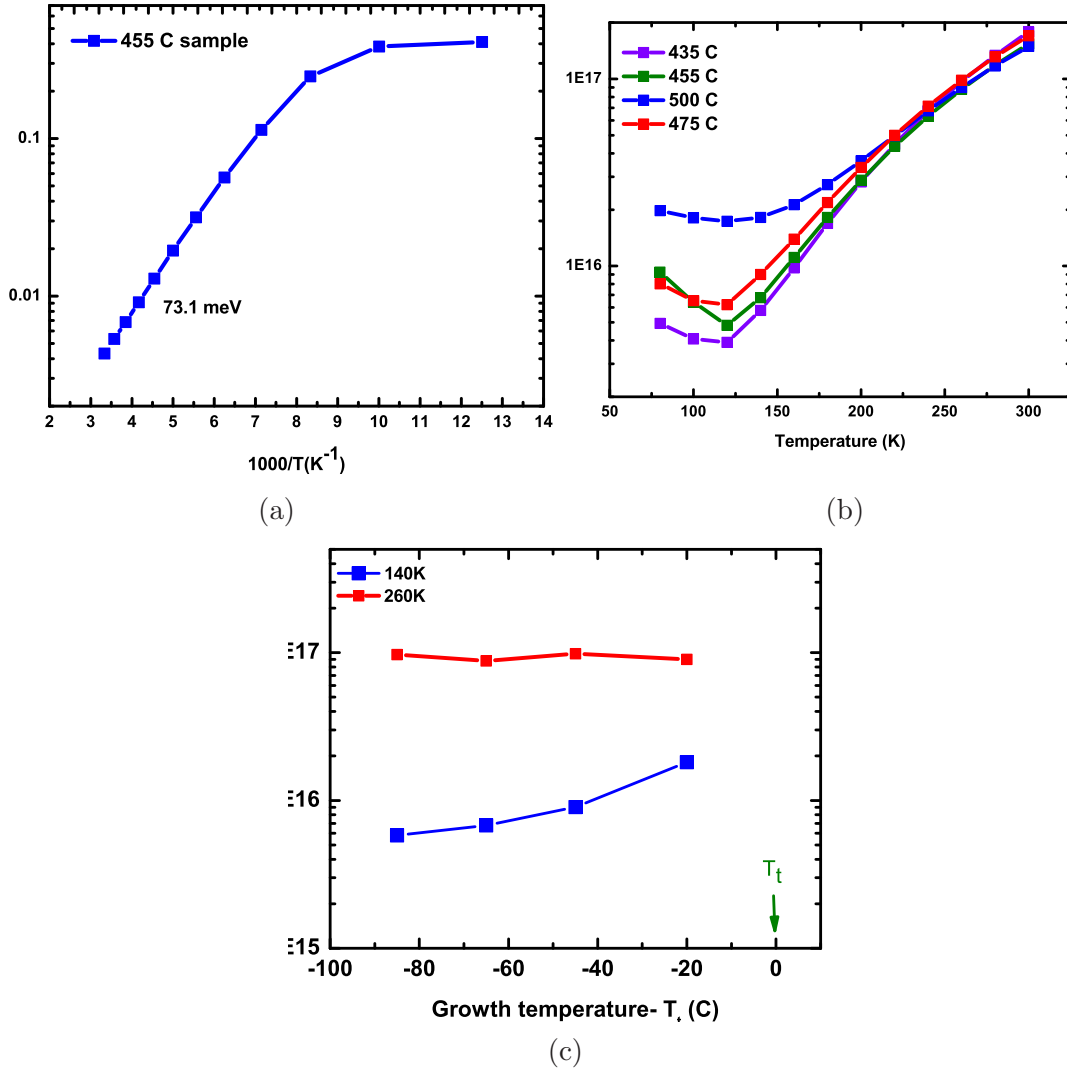


Figure 5.3: a) Hall resistivity of non-intentionally doped long-wave SL versus measurement temperature, b) Hall carrier concentration versus measurement temperature, and c) Hall carrier concentration dependence on growth temperature; SL is residually n-type at all of the measurement temperatures. At low measurement temperatures extrinsic carriers and at high measurement temperatures intrinsic carriers are the dominant source of carriers in the LW SL.

tures interface scattering is the dominant source of the scattering as compared to other sources of scattering like phonon and ionized impurity scattering, therefore SL mobility is independent of the measurement temperature. Figure 5.4(b) shows the

peak mobility for the samples grown at different temperatures.

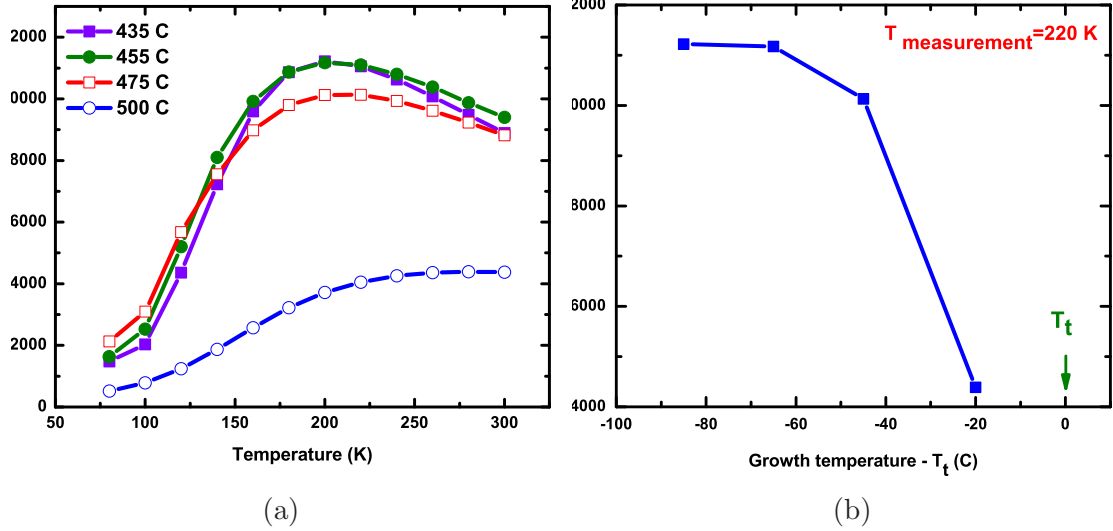


Figure 5.4: a) Hall mobility versus measurement temperature, and b) Hall peak mobility of non-intentionally doped long-wave SL versus growth temperature; As the growth temperature increases, interface scattering becomes the dominant source of scattering in the SL which decreased the mobility and causes temperature independent behavior of the mobility. Also due to interface roughness scattering peak mobility decreases.

To understand the decrease in peak mobility as the growth temperature increases, one should note that the dependence of mobility on the interface roughness is given by [55, 56],

$$\mu^{-1} \propto g(\Lambda, D)\Delta^2 D\Lambda^2(\partial E/\partial d)^2 \quad (5.1)$$

where Δ is height fluctuations associated with interface roughness in SLs, Λ is a correlation length of Gaussian-like fluctuations, D is the SL period, g accounts for screening and the relation between the electron wavelength and the correlation lengths, E is the electron energy, and d is the well width. As the substrate temperature increases, the interface roughness (Δ) which is the main source of scattering increases and therefore, μ decreases. Also from equation 5.1 the sixth power dependence [57]

of mobility on the well width can be obtained which can explain the higher peak mobility of LW SLs with 13 MLs of InAs well-type layer as compared to MW SLs with 8 MLs of InAs well-type layer.

5.5 Transport properties of longwave SLs on GaSb substrate

All of type-II InAs/GaSb superlattice detectors are grown on GaSb substrates, therefore, it is important to study the in-plane and vertical transport properties of these SLs on GaSb substrates and compare that to the results obtained in the previous section on GaAs substrates. These measurements are complicated due to the highly conducting GaSb substrate. The complication arises because of the significant contribution of the GaSb substrate carriers to the transport phenomenon in the SL structure. To overcome the complexity, the substrate is removed by flip chip bonding technique. It is worth mentioning that this project is an ongoing and long project which will be continued as future tasks as well.

5.5.1 Growth, processing, characterization of the long-wave superlattices on GaSb substrate

Growth

The substrates were initially outgassed under a vacuum, and the surface oxide was then removed at high (535°C) temperature under an Sb flux. The temperature of (1×3) to (2×5) reconstruction transition (T_t) on GaSb surface observed on the RHEED pattern was taken as a reference for all the growth temperatures. This transition temperature (T_t) is the same for all the GaSb substrates under the given

Chapter 5. Transport properties of type-II InAs/GaSb SLs

Sb flux. A 100 nm $\text{Al}_{0.2}\text{Ga}_{0.8}\text{Sb}$ etch stop layer was then grown. After the etch stop layer, 13 MLs InAs/ 0.726 MLs InSb/ 7 MLs GaSb superlattice with a total thickness of 2 μm was grown at different growth temperatures, $T_t\text{-}45^\circ\text{C}$, $T_t\text{-}65^\circ\text{C}$, $T_t\text{-}85^\circ\text{C}$, and $T_t\text{-}95^\circ\text{C}$. The schematic and HRXRD of this structure are shown in figures 5.5(a) and (b), respectively .

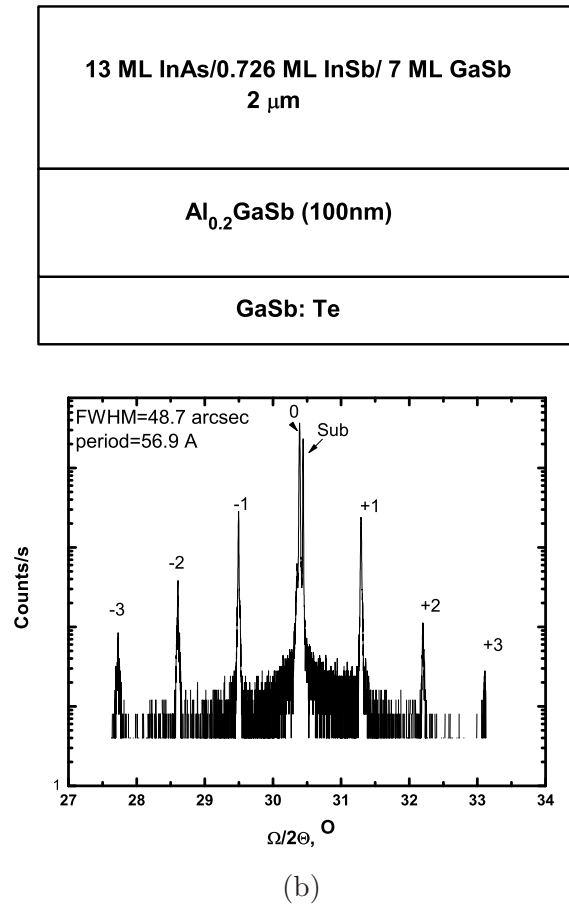


Figure 5.5: (a) Long-wave SL structure schematic (b) HRXRD of the sample grown at $T_t\text{-}45^\circ\text{C}$ used for transport studies.

Processing

Three masks were used in this step. SiN was deposited at the top of the sample. Standard optical photolithography was used for all the three steps. In the first step the sample was etched to the top of the SLs. Then UBM was deposited as Ti/Ni/Au (50/50/400 nm). In the last step a 1.5 μm thick indium layer was deposited. Also, processing of fanout included deposition of metal contacts Ti/Ni/Au (50/50/400 nm). Next, Reflow and bonding of the sample and fanout were done, and then the substrate was removed. The schematic of the main steps of processing are shown in figure 5.6.

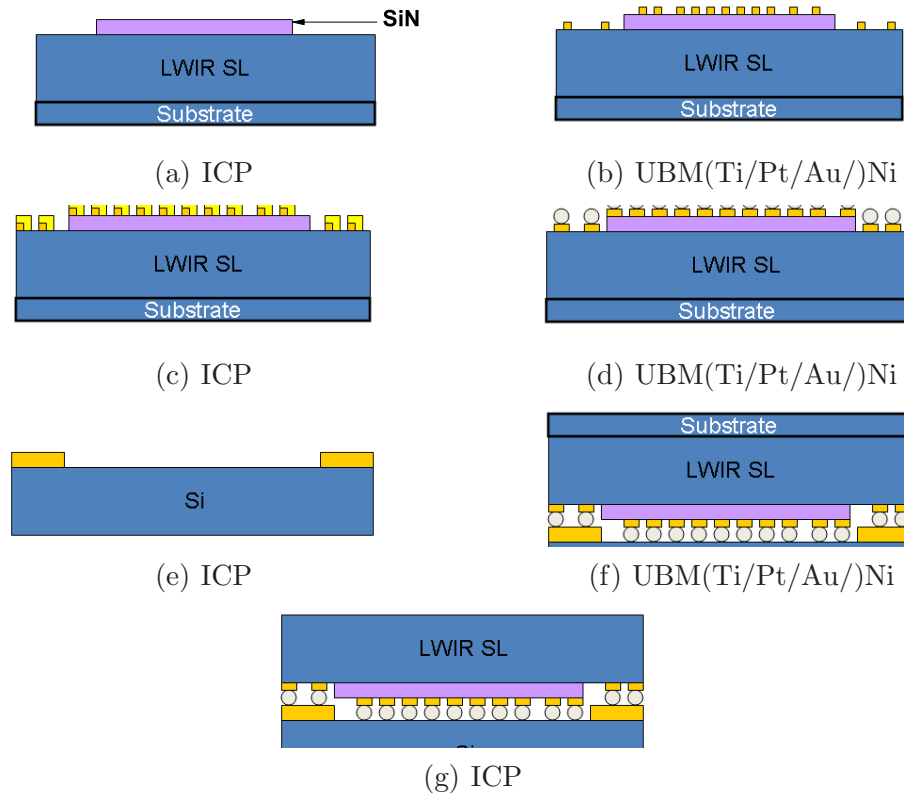


Figure 5.6: Main steps of processing for substrate removal (flip-chip method)

Characterization

To study the lateral and vertical SL transport, different sample geometries are used. In this section the lateral transport geometry and measurements are presented. The vertical transport studies are an ongoing project and will be mentioned as future work in chapter 6. To study the lateral transport, the processed flip-chip samples are used in the van der Pauw configuration (figure 5.7). In the van der Pauw measurements four ohmic contacts are placed on the sample, where the contacts must be on the boundary of the sample and must be very small (see figure 5.7).

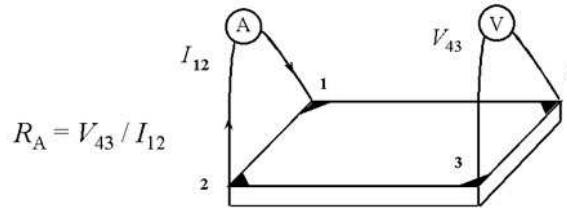


Figure 5.7: Classical form of the sample for van der Pauw method measurements.

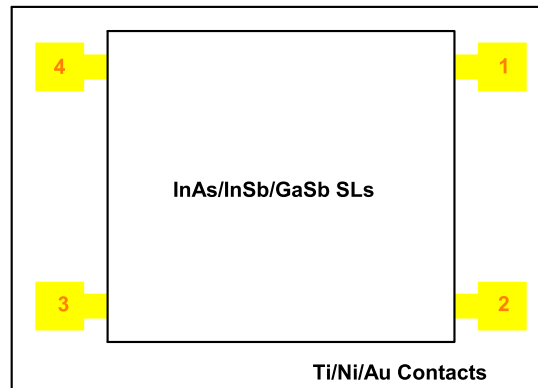


Figure 5.8: The van der Pauw configuration for lateral LW SL transport studies

To make a measurement, current passes along one edge (3,4) of the sample and the voltage across the opposite edge (1,2) is measured. From these two values, a

resistance is found:

$$R_{1234} = \frac{V_{12}}{I_{34}} \quad (5.2)$$

Hall coefficient and resistivity are obtained as following:

$$R_H = \frac{W}{B} R_{1234} \quad (5.3)$$

Where R_H is the hall coefficient, B is the magnetic field and W is the sample thickness.

$$\rho = \frac{\pi W}{\ln 2} \left(\frac{R_{1234} + R_{2341}}{2} \right) f(Q) \quad (5.4)$$

Where ρ is the resistivity and $f(Q)$ is a factor which is only a function of ratio R_{1234}/R_{2341} . R_{1234}/R_{2341} and $f(Q)$ are related through the following transcendental equation,

$$\cosh \left\{ \frac{(R_{1234}/R_{2341}) - 1 \ln 2}{(R_{1234}/R_{2341}) + 1} \frac{1}{f} \right\} = \frac{1}{2} \exp \frac{\ln 2}{f} \quad (5.5)$$

The hall experimental data is analyzed by Quantitative Mobility Spectrum Analysis (QMSA) method. QMSA is a method and apparatus to produce the conductivity-mobility spectrum of an isotropic semiconductor material using the experimental data this algorithm gives the electrical transport information under high magnetic fields on multiple carrier devices.

As shown in figure 5.9(a), hall coefficient and resistivity were measured for magnetic fields up to 12 T. figure 5.9(b) shows the mobility spectrum obtained from QMSA analysis of data shown in figure 5.9(a). QMSA shows indication of two carriers shown as E1 and E2 in figure 5.9(b). All of the peaks under E2 are considered as one carrier (E2). As shown in figure 5.9(c) the fit shows a broad spectrum (E2) for wide range of temperatures which could be related to the errors associated with the QMSA algorithm. In figure 5.9(b), holes from this spectrum

were interpreted as ghost peaks. These are an artifact from the QMSA algorithm, caused essentially by noise. The algorithm adds holes under the electron peak in order to obtain the best fit to the experimental data.

Carrier concentration of the two types of the carriers was calculated using :

$$n = \frac{\sigma}{e\mu} \quad (5.6)$$

Where σ is the conductivity and μ is the mobility obtained from QMSA. The carrier concentration vs $1000/T$ is curve fit to the equation:

$$n = \frac{n_{0,s}}{W} e^{-\left(\frac{E_a}{K_B T}\right)} \quad (5.7)$$

Where E_A (the activation energy) , and $n_{0,s}$ (density of states) are found to be 10.8 meV, $6.1 \times 10^{13} \text{cm}^{-2}$ for E1 and 7.29 meV, $1.9 \times 10^{13} \text{cm}^{-2}$ for E2 (figure 5.10(a)).

The activation energies indicates shallow impurity donors of about 10 meV below the conduction band of the SL, which is shown as the dashed line in figure 5.10(b).

5.6 Conclusion

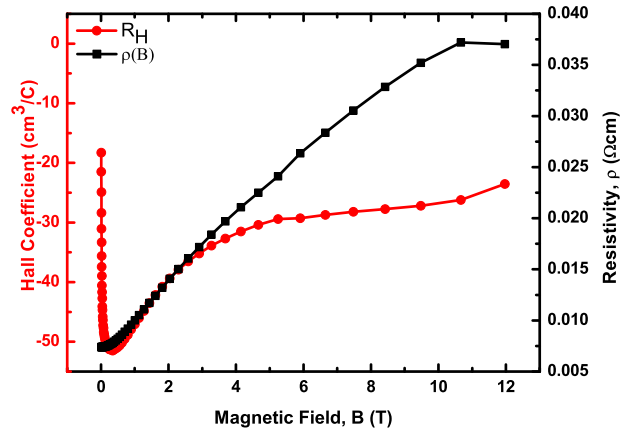
The residual doping of the 8 ML InAs/ 8 ML GaSb on GaSb substrate is found to change from p type to n type as the measurement temperature increases. The transition was attributed to the difference in activation energies of p-type and n-type carriers in the MW SL. In-plane transport study on 13 ML InAs/0.45 ML InSb/ 7 ML GaSb (LW samples) shows n-type carriers for all the measured temperatures. By varying the substrate temperature during the growth, it is found that interface scattering is one of the dominant sources of the carrier scattering mechanisms in the SL material system, and affects the transport properties of the SL. Also, transport measurement of SLs grown on GaSb were analyzed by quantitative mobility spectrum

Chapter 5. Transport properties of type-II InAs/GaSb SLs

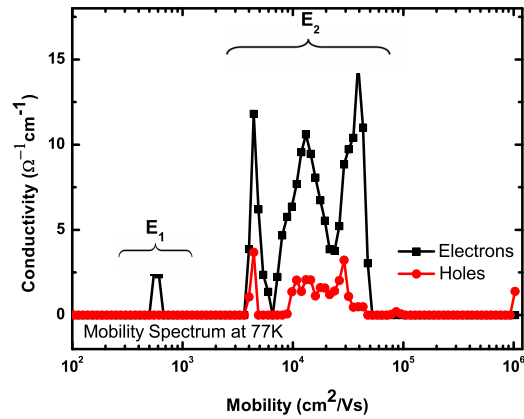
analysis algorithm. Two types of carriers (E1 and E2) were extracted with mobilities in high $10^2 \text{cm}^2/\text{V.s}$ and low $10^4 \text{cm}^2/\text{V.s}$ for E1 and E2, respectively. Activation energies of E1 and E2 indicate shallow impurity level donors close to the conduction band of the SL.

Due to different errors associated with the sample geometry, hall measurements, and QMSA algorithm, another set of samples will be studied for both in-plane and vertical SL transport studies on GaSb substrates.

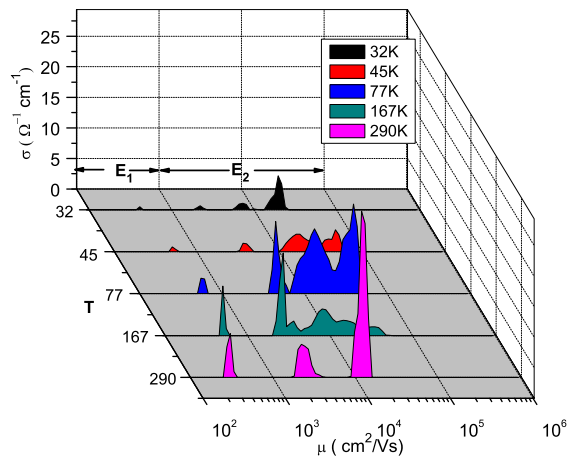
Chapter 5. Transport properties of type-II InAs/GaSb SLs



(a)



(b)



(c)

Figure 5.9: (a) Hall experimental data for magnetic field range of 0-12 T (b) Mobility spectra obtained from QMSA algorithm at 77 K (c) Mobility spectra obtained from QMSA algorithm at temperature range of 32-290 K.

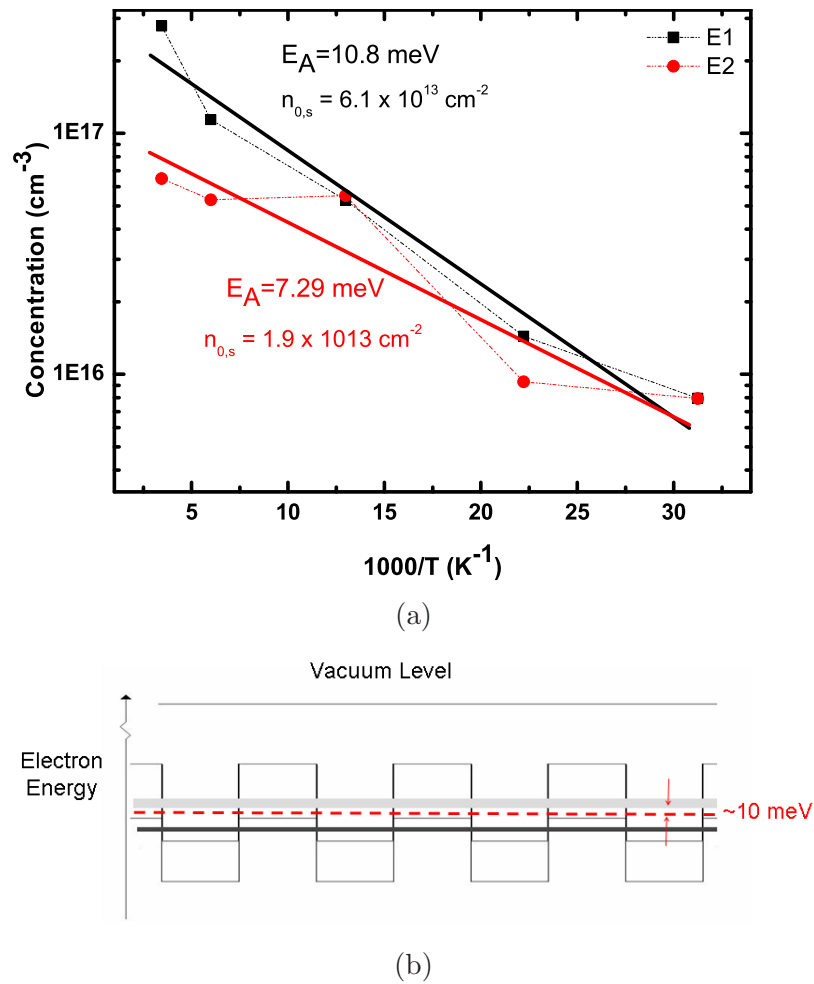


Figure 5.10: (a) Carrier concentration versus 1/T for LWIR SLs on GaSb substrate; Two activation energies are extracted, indicating (b) shallow impurity donor levels close to the SL conduction band

Chapter 6

Conclusions and Future Work

6.1 Conclusion

This work is focused on development of high performance infrared InAs/GaSb SL detectors. SL detector technology has inherent advantages over present-day detection technologies. InAs/GaSb SL has high responsivity because of strong absorption of normal incidence photons. Larger electron effective masses that are not directly dependent on the bandgap energy lower the tunneling current compared with bulk materials with the same bandgap energy. Different combinations of superlattice periodicity or constituent material composition can be utilized to tune the superlattice bandgap which can be used to provide multicolor capability. Also, the light-hole and heavy-hole band separation can be adjusted to reduce Auger recombination.

In chapter 1 of this dissertation we introduced the general concept of infrared detection. Detection principles (with concentration on photovoltaic effect), detector types (thermal and photon) and conventional figures of merit (external quantum efficiency, noise equivalent power, spectral detectivity) were discussed. Finally, pros and cons of competitive infrared technologies (MCTs, bulk InSb, and QWIPs) were

Chapter 6. Conclusions and Future Work

described and alternative technology for IR detection (based on type-II InAs/GaSb SLs) was introduced.

In chapter 2 the design, growth, processing, optical and electrical characterization of InAs/GaSb IR detectors were explained. We used next-nano and sentaures TCAD softwares for the simulation of the SLs. Material growth using solid source molecular beam epitaxy was briefly explained. We characterized structural, optical and morphological properties of as-grown material by XRD, absorption and AFM techniques, respectively. Processing of a single-pixel device was also covered. The optical and electrical characterization of the devices included the explanation of temperature dependent IV measurements, spectral response measurements using a FTIR spectrometer and the responsivity measurement setup.

In chapter 3, first the growth of InAs/GaSb SLs on GaSb substrates by molecular beam epitaxy (MBE) technique was presented. The two main parameters of temperature and interfaces for the growth of SLs were discussed. We found that optimal temperature for deposition of SL is 45° lower than temperature T_t of (1×3) to (2×5) reconstruction transition observed on the GaSb surface under 1×10^6 Sb-flux. Choice of shutter sequence during SL growth is important since it determines which type of interface (“GaAs” - like, “InSb-like”, or both) will be formed between compositionally abrupt GaSb and InAs layers. We found introducing InSb layer for strain compensation between InAs and GaSb layers produces the best structural properties. Since the lattice constant of InSb (GaAs) is much larger (smaller) than that of the GaSb, an insertion of few monolayers of these materials into SL allows to grow strain-compensated SL material. Thus, detectors with thick SL region (absorber) can be grown without degrading its quality. Since external quantum efficiency is proportional to the absorber thickness, detectors with enhanced values of QE can be grown. Detector structure with 2 μm of SL absorbing region has been grown. The HRXRD analysis revealed excellent crystalline quality of the film; the FWHM of the

Chapter 6. Conclusions and Future Work

first order satellite SL peak was found to be equal to 16 arcsec and lattice mismatch was about 0%. In this chapter, high performance mid-infrared pin InAs/GaSb SL detector ($\lambda_{cut-off}$ was $\sim 4.5 \mu\text{m}$ at 77 K) grown by molecular beam epitaxy was presented. The structural, optical and electrical properties were characterized using X-ray crystallography, IV and responsivity measurements. At $V_b = -0.3 \text{ V}$, the total dark current was equal to 1.34×10^{-6} at 77 K which is comparable to the lowest published dark current densities reported by other groups.

Next, based on the optimized longwave growth conditions, three long-wave pin devices with different absorbing region doping were studied. The long-wave pin with $5 \times 10^{15} \text{ cm}^{-3}$ absorber p-doping level showed the best device performance. The concept of nBn devices was presented. Devices based on nBn design have lower dark current density as compared to the conventional pin designs due to suppression of the currents associated with Shockley-Read-Hall centers and mesa lateral surface imperfections. The comparison between shallow etched long-wave nBn device and the optimized long wave pin device ($5 \times 10^{15} \text{ cm}^{-3}$ p-doped absorbing region) showed nBn devices have the potential to have higher signal to noise ratio as compared to the pin devices. Temperature dependent I-V measurements showed 0.05 A/cm^2 dark current density at $+0.1 \text{ V}$ for nBn device as compared to 0.2 A/cm^2 at -0.1 V at 77 K for pin device. Also nBn devices showed higher responsivity as compared to the pin devices due to elimination of Shockley-Reed-Hall recombination centers associated with depletion regions and therefore, more carriers are extracted from the absorbing region which increases the responsivity of these devices. nBn devices can be further optimized by studying the barrier and absorber doping level as well as barrier material and composition.

In chapter 4 the growth, processing and characterization of two-color InAs/GaSb SL nBn detectors with cutoff wavelengths in mid-wave and long-wave regimes were presented. First, growth, processing and characterization of the two samples, re-

Chapter 6. Conclusions and Future Work

ferred to structures A and B were presented. Both structures A and B had identical structure except structure A had a midwave absorbing region and structure B had a long-wave absorbing region. Two structures were fabricated out of the same growth material, one with a shallow top contact isolation etch and one with a conventional mesa structure for both mid-wave (A), and long-wave (B) samples. The shallow etched device dark current was reduced by two orders of magnitude at 77 K compared with the deep etched device for structure A. The current density was equal to $2.3 \times 10^{-6} A/cm^2$ and $3.1 \times 10^{-4} A/cm^2$ for shallow and deep etched devices at $V_b = 0.1 V$ and $T = 77 K$, respectively. The responsivity and QE for sample A were measured at $4 \mu m$ to be $0.74 A/W$ and 23% respectively. The responsivity for sample B was low, $0.51 A/W$ at $5.5 \mu m$, the expectation is that this will be increased in future devices.

Spectral response showed that the two color responses ($\lambda_{c1} \sim 3.5 \mu m$ and $\lambda_{c2} \sim 4.5 \mu m$) and ($\lambda_{c1} \sim 3.5 \mu m$ and $\lambda_{c2} \sim 8.0 \mu m$) at 100 K and 150 K for samples A and B, respectively, under different polarity of applied bias. Under forward bias the photocarriers from the absorber are collected. Absorber layers are SL 8×8 MLs InAs/GaSb ($\lambda_{c2} \sim 4.5 \mu m$) and SL 9×5 MLs InAs/ $In_{0.25}Ga_{0.75}Sb$ ($\lambda_{c2} \sim 8.0 \mu m$) for structures A and B, respectively. When the device is under reverse bias the photocarriers from the heavily n-doped top contact layer (SL InAs/GaSb 8×8 MLs) are collected and the photocarriers from the absorber are blocked by the barrier. Heavily doped InAs in $0.0972 \mu m$ InAs/GaSb SL of the top contact layer, results in a larger optical bandgap due to the Moss-Burstein effect and is the source of the signal at the shorter wavelength for both of the structures A and B. It is also important to mention that reverse bias signal is (50-100 times) weaker than the forward bias signal, which is consistent with the fact that the top contact layer is thinner and heavily doped in comparison with the absorber.

On the basis of results obtained from structures A and B another dual-color nBn

Chapter 6. Conclusions and Future Work

device (structure C) was grown and fabricated. Structure C was designed to improve the reverse bias signal and consists of thick MWIR and LWIR absorbers on both sides of the barrier. It consisted equal thickness of both MWIR and LWIR absorber regions separated with $\text{Al}_{0.2}\text{GaSb}$ barrier. The spectral response showed cutoff wavelengths $\lambda_{c1} \sim 4.5 \mu\text{m}$ and $\lambda_{c2} \sim 8.0 \mu\text{m}$ under different polarities of applied bias. When forward bias is applied the carriers from the LW absorber are collected and when the reverse bias is applied the carriers from the MW absorber are collected. The spectral response for structure C, showed that LW to MW intensity ratio changes within very small bias voltage range which results in less expensive and complex multi-color FPA technology.

Chapter 5 was devoted to transport studies of both mid-wave and lon-wave InAs/GaSb SL material system. To prevent the effect of carriers from the high conducting GaSb substrates, two methods were undertaken. In the first method, samples were grown on semi-insulating GaAs substrates. In the second method the GaSb substrate was removed by flip chip bonding technique.

The residual doping of the 8 ML InAs/ 8 ML GaSb grown on GaAs was found to change from p-type to n-type as the measurement temperature was increased. The transition was attributed to the difference in activation energies of p-type and n-type carriers in the MW SL. In-plane transport study on 13 ML InAs/0.45 ML InSb/7 ML GaSb (LW samples) grown on GaAs showed n-type carriers for all the measured temperatures. By varying the substrate temperature during the growth, it was found that interface scattering is one of the dominant sources of the carrier scattering mechanisms in the SL material system, and affects the transport properties of the SL. Also, transport measurement of LW SLs grown on GaSb were analyzed by quantitative mobility spectrum analysis algorithm. Two types of carriers (E1 and E2) were extracted with mobilities in high $10^2 \text{cm}^2/\text{V.s}$ and low $10^4 \text{cm}^2/\text{V.s}$ for E1 and E2, respectively. Activation energies of E1 and E2 indicate shallow impurity

level donors close to the conduction band of the SL. Further investigation of lateral and vertical transport properties of SLs will be covered as future work plan.

6.2 Future work

6.2.1 SL transport studies

One of the fundamental properties of the SLs absorber layer is the background carrier concentration as it determines the minority carrier lifetime and diffusion lengths of carriers. As it was described in chapter 5, in order to study the transport properties of SLs grown on GaSb substrates, one needs to avoid the highly conducting GaSb substrate carriers. Therefore, different techniques are used to remove the substrate.

In order to remove the GaSb substrate, two different techniques will be used. The first method is the flip-chip bonding technique that was covered in chapter 5 for lateral transport studies. However, our previous measurements were erroneous due to the sample geometry, hall measurements, and QMSA algorithm. As a result, these measurements will be repeated with the flip-chip bonding substrate removal technique.

Another method to remove the substrate is to use mechanical and chemical polishing techniques. Figure 6.1 shows a set of processing steps [50] for removing the SL substrate in lateral transport studies. In this method, InAsSb etch stop layer is grown between the buffer layer and SL epi-layer. The sample is frontside-bonded to a host substrate using liquid epoxy adhesive. After mechanical polishing of GaSb substrate down to 80/100 μm thickness, selective wet etchants can be used to remove the GaSb substrate as well as the InAsSb etch stop layer.

To study the vertical transport properties a different sample geometry is used.

Chapter 6. Conclusions and Future Work

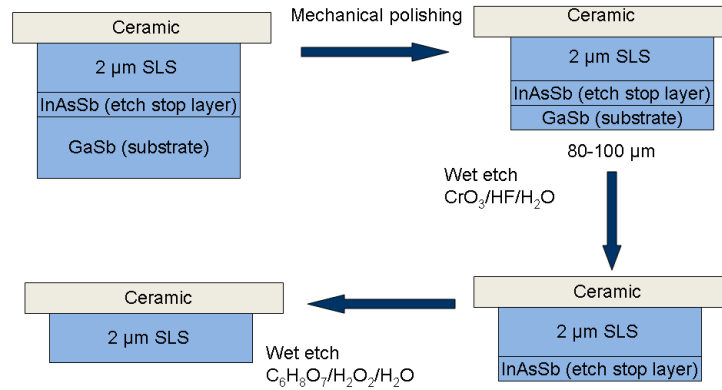


Figure 6.1: Mechanical and chemical processing steps for GaSb substrate removal

In this geometry, the conduction of the GaSb substrate does not contribute to the transport study, therefore substrate is not removed. Figure 6.2 shows the possible sample geometry to study the vertical transport in the SLs.

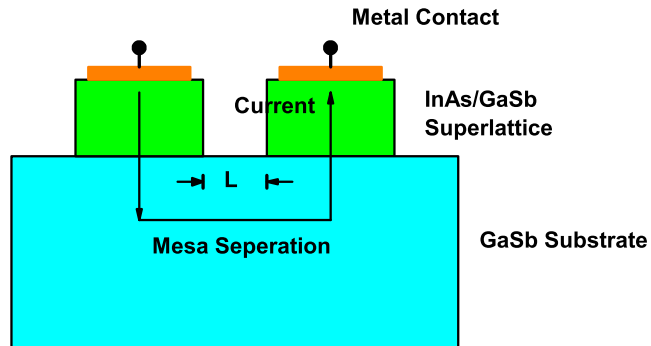


Figure 6.2: SL sample geometry for vertical transport study

For the vertical transport sample geometry, pixels are defined by mesa isolation etch where voltage is applied between the tops of the mesas and current is measured as a function of magnetic field. Due to this geometry, the current flow direction measured in this method is perpendicular to the current flow direction in the substrate, therefore the transport properties of the GaSb substrate does not affect the

measurement results.

6.2.2 Minority carrier lifetime

To date, there is no comprehensive study correlating the carrier lifetime to the structural properties, and growth parameters of the SL. Such a systematic study will provide invaluable data such as the minority carrier diffusion length and lifetime and intersubband relaxation time that will enable to determine the limiting scattering mechanisms in InAs/GaSb system, such as Shockley Read Hall and Auger recombination.

6.2.3 Device performance optimization for pin and nBn detectors

In order to improve the surface leakage currents in longwave pin detectors, a stable passivant is required to prevent the oxidation of GaSb layers in the SL material system.

Also, for improving the device performance of the long-wave nBn detectors and to prevent the dark currents associated with SRH centers, an optimized barrier with zero valence band off set is required. This requires a comprehensive study of band alignment of different material system with the SL band alignment.

6.2.4 Alternative designs

- Type-II InAs/GaSb SLs grown on GaSb substrates, still suffers from a relatively high cost mainly associated with its substrate. GaSb substrates are expensive and are limited to 2" diameter or smaller wafers. For this reason, there is

Chapter 6. Conclusions and Future Work

a great deal of interest in SL on GaAs/Si substrates, which are cheaper and are available in larger wafer sizes, both of which reduce the manufacturing costs. In order to grow SLs on alternative substrates a detailed study of effect of different interfaces, and growth optimization techniques on structural and optical properties of SL detectors is required.

- InAsSb based infrared detectors are important for non-cryogenic thermal imaging applications in the mid wave infrared (MWIR). InAsSb material system can provide cheap, robust and inexpensive infrared detectors as they are based on a mature III-V compound semiconductor technology. Lattice matched InAsSb on GaSb substrate (9% Sb) show excellent material quality for midwave infrared (MWIR) regime. IR detectors using nBn design have also shown promising results in eliminating the currents associated with Shockley-Read-Hall centers and mesa lateral surface imperfections that increases the operating temperature. The goal is to produce room temperature mid-wave InAsSb infrared detectors based on nBn design. The study requires detailed study of barrier in terms of material, composition and doping level.

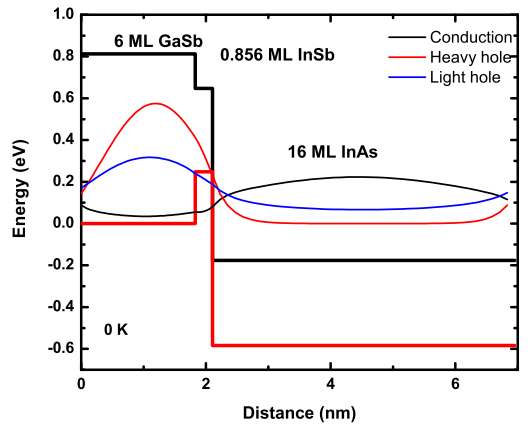
6.2.5 Design of very longwave infrared (VLWIR) detector and theoretical modeling

Very long wavelength infrared (VLWIR) applications, such as space-based astronomy and remote pollution monitoring, require detectors with high performance and stability over broad temperature ranges. In order to use InAs/GaSb SLs for VLWIR regime, different InAs and GaSb layer thicknesses and different strain compensating interface layers need to be investigated. Initial work on modeling an InSb strain compensating layer and structural optimization has been performed, however the effect of this strain compensating layer and optimization of InAs/InSb/GaSb layers

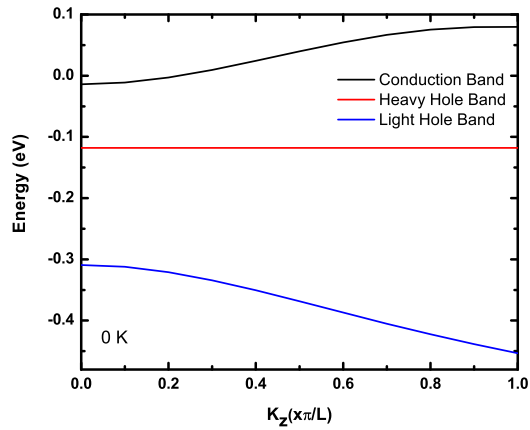
Chapter 6. Conclusions and Future Work

on the device performance need to be investigated. Figure 6.3(a) and (b) show next nano simulations for 16 MLs of InAs/0.856 MLs of InSb/ 7 MLs of GaSb band alignment and dispersion diagram, respectively. Figure 6.3(c) shows the best structural properties in terms of lattice mismatch and FWHM of first order SL peak which is achieved by 0.86 MLs of strain compensating InSb layer grown between InAs and GaSb layers.

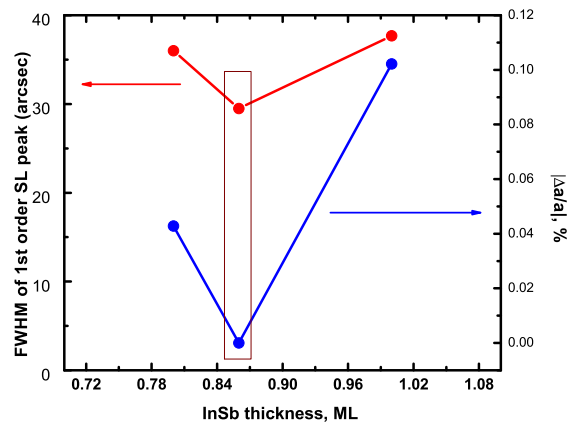
Chapter 6. Conclusions and Future Work



(a)



(b)



(c)

Figure 6.3: (a) next-nano band alignment simulation of 16 MLs InAs/0.86 MLs InSb/7 MLs GaSb (b) next-nano dispersion diagram which indicates a cut-off wavelength of $12 \mu\text{m}$ at 0 K (c) Growth optimization for VLWIR SL structure using InSb strain compensating layer

References

- [1] S. H. Huang, G. Balakrishnan, M. Mehta, A. Khoshakhlagh, L. R. Dawson, D. L. Huffaker, and P. Li, “Epitaxial growth and formation of interfacial misfit array for tensile gasb on gasb,” *Applied Physics Letters*, vol. 90, no. 16, p. 161902, 2007. [Online]. Available: <http://link.aip.org/link/?APL/90/161902/1>
- [2] A. Rogalski and P. Martyniuk, “Inas/gainsb superlattices as a promising material system for third generation infrared detectors,” *Infrared Physics & Technology*, vol. 48, no. 1, pp. 39 – 52, 2006. [Online]. Available: <http://www.sciencedirect.com/science/article/B6TJ9-4G9935K-8/2/d7c6f7136b0a76c990a432e0362887e4>
- [3] M. Tidrow, W. Beck, W. Clark, H. Pollehn, J. Little, N. Dhar, R. Leavitt, S. Kennerly, D. Beekman, A. Goldberg, and Others, “Device physics and focal plane array applications of QWIP and MCT,” *Opto-Electronics Review*, vol. 7, no. 4, pp. 283–296, 1999. [Online]. Available: [http://www.inh.wat.edu.pl/review/optor/1999/4/7\(4\)283.pdf](http://www.inh.wat.edu.pl/review/optor/1999/4/7(4)283.pdf)
- [4] C. Hansson, “Comparative study of infrared photodetectors based on quantum wells (qwips) and quantum dots (qdips),” Master’s thesis, Halmstad University, 2006.
- [5] I. Vurgaftman, J. R. Meyer, and L. R. Ram-Mohan, “Band parameters for iii–v compound semiconductors and their alloys,” *Journal of Applied Physics*, vol. 89, no. 11, pp. 5815–5875, 2001. [Online]. Available: <http://link.aip.org/link/?JAP/89/5815/1>
- [6] M. Razeghi, “Overview of antimonide based iii-v semiconductor epitaxial layers and their applications at the center for quantum devices,” *THE EUROPEAN PHYSICAL JOURNAL APPLIED PHYSICS*, vol. 23, pp. 149–205, 2003.

References

- [7] L. Esaki, “A bird’s-eye view on the evolution of semiconductor superlattices and quantum wells,” *Quantum Electronics, IEEE Journal of*, vol. 22, no. 9, pp. 1611–1624, Sep 1986.
- [8] M. R. Kitchin and M. Jaros, “Characterization of gasb/inas type ii infrared detectors at very long wavelengths: carrier scattering at defect clusters,” *Physica E: Low-dimensional Systems and Nanostructures*, vol. 18, no. 4, pp. 498 – 508, 2003. [Online]. Available: <http://www.sciencedirect.com/science/article/B6VMT-4876CYY-2/2/399e932f72c8c28cb17376400153088b>
- [9] G. C. Dente and M. L. Tilton, “Pseudopotential methods for superlattices: Applications to mid-infrared semiconductor lasers,” *Journal of Applied Physics*, vol. 86, no. 3, pp. 1420–1429, 1999. [Online]. Available: <http://link.aip.org/link/?JAP/86/1420/1>
- [10] P.-Y. Delaunay, B. M. Nguyen, D. Hoffman, and M. Razeghi, *Quantum Electronics, IEEE Journal of*, vol. 44, no. 5, pp. 462–467, May 2008.
- [11] D. Z.-Y. Ting, C. J. Hill, A. Soibel, S. A. Keo, J. M. Mumolo, J. Nguyen, and S. D. Gunapala, “A high-performance long wavelength superlattice complementary barrier infrared detector,” *Applied Physics Letters*, vol. 95, no. 2, p. 023508, 2009. [Online]. Available: <http://link.aip.org/link/?APL/95/023508/1>
- [12] B.-M. Nguyen, S. Bogdanov, S. A. Pour, and M. Razeghi, “Minority electron unipolar photodetectors based on type ii inas/gasb/alsb superlattices for very long wavelength infrared detection,” *Applied Physics Letters*, vol. 95, no. 18, p. 183502, 2009. [Online]. Available: <http://link.aip.org/link/?APL/95/183502/1>
- [13] Y. Wei, A. Hood, H. Yau, A. Gin, M. Razeghi, M. Z. Tidrow, and V. Nathan, “Uncooled operation of type-ii inas/gasb superlattice photodiodes in the midwavelength infrared range,” *Applied Physics Letters*, vol. 86, no. 23, p. 233106, 2005. [Online]. Available: <http://link.aip.org/link/?APL/86/233106/1>
- [14] Y. Wei, A. Hood, H. Yau, V. Yazdanpanah, M. Razeghi, M. Z. Tidrow, and V. Nathan, “High-performance type-ii inas/gasb superlattice photodiodes with cutoff wavelength around 7 μ m,” *Applied Physics Letters*, vol. 86, no. 9, p. 091109, 2005. [Online]. Available: <http://link.aip.org/link/?APL/86/091109/1>
- [15] G. J. Sullivan, A. Ikhlassi, J. Bergman, R. E. DeWames, J. R. Waldrop, C. Grein, M. Flatté, K. Mahalingam, H. Yang, M. Zhong, and M. Weimer, “Molecular beam epitaxy growth of high quantum efficiency inas/gasb superlattice detectors,” vol. 23, no. 3, pp. 1144–1148, 2005. [Online]. Available: <http://link.aip.org/link/?JVB/23/1144/1>

References

- [16] B.-M. Nguyen, D. Hoffman, P.-Y. Delaunay, and M. Razeghi, “Dark current suppression in type ii inas/gasb superlattice long wavelength infrared photodiodes with m-structure barrier,” *Applied Physics Letters*, vol. 91, no. 16, p. 163511, 2007. [Online]. Available: <http://link.aip.org/link/?APL/91/163511/1>
- [17] A. Khoshakhlagh, J. B. Rodriguez, E. Plis, G. D. Bishop, Y. D. Sharma, H. S. Kim, L. R. Dawson, and S. Krishna, “Bias dependent dual band response from inas/ga(in)sb type ii strain layer superlattice detectors,” *Applied Physics Letters*, vol. 91, no. 26, p. 263504, 2007. [Online]. Available: <http://link.aip.org/link/?APL/91/263504/1>
- [18] E. H. Aifer, J. G. Tischler, J. H. Warner, I. Vurgaftman, J. R. Meyer, C. L. Canedy, and E. M. Jackson, “Dual band lwir/vlwir type-ii superlattice photodiodes,” *Infrared Technology and Applications XXXI*, vol. 5783, no. 1, pp. 112–122, 2005. [Online]. Available: <http://link.aip.org/link/?PSI/5783/112/1>
- [19] W. Harrison, *Electronic Structure and the Properties of Solids*, reprint ed. Dover Publications, 1980.
- [20] C. Kittel, *Quantum Theory of Solids*, second revised printing ed. New York: Wiley, 1987.
- [21] P. Yu and M. Cardona, *Fundamentals of Semiconductors: Physics and Materials Properties*, 3rd ed. Springer, 2005.
- [22] [Online]. Available: <http://www.nextnano.de/nextnano3/>
- [23] J. Steinshnider, M. Weimer, R. Kaspi, and G. W. Turner, “Visualizing interfacial structure at non-common-atom heterojunctions with cross-sectional scanning tunneling microscopy,” *Phys. Rev. Lett.*, vol. 85, no. 14, pp. 2953–2956, Oct 2000.
- [24] P. M. Thibado, B. R. Bennett, M. E. Twigg, B. V. Shanabrook, and L. J. Whitman, “Origins of interfacial disorder in GaSb/InAs superlattices,” *Applied Physics Letters*, vol. 67, no. 24, pp. 3578–3580, 1995. [Online]. Available: <http://link.aip.org/link/?APL/67/3578/1>
- [25] G. G. P. . F. I. Blefeld, R.; Osbourn, “The preparation and characterization of strained-layer superlattices in the gas+ gap system,” *Journal of Electronic Materials*, vol. 12, pp. 903–915, 1983.
- [26] J. W. Little, S. P. Svensson, W. A. Beck, A. C. Goldberg, S. W. Kennerly, T. Hongmatip, M. Winn, and P. Uppal, “Thin active region, type II superlattice photodiode arrays: Single-pixel and focal plane array

References

- characterization,” *Journal of Applied Physics*, vol. 101, no. 4, p. 044514, 2007. [Online]. Available: <http://link.aip.org/link/?JAP/101/044514/1>
- [27] R. Kaspi, C. Moeller, A. Ongstad, M. L. Tilton, D. Gianardi, G. Dente, and P. Gopaladasu, “Absorbance spectroscopy and identification of valence subband transitions in type-II InAs/GaSb superlattices,” *Applied Physics Letters*, vol. 76, no. 4, pp. 409–411, 2000. [Online]. Available: <http://link.aip.org/link/?APL/76/409/1>
- [28] E. Plis, S. Annamalai, K. T. Posani, S. Krishna, R. A. Rupani, and S. Ghosh, “Midwave infrared type-II InAs/GaSb superlattice detectors with mixed interfaces,” *Journal of Applied Physics*, vol. 100, no. 1, p. 014510, 2006. [Online]. Available: <http://link.aip.org/link/?JAP/100/014510/1>
- [29] “Growth of inas/gasb short-period superlattices for high-resolution mid-wavelength infrared focal plane array detectors,” *Journal of Crystal Growth*, vol. 278, no. 1-4, pp. 156 – 161, 2005, 13th International Conference on Molecular Beam Epitaxy. [Online]. Available: <http://www.sciencedirect.com/science/article/B6TJ6-4FB9419-2/2/c09026a5f41ae49608cc83d3e1a93bed>
- [30] H. J. Haugan, L. Grazulis, G. J. Brown, K. Mahalingam, and D. H. Tomich, “Exploring optimum growth for high quality InAs/GaSb type-II superlattices,” *Journal of Crystal Growth*, vol. 261, no. 4, pp. 471 – 478, 2004. [Online]. Available: <http://www.sciencedirect.com/science/article/B6TJ6-49Y3JCK-3/2/08d9067d6ed98d9781312d32d12302ae>
- [31] A. S. Bracker, M. J. Yang, B. R. Bennett, J. C. Culbertson, and W. J. Moore, “Surface reconstruction phase diagrams for InAs, AlSb, and GaSb,” *Journal of Crystal Growth*, vol. 220, no. 4, pp. 384 – 392, 2000. [Online]. Available: <http://www.sciencedirect.com/science/article/B6TJ6-41WB9CM-7/2/1b7bf4033fb9b3f443099569080ea7c9>
- [32] E. Plis, S. J. Lee, Z. Zhu, A. Amtout, and S. Krishna, “InAs/GaSb superlattice detectors operating at room temperature,” *Selected Topics in Quantum Electronics, IEEE Journal of*, vol. 12, no. 6, pp. 1269–1274, Nov.-dec. 2006.
- [33] D. Hoffman, B.-M. Nguyen, P.-Y. Delaunay, A. Hood, M. Razeghi, and J. Pellegrino, “Beryllium compensation doping of inas/gasb infrared superlattice photodiodes,” *Applied Physics Letters*, vol. 91, no. 14, p. 143507, 2007. [Online]. Available: <http://link.aip.org/link/?APL/91/143507/1>
- [34] J. B. Rodriguez, E. Plis, S. J. Lee, H. Kim, G. Bishop, Y. D. Sharma, L. R. Dawson, S. Krishna, and C. Jones, “Type-II InAs/GaSb strain layer

References

- superlattice detectors for higher operating temperatures,” B. F. Andresen, G. F. Fulop, and P. R. Norton, Eds., vol. 6542, no. 1. SPIE, 2007, p. 654208. [Online]. Available: <http://link.aip.org/link/?PSI/6542/654208/1>
- [35] S. Maimon and G. W. Wicks, “nBn detector, an infrared detector with reduced dark current and higher operating temperature,” *Applied Physics Letters*, vol. 89, no. 15, p. 151109, 2006. [Online]. Available: <http://link.aip.org/link/?APL/89/151109/1>
- [36] J. B. Rodriguez, E. Plis, G. Bishop, Y. D. Sharma, H. Kim, L. R. Dawson, and S. Krishna, “nBn structure based on InAs/GaSb type-II strained layer superlattices,” *Applied Physics Letters*, vol. 91, no. 4, p. 043514, 2007. [Online]. Available: <http://link.aip.org/link/?APL/91/043514/1>
- [37] H. S. Kim, E. Plis, J. B. Rodriguez, G. D. Bishop, Y. D. Sharma, L. R. Dawson, S. Krishna, J. Bundas, R. Cook, D. Burrows, R. Dennis, K. Patnaude, A. Reisinger, and M. Sundaram, “Mid-IR focal plane array based on type-II InAs/GaSb strain layer superlattice detector with nBn design,” *Applied Physics Letters*, vol. 92, no. 18, p. 183502, 2008. [Online]. Available: <http://link.aip.org/link/?APL/92/183502/1>
- [38] P. C. Klipstein, O. Klin, S. Grossman, N. Snapi, B. Yaakovovitz, M. Brumer, I. Lukomsky, M. Yassen, D. Aronov, B. Yofis, A. Glozman, T. Fishman, E. Berkowitz, O. Magen, I. Shtrichman, and E. Weiss, “Mwir inassb xbn detectors for high operating temperatures,” in *Defense, Security and Sensing*. SPIE, 2010, pp. 7660–86.
- [39] E. Plis, H. S. Kim, G. Bishop, S. Krishna, K. Banerjee, and S. Ghosh, “Lateral diffusion of minority carriers in nbn based type-II InAs/GaSb strained layer superlattice detectors,” *Applied Physics Letters*, vol. 93, no. 12, p. 123507, 2008. [Online]. Available: <http://link.aip.org/link/?APL/93/123507/1>
- [40] O. Schreer, M. L. Saenz, C. Peppermueller, T. Hierl, K. Bachmann, D. Clement, and J. Fries, “Helicopter-borne dual-band dual-fpa system,” *Infrared Technology and Applications XXIX*, vol. 5074, no. 1, pp. 637–647, 2003. [Online]. Available: <http://link.aip.org/link/?PSI/5074/637/1>
- [41] J. F. Scholl, E. L. Dereniak, M. R. Descour, C. P. Tebow, and C. E. Volin, “Phase grating design for a dual-band snapshot imaging spectrometer,” *Appl. Opt.*, vol. 42, no. 1, pp. 18–29, 2003. [Online]. Available: <http://ao.osa.org/abstract.cfm?URI=ao-42-1-18>
- [42] [Online]. Available: <http://cimss.ssec.wisc.edu/goes/burn/detection.html>

References

- [43] M. Walther, R. Rehm, J. Fleissner, J. Schmitz, J. Ziegler, W. Cabanski, and R. Breiter, "InAs/GaSb type-II short-period superlattices for advanced single and dual-color focal plane arrays," *Infrared Technology and Applications XXXIII*, vol. 6542, no. 1, p. 654206, 2007. [Online]. Available: <http://link.aip.org/link/?PSI/6542/654206/1>
- [44] L. V. G. N. E. N. M. G. P. R. V. G. A. P. G. P. E. . O. Smith, E.; Pham, "HgCdTe focal plane arrays for dual-color mid-and long-wavelength infrared detection," *Journal of Electronic Materials*, vol. 33, pp. 509–516, 2004.
- [45] Ünal Sakoğlu, J. S. Tyo, M. M. Hayat, S. Raghavan, and S. Krishna, "Spectrally adaptive infrared photodetectors with bias-tunable quantum dots," *J. Opt. Soc. Am. B*, vol. 21, no. 1, pp. 7–17, 2004. [Online]. Available: <http://josab.osa.org/abstract.cfm?URI=josab-21-1-7>
- [46] C. A. Hoffman, J. R. Meyer, E. R. Youngdale, F. J. Bartoli, and R. H. Miles, "Interface roughness scattering in semiconducting and semimetallic inas-ga[_{sub}1 - x]in[_{sub}x]sb superlattices," *Applied Physics Letters*, vol. 63, no. 16, pp. 2210–2212, 1993. [Online]. Available: <http://link.aip.org/link/?APL/63/2210/1>
- [47] F. Szmulowicz, S. Elhamri, H. J. Haugan, G. J. Brown, and W. C. Mitchel, "Demonstration of interface-scattering-limited electron mobilities in inas/gasb superlattices," *Journal of Applied Physics*, vol. 101, no. 4, p. 043706, 2007. [Online]. Available: <http://link.aip.org/link/?JAP/101/043706/1>
- [48] "Electrical properties of short period inas/gasb superlattice," *PHYSICA STATUS SOLIDI C CONFERENCES*, vol. 4, p. 1494, 2007.
- [49] J. S. L. Burkle, F. Fuchs and W. Pletschen, "Control of the residual doping of inas/gasb infrared superlattices," *APPLIED PHYSICS LETTERS*, vol. 77, p. 1659, 2000.
- [50] C. Cervera, J. B. Rodriguez, J. P. Perez, H. Ait-Kaci, R. Chaghi, L. Konczewicz, S. Contreras, and P. Christol, "Unambiguous determination of carrier concentration and mobility for inas/gasb superlattice photodiode optimization," *Journal of Applied Physics*, vol. 106, no. 3, p. 033709, 2009. [Online]. Available: <http://link.aip.org/link/?JAP/106/033709/1>
- [51] A. Hood, D. Hoffman, Y. Wei, F. Fuchs, and M. Razeghi, "Capacitance-voltage investigation of high-purity inas/gasb superlattice photodiodes," *Applied Physics Letters*, vol. 88, no. 5, p. 052112, 2006. [Online]. Available: <http://link.aip.org/link/?APL/88/052112/1>

References

- [52] M. Mehta, A. Jallipalli, J. Tatebayashi, M. Kutty, A. Albrecht, G. Balakrishnan, L. Dawson, and D. Huffaker, *Photonics Technology Letters, IEEE*, vol. 19, no. 20, pp. 1628–1630, Oct.15, 2007.
- [53] R. B. Laghumavarapu, A. Moscho, A. Khoshakhlagh, M. El-Emawy, L. F. Lester, and D. L. Huffaker, “Gasb/gaas type ii quantum dot solar cells for enhanced infrared spectral response,” *Applied Physics Letters*, vol. 90, no. 17, p. 173125, 2007. [Online]. Available: <http://link.aip.org/link/?APL/90/173125/1>
- [54] J. Tatebayashi, A. Khoshakhlagh, S. H. Huang, L. R. Dawson, G. Balakrishnan, and D. L. Huffaker, “Formation and optical characteristics of strain-relieved and densely stacked gasb/gaas quantum dots,” *Applied Physics Letters*, vol. 89, no. 20, p. 203116, 2006. [Online]. Available: <http://link.aip.org/link/?APL/89/203116/1>
- [55] R. E. Prange and T.-W. Nee, “Quantum spectroscopy of the low-field oscillations in the surface impedance,” *Phys. Rev.*, vol. 168, no. 3, pp. 779–786, Apr 1968.
- [56] J. R. Meyer, D. J. Arnold, C. A. Hoffman, F. J. Bartoli, and L. R. Ram-Mohan, “Electron and hole in-plane mobilities in hgte-cdte superlattices,” *Phys. Rev. B*, vol. 46, no. 7, pp. 4139–4146, Aug 1992.
- [57] A. Gold, “Electronic transport properties of a two-dimensional electron gas in a silicon quantum-well structure at low temperature,” *Phys. Rev. B*, vol. 35, no. 2, pp. 723–733, Jan 1987.